PATH INTEGRAL CALCULATIONS OF COUPLED SPIN AND DENDRIMERIC SYSTEMS

BY

RESHMI DANI

DISSERTATION

Submitted in partial fulfillment of the requirements for
the degree of Doctor of Philosophy in Chemistry
in the Graduate College of the
University of Illinois Urbana-Champaign, 2022

Urbana, Illinois

Doctoral Committee:

   Professor Nancy Makri, Chair
   Professor Zan Luthey-Schulten
   Professor Josh Vura-Weis
   Research Assistant Professor Taras Pogorelov

Abstract

Extended systems like interacting spin chains, dendrimers and excitonic transfer complexes are essential to further our understanding of emergent behavior in complex condensed phase systems. Quantum mechanics plays a very important role in investigating such systems. However, exact quantum dynamics calculations of such condensed phase systems are extremely challenging owing to the exponential scaling of quantum mechanics. The work presented in this thesis utilizes the path integral methods developed in the Makri group to perform fully quantum mechanical simulations of such extended systems. The kinds of systems studied here can be broadly divided into two classes: spin chains (quantum transverse field Ising chain) and extended systems with Frenkel interactions (dendrimers, excitonic ring and chains).

For the spin systems, the path integral methods are used to obtain real time dynamics of finite-length Ising chains where each spin is coupled to a dissipative bath. The calculations performed emulate a quantum quench experiment, where the chain is initially prepared in the ferromagnetic 'aligned' phase and is made to evolve with parameters corresponding to the paramagnetic phase. The corresponding dynamics depends on the system and bath parameters and the temperature. Considerable edge effects are observed too.

Another kind of studied in this thesis is the model dendrimer. This is very different from the spin chains and adjacent segments in the dendrimer are known to interact through Frenkel excitations. Almost all examples of dendrimers used to funnel energy have a decreasing site energy towards the core to create an efficient energy funnel. We show here than even in the absence of an explicit energy bias, excitonic couplings can form a funnel to drive the excitation energy from the periphery to the core. The dynamics of the excitation energy in these systems is highly non-trivial and strongly affected by quantum mechanical effects. We show by eigenstate analysis and path integral time dynamics that for certain combinations of these excitonic couplings, we get more EET into the dendrimer core. Some combinations also exhibit frustration (analogous to spin systems) which causes considerable slowdown of the dynamics.

Lastly, we present our investigations for a multistate system coupled to a general bath with terms local in the system basis. We show here that the time derivatives of populations are given in terms of

imaginary components of coherences, i.e. off-diagonal elements of the reduced density matrix. When the process exhibits rate dynamics, we show that these imaginary components (or flux) exhibit a "plateau" region i.e. a region where the slope changes very slowly. All state-to-state rates can be obtained from the early "plateau" values of these imaginary components. We generalize the reactive flux method and its non-equilibrium version to multi-state processes and show that even in the completely incoherent limit of rate kinetics, the time evolution of populations is governed by coherences. Further, we also show that equilibrium population of the different species is also determined by these imaginary components, more precisely the short time evolution up to the plateau time.

We take advantage of the newly formed methods in the Makri lab to perform numerically exact quantum simulations of these extended systems coupled to dissipative baths to reveal the interesting features and the complex interplay between the different time and energy scales in the system which is highly non-trivial and requires a fully quantum mechanical treatment to capture fully what goes on in these systems.

To my parents Anuradha and Rajesh, and Shounak

Acknowledgements

First and foremost, I would like to thank my advisor Prof. Nancy Makri for her continuing support and encouragement over the course of my Ph.D. Her insightful approach to science, studying something from the simplest level to building up on that is something I have been awed by and hope to inculcate in my research methods. Even beyond academics, her support in everything I did, getting me plants, and cheesecakes for the whole lab is very encouraging. I am really very grateful to her for everything.

I would also like to thank my committee members Prof. Zaida Luthey Schulten, Prof. Josh Vura-Weis and Prof. Taras Pogorelov for their promptness in scheduling my exams and also for their input on my research.

I would also like to mention my undergraduate professors and mentors who were crucial to my introduction to the world of research and deciding to pursue a doctorate degree. Hence, I would like to thank Prof. Pradipta Ghosh, Prof. G. Krishnamoorthy, Prof. Ignacio Franco and Dr. Ila. I would also like to thank Prof. David Woon with whom I TAed for three semesters and loved every bit of it.

I would also like to thank my current and former lab members during the course of my time at the Makri lab. Especially I would like to express my deep gratitude to Amartya, Marco and Sohang for the extremely supportive environment we have in our group and always being ready to help when I got stuck.

I also want to thank Lisa, Connie, Katie and Beth for always being there when I needed help with something and for making this intercontinental move so much less scary for us international students.

I have also been extremely lucky to have some amazing friends from all stages of my academic life and who I am sure are now friends for life. Ragini, Alison, Natasha, Ushma, Arunima, Moumita, Trisha, Sohini, Sudeshna, Payal, Rahul, Kinshuk and Srijon, I couldn't thank you enough for the support and encouragement you guys have given me.

Table of Contents

List of abbreviations

TLS   Two-level system

RDM   Reduced density matrix

PI   Path integral

QuAPI   Quasi adiabatic propagator path integral

QCPI   Quantum classical path integral

MPI   Modular Path Integral

SMatPI   Small matrix decomposition of the path integral

SMatMPI   Small matrix decomposition of the modular path integral

Chapter 1

Introduction

Extended systems are often encountered in chemistry and form the basis of studying very interesting processes; a few of them being magnetization of spin-chains,[1] quantum quench and quantum phase transitions in interacting many body systems,[2-3] and excitonic energy transfer in photosynthetic aggregates,[4-5] dendrimers.[6-8] Quantum mechanics plays a very important role in determining the dynamics and behavior of these systems. Classical methods and approximations[9-12] don't always account for the rich dynamical behaviors exhibited by these systems. However, the exponential scaling of quantum mechanics with system size renders exact simulations of such extended systems an extremely challenging task. There have been a lot of methods that have tried to tackle this problem of a larger system, namely density matrix renormalization group (DMRG)[13-14] using matrix product states (MPS)[15-16] and multiscale entanglement renormalization ansatz (MERA).[17] There have also been methods to study the real time dynamics of such extended systems like time dependent density matrix renormalization group (TD-DMRG)[18-20] and time dependent variational principle.[21] These methods primarily deal with these systems in the isolated state. However, such systems are never isolated and are always associated with an environment and(or) molecular vibrations. So, it is very important to take these into account to correctly describe and study these systems. Despite efforts to incorporate the effect of vibrational modes,[22] these wave function-based methods scale exponentially with respect to the number of modes required. When the system is associated with low frequency modes, the convergence becomes even more difficult.

To circumvent the issues with the wave function-based methods, methods have been developed that use the reduced density matrix or the RDM. In these methods, we are interested in the RDM or the density matrix of the system after integrating out the bath modes. This effectively reduces the dimensionality of the problem. While with the wave function-based methods, the dimensionality grew as the number of the system and the bath states, now the dimensionality that affects the computational complexity is just the

dimension of the system of interest as the bath modes are integrated out. These methods rely on the fact that most classically forbidden processes (for example tunneling) occur in a very small subspace of the space spanned by all degrees of freedom and allow for system-solvent separation. A few of these methods include the Redfield theory,[9-10] Forsters theory[23]. However, these are perturbative approaches where the system-bath interaction strength is used as the perturbative factor. In cases where this coupling strength is not small, this perturbative approach fails to produce correct results. There are also methods which approach the system bath coupling strength non-perturbatively but use other approximations such as polaron transform perturbation theory[24-25], and the non-interacting blip approximation (NIBA).[26] There are exact methods that have been developed too, like hierarchical equations of motions (HEOM)[28-30] which is a non-perturbative approach to solving for the RDM of open quantum systems. There has been enormous amount of work that has been done to develop this method further and it has been solved exactly for a Drude bath[29] but this method hasn't yet been developed for any generic bath with arbitrary number of modes.

There have also been methods developed on the generalized quantum master equation[31-32] to solve for the reduced dynamics in open quantum systems. Here, the effects of the bath are accounted for by the memory kernel. The computational bottleneck of these methods is the calculational of this memory kernel as it requires knowledge of the evolution of the system with the environment. The exactness of this method depends on the exactness of the method used to determine this memory kernel. For example, when the kernel is calculated using perturbative and Markovian approximations, it leads to the well-known Redfield-Bloch equations.[10] Thus, if one could calculate the master equation kernel over the entire memory length, these methods can give the RDM dynamics up to longer times. However, the calculation of these kernels is not always trivial.

All these problems can be overcome using the path integral formulation of quantum mechanics[33-34] using the influence functional[27,50] to account for the effect of the bath on the system. It is a useful formulation to begin with as it speaks the common language of paths with classical mechanics. These are paths local in space, but the formulations sums over every possible path which takes care of the nonlocality of quantum mechanics. By integrating out the bath modes, we essentially transform a non-Markovian

algorithm to a Markovian one. This formulation thus allows us to include an arbitrary number of vibrational modes at no extra cost by integrating out the modes giving rise to the influence functional. In case of a harmonic bath, these influence functionals have an analytical form. The oldest method to solve a system connected to a harmonic bath, the quasi-adiabatic propagator path integral[35-66] (QuAPI) was formulated in the Makri group in the early 90s. We can thus include the full thermal effects of any arbitrary harmonic bath without any approximations. However, modifications to this method are required to deal with larger system size, as even though the bath modes could be added at no extra computational cost, the algorithm still scales exponentially when the size of the isolated subsystem (or the system of interest as mentioned before) increases. More recently, new methods have been developed in the Makri lab to deal with larger systems without an intractable increase in the scaling. The current work uses two such methods – the modular path integral[37-38] (MPI) and the small matrix decomposition of path integral[39-41] (SMatPI) to study two classes of extended systems: quantum Ising spin chains and dendrimeric systems[6-8] with Frenkel interactions.

1.1 Dynamics of the quantum Ising chain

The quantum Ising chain describes a spin chain where every spin can occupy the 'up' or the 'down' state and can tunnel between these two states and neighboring spins interact through a $\hat{\sigma}_z \hat{\sigma}_z$ interaction. It is described by the Hamiltonian

$$\hat{H}_{\text{Ising}} = -\hbar\Omega\sum_{\alpha=1}^{n} \hat{\sigma}_x^{\alpha} - J\sum_{\alpha=1}^{n-1} \hat{\sigma}_z^{\alpha}\hat{\sigma}_z^{\alpha+1} \tag{1.1}$$

where $\hbar\Omega$ is the transverse field and J gives the spin-spin coupling strength. The two parameters are antagonistic as one tries to orient the spins creating 'order' while the transverse field causes the spins to flip via quantum tunneling causing 'disorder'. Also, for positive J, the system has ferromagnetic interactions while for negative J, it has anti-ferromagnetic interactions. Such systems are common in magnetic

3

materials, where the spin-spin interactions, coupling of spin to phonons and molecular vibrations lead to dissipative interactions. A variety of crystals and metal-organic frameworks with interesting spin topologies have been identified, studied and synthesized[42-45].

There has been a lot of research on this model using various methods. There are analytic methods involving transformation into non-interacting spinless Fermions[46] (Jorden Wigner transformation) and a corresponding Bogoliubov technique[47]. There have been studies using imaginary time path integral methods[48], density matrix renormalization group (DMRG)[13]. However, there are not a lot of results that show the real-time dynamics of such systems of any size in presence of dissipation. In this thesis, we have reported the exact quantum dynamics for a finite length Ising chain, where every spin is coupled to a dissipative bath. The main observable that has been studied here is the average position $\langle \sigma_z(t) \rangle$ of the spin along the z direction, which is obtained from the population $P_\uparrow$ of the "up" state, and this observable is examined during the tunneling dynamics that follows the non-equilibrium initial condition $P_\uparrow(0) = 1$. This observable is proportional to the spin magnetization. These results help to explore the complex behavior emerging from the interaction of these extended systems and the dissipative medium.

1.2 Excitation energy transfer in bias-free dendrimers

Dendrimers are highly branched macromolecules consisting of a core, repeat units and a periphery[6-8]. Fig. 1.1 shows one such example of a dendrimer containing of three generations (which means there are three branching units).
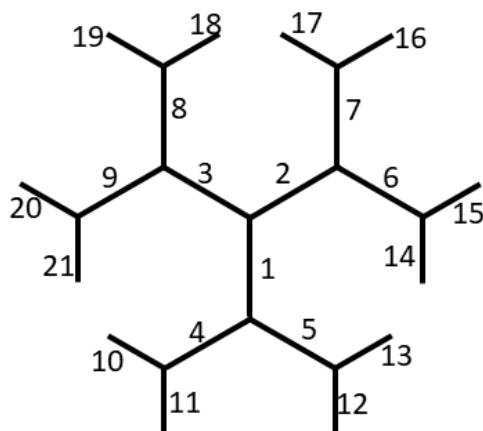
Fig.1.1 A three generation dendrimer with numbered segments. Segments 1-3 form the innermost core or the first generation, 4-9 forming the middle core or the second generation, and 10-21 forming the outermost core or the third generation.

The core forms the innermost generation and the periphery the outermost with an arbitrary number of generations in between. They have been of great interest in the field of energy harvesting as they can act like antennae molecules which can absorb energy at the periphery and transfer it to the core with high efficiency. We consider dendrimers consisting of building blocks of conjugated molecules whose wavefunctions are delocalized over linear segments. Electronic state calculations[49] have shown that the interactions between these building blocks (or segments) can be mapped on to a Frenkel Hamiltonian with nearest neighbor interactions

$$\hat{H}_e = \sum_{\alpha=1}^{n} \varepsilon_\alpha |\alpha\rangle\langle\alpha| + \sum_{\alpha=1}^{n-1} J_{\alpha,\alpha+1} \left(|\alpha\rangle\langle\alpha+1| + |\alpha+1\rangle\langle\alpha| \right) \qquad (1.2)$$

where $J_{\alpha,\alpha+1}$ gives the excitonic coupling parameter. A plethora of work has been done for dendrimers where the energy of a dendrimer generation decreases from the periphery to the core, so as to create an efficient 'funnel' for the energy to transfer. In this thesis, we explore the possibility of creating an efficient funnel not by an energetic bias, but by varying the different electronic couplings between the dendrimer

segments. We present eigenstates and real time dynamics results of such systems to understand them better. The competition between eigenstate structure and entropic considerations in these structures dictates the equilibrium distribution in these dendrimers which tend to change with the temperature, the exciton-bath couplings and the relative magnitude and signs of the excitonic couplings. The numerical results presented for these dendrimers offers a fully quantum mechanical treatment of the dynamics leading to valuable insights.

1.3 Rates of multistate processes from the quantum coherences

In this work, we turn our attention to discrete multistate Hamiltonians, which can be used to model a variety of processes charge or energy transport or condensed-phase reactive processes described by continuous potentials discretized along a reaction coordinate. First, we show that the time derivative of the population at any time (for any site) is directly related to the imaginary part of the RDM elements (or the coherences). Then we show how under certain regimes, we can write the populations in terms of kinetic equations and extract rate constants for the same using the coherences.

When the reaction time is sufficiently long compared to the timescales of the reactants themselves, rate kinetics are observed. In this case, there is a considerable separation of timescales i.e. if the reactant is prepared in a particular configuration, there is first a very rapid relaxation to a local equilibrium before any product has been formed. We show in this work, that for processes where this rate theory is valid, the flux (or the time derivative of the population) shows a plateau time after which it goes into a very slow decay that characterizes the reactive processes. Thus, here we can obtain the rate constants for the reaction rates from the imaginary part of the RDM elements at the plateau time. The rate kinetics here can be described by simple kinetic equations that involve a matrix of state-to-state transition rates The evolution of the state populations is then obtained from the short-time simulation results and the solution of the kinetic equations

with the calculated rate matrix. Thus, one needs to calculate exact quantum dynamics only up to a short time and get long-time dynamics. This is particularly useful for larger system and/or complex environments.

1.4 References

1) Bogani, L.; Vingidini, A.; Sessoli, R.; Gatteschi, D.; Single chain magents: where to from here?. *J. Mater. Chem.*, **2008**, *18*, 4750–4758

2) Calabrese, P.; Essler, F.; Fagotti, M., Quantum quench in the transverse- field Ising chain. *PRL.* **2011**, *106*, 227203

3) Dziarmaga, J., Dynamics of a quantum phase transition and relaxation to a steady state. *Adv. Phys.* **2010**, *59* (6), 1063-1189

4) Pullerits, T.; Sundstrom, V., Photosynthetic light-harvesting pigment-protein complexes: Toward understanding how and why. *Acc. Chem. Res.* **1996,** *29*, 381-389.

5) Blankenship, R. E., *Molecular mechanisms of photosynthesis*. World Scientific: London, **2002**

6) Moore, J. S., Shape-Persistent Molecular Architectures of Nanoscale Dimension. *Acc. Chem. Res.* **1997,** *30* (10), 402-413.

7) Ballauff, M.; Likos, C. N., Dendrimers in Solution: Insight from Theory and Simulation. *Angew. Chem. Intl. Ed.* **2004,** *43* (23), 2998-3020

8) Abbasi, E.; Aval, S. F.; Akbarzadeh, A.; Milani, M.; Nasrabadi, H. T.; Joo, S. W.; Hanifehpour, Y.; Nejati-Koshki, K.; Pashaei-Asl, R., Dendrimers: synthesis, applications, and properties. *Nanoscale Res. Lett.* **2014,** *9* (1), 247

9) Redfield, A. G., On the theory of relaxation processes. *Ibm J. Res. Dev.* **1957**, *1*, 19

10) Laird, B. B.; Budimir, J.; Skinner, J. L., Quantum-mechanical derivation of the Bloch equations: Beyond the weak-coupling limit. *J. Chem. Phys.* **1991**, *94*, 4391

11) Pearle, P., Simple derivation of the Lindblad equation. *Eur. J. Phys.* **2012**, *33*, 805

12) Manzano, D.; A short introduction to the Lindblad master equation. *AIP Adv.* **2020**, 10, 025106

13) White, S. R., Density matrix formulation for quantum renormalization groups. *Phys. Rev. Lett.* **1992**, *69*, 2863

14) Olivares-Amaya, R.; Hu, W.; Nakatani, N.; Sharma, S.; Yang, J.; Chan, G. K., The ab-initio density matrix renormalization group in practice. *J. Chem. Phys.* **2015**, *142*, 034102

15) Lars-Hendrik, F.; Daniela, P., Ultrafast ab initio quantum chemistry using matrix product states. *J. Chem. Theory Comput.* **2019**, *15* (4), 2154–2165

16) Román, O., A practical introduction to tensor networks: Matrix product states and projected entangled pair states. Ann. Phys. **2014**, *349*, 117-158

17) Vidal, G., Class of quantum many-body states that can be efficiently simulated. *Phys. Rev. Lett.* **2008**, *101*, 110501

18) Cazalilla, M.; Marston, J. Time-dependent density-matrix renormalization group: A systematic method for the study of quantum many-body out-of-equilibrium systems. *Phys. Rev. Lett.* **2002**, *88*, 256403

19) White, S. R.; Feiguin, A., E. Real-time evolution using the density matrix renormalization group. *Phys. Rev. Lett.* **2004**, *93*, 076401

20) Yao, Y.; Ke-Wei, S.; Zhen, L.; Haibo, M., Full quantum dynamics simulation of a realistic molecular system using the adaptive time-dependent Density matrix renormalization group method. *J. Phys. Chem. Lett.* **2018**, *9* (2), 413-419

21) Jutho, H., Cirac, J. I.; Tobias, J. O.; Iztok, P.; Henri, V.; Frank, V., Time-dependent variational principle for quantum lattices. *Phys. Rev. Lett.* **2011**, *107* (7), 070601

22) Ren, J.; Shuai, Z.; Chan, G. K., Time-dependent density matrix renormalization group algorithms for nearly exact absorption and fluorescence spectra of molecular aggregates at both zero and finite temperature. *J. Chem. Theory Comput.* **2018**, 14, 10, 5027-5039

23) Scholes, G.; Xanthipe, J.; Fleming, G., Adapting the Förster theory of energy transfer for modeling dynamics in aggregated molecular assemblies. *J. Phys. Chem. B* **2001**, *105* (8), 1640-1651

24) Tokuda, N., A variational approach to the polaron problem. *J. Phys. C: Solid State Phys.* **1980**, *13*, L851

25) Dazhi, X.; Cao, J., Non-canonical distribution and non-equilibrium transport beyond weak system-bath coupling regime: A polaron transformation approach. *Front. Phys*. **2016,** *11* (4), 110308

26) Dekker, H., Noninteracting-blip approximation for a two-level system coupled to a heat bath. *Phys. Rev. B* **1987**, *35* (3), 1436-1437

27) Leggett, A. J.; Chakravarty, S.; Dorsey, A. T.; Fisher, M. P. A.; Garg, A.; Zwerger, W., Dynamics of the dissipative two-state system. *Rev. Mod. Phys*. **1987**, *59*, 1−85

28) Tanimura. Y.; Kubo, R., Time evolution of a quantum system in contact with a nearly gaussian-markoffian noise bath. *J. Phys. Soc. Jpn.* **1989**, *58*, 101

29) Tanimura, Y., Numerically "exact" approach to open quantum dynamics: The hierarchical equations of motion (HEOM). *J. Chem. Phys.* **2020**, *153*, 020901

30) Ikeda, T.; Scholes, G. D., Generalization of the hierarchical equations of motion theory for efficient calculations with arbitrary correlation functions. *J. Chem. Phys.* **2020**, *152*, 204101

31) Nakajima, S., On quantum theory of transport phenomena. *Prog. Theor. Phys.* **1958**, *20*, 948

32) Zwanzig, R., Ensemble method in the theory of irreversibility. *J. Chem. Phys.* **1960**, *33*, 1338-1341

33) Feynman, R. P., Space-time approach to non-relativistic quantum mechanics. *Rev. Mod. Phys.* **1948**, *20*, 367-387

34) R. P. Feynman and A. R. Hibbs, *Quantum Mechanics and Path Integrals*. (McGraw-Hill, New York, 1965

35) Makri N., Numerical path integral techniques for long time dynamics of quantum dissipative systems *J. Math. Phys.* **1995**, *36*, 2430-2456

36) Makri N., Quantum dissipative dynamics: A numerically exact methodology. *J. Phys. Chem.* **1998**, *102* (24), 4414-4427

37) Makri N., Modular path integral methodology for real-time quantum dynamics. *J. Chem. Phys.* **2018,** *149*, 214108

38) Makri N., Communication: Modular path integral: Quantum dynamics via sequential necklace linking. J. Chem. Phys. **2018**, *148*, 101101

39) Makri, N., Small matrix disentanglement of the path integral: overcoming the exponential tensor scaling with memory length. *J. Chem. Phys.* **2020,** *152*, 041104

40) Makri, N., Small matrix path integral for system-bath dynamics. *Journal of Chemical Theory and Computation* **2020,** *16*, 4038–4049

41) Makri, N., Small matrix path integral with extended memory. *J. Chem. Theory and Comput.* **2021,** *17*, 1-6

42) Escalera-Moreno, L.; Baldoví, J. J.; Gaita-Ariño, A.; Coronado, E., Spin states, vibrations and spin relaxation in molecular nanomagnets and spin qubits: a critical perspective. *Chem. Sci.* **2018**, *9* (13), 3265-3275

43) Dixey, R. J. C.; Orlandi, F.; Manuel, P.; Mukherjee, P.; Dutton, S. E.; Saines, P. J., Emergent magnetic order and correlated disorder in formate metal-organic frameworks. *Phil. Trans. R. Soc. A.* **2019**, *377* (2149), 20190007

44) Collins, K. A.; Saballos, R. J.; Fataftah, M. S.; Puggioni, D.; Rondinelli, J. M.; Freedman, D. E., Synthetic investigation of competing magnetic interactions in 2D metal–chloranilate radical frameworks. *Chem. Sci.* **2020**, *11* (23), 5922-5928

45) Anthony, J. C.; Benjamin, P. J., Quasi-one dimensional magnetic interactions in the three-dimensional hyper-honeycomb framework [(C2H5)3NH]2Cu2(C2O4)3. *Phys. Chem. Chem. Phys.* **2021**, *23*, 5012-5019

46) Pfeuty, P., The one-dimensional Ising model with a transverse field. *Ann. Phys.* **1970**, *57* (1), 79-90

47) Suzuki, S.; Inoue, J.; Chakrabarty, B. K., *Quantum Ising phases and transitions in transverse Ising models*, 2nd ed. (Springer-Verlag, Berlin-Heidelberg, 2013)

48) Isakov, S. V.; Mazzola, G.; Smelyanskiy, V. N.; Jiang, Z.; Boixo, S.; Neven, H.; Troyer, M., Understanding quantum tunneling through quantum monte carlo simulations. *Phys. Rev. Lett.* **2016**, *117* (18), 180402

49) Poliakov, E. Y.; Chernyak, V.; Tretiak, S.; Mukamel, S., Exciton-scaling and optical excitations of self-similar phenylacetylene dendrimers. *J. Chem. Phys.* **1999,** *110* (16), 8161-8175

50) Feynman R.P., Vernon F.L., The theory of a general quantum system interacting with a linear dissipative system. *Ann. Phys.* **2000**, *281* (1), 547-607

Chapter 2

Path Integral Methods

This chapter describes in brief the path integral methods developed in the Makri group that have been used to study the systems and processes discussed in this thesis.

Feynman's path integral formulation of time-dependent quantum mechanics[1-2] offers an attractive alternative to the Schrödinger equation when wavefunction storage is not practical. In its original form, however, evaluation of the path integral hinges on one's ability to compute highly multidimensional integrals with respect to auxiliary variables for each degree of freedom. This integrand being highly oscillatory is very hard to converge using Monte-Carlo methods (dynamical sign problem). Also, the phenomenon of interest in many cases might be limited to a small subspace. In that case, one might want to treat the small dimensional subspace as the system and everything else may be relegated to a different level of treatment. This different level can be exact (harmonic bath) or approximate (classical treatment). Methods in the Makri lab have led to efficient, fully quantum mechanical propagation algorithms for system-bath Hamiltonians[3-4] (QuAPI) and also to a rigorous and consistent quantum-classical methodology.[5] (QCPI)

These methods help us to calculate the dynamics of open quantum systems i.e. systems connected to an external bath. The RDM of the system is calculated by integrating out the bath co-ordinates using the influence functional approach.[8,16]. This allows for inclusion of any arbitrary number of bath modes at almost no extra computational cost.

Let us consider the expression for evolution of the RDM for a system with Hamiltonian H

$$\hat{\rho}(t) = \mathrm{Tr}_b \left[e^{-i\hat{H}t/h} \hat{\rho}(0) e^{i\hat{H}t/h} \right]$$

(2.1)

11

where $\hat{\rho}(0)$ is the initial RDM and the above trace is with respect to the bath modes. From this, we can calculate the expectation value of any operator $\hat{o}$ for this system by

$$\langle\hat{o}(t)\rangle = \mathrm{Tr_b}\left[\hat{\rho}(t)\hat{o}\right]. \tag{2.2}$$

We can obtain the path integral representation of this expression by expressing the time propagators as a product of multiple short time propagators and then inserting resolution of identities between each pair of these short time propagators. So, we have

$$\left[e^{-i\hat{H}t/\hbar} = \left(e^{i\hat{H}\Delta t/\hbar}\right)^N\right] \tag{2.3}$$

where $t = N\Delta t$ and we have broken up one time propagator into N short time propagators. Eq. 2.1 thus becomes

$$\hat{\rho}(t) = \mathrm{Tr_b}\left[e^{-i\hat{H}\Delta t/\hbar}e^{-i\hat{H}\Delta t/\hbar}.....e^{-i\hat{H}\Delta t/\hbar}\hat{\rho}(0)e^{i\hat{H}\Delta t/\hbar}.....e^{i\hat{H}\Delta t/\hbar}e^{i\hat{H}\Delta t/\hbar}\right]. \tag{2.4}$$

Inserting resolution of identities, we get

$$\hat{\rho}(t) = \mathrm{Tr_b}\left[\begin{matrix}\sum_{i_N^\pm}\sum_{i_{N-1}^\pm}...\sum_{i_0^\pm}e^{-i\hat{H}\Delta t/\hbar}\left|i_N^+\right\rangle\left\langle i_N^+\right|e^{-i\hat{H}\Delta t/\hbar}\left|i_{N-1}^+\right\rangle\left\langle i_{N-1}^+\right|.....e^{-i\hat{H}\Delta t/\hbar}\left|i_0^+\right\rangle\times \\ \left\langle i_0^+\left|\hat{\rho}(0)\right|i_0^+\right\rangle\left\langle i_0^-\left|e^{i\hat{H}\Delta t/\hbar}.....e^{i\hat{H}\Delta t/\hbar}\right|i_N^-\right\rangle\left\langle i_N^-\left|e^{i\hat{H}\Delta t/\hbar}\right.\right.\end{matrix}\right] \tag{2.5}$$

Here, $\left\{i_0^\pm, i_1^\pm, ...i_N^\pm\right\}$ gives the forward and backward paths respectively. In the next two sections, we go over two different approaches to simulate the exact dynamics of open systems starting from this path integral formulation.

2.1 Modular Path Integral (MPI) and Small Matrix Decomposition of MPI (SMatMPI)

The MPI[6-7] algorithm is a decomposition of the real-time path integral for extended systems with a primarily one-dimensional topology and each unit comprises a small number of quantum (spin or electronic) states which are coupled to a large number of harmonic degrees of freedom. This may be the normal mode coordinates of molecular vibrations or may represent a generic dissipative bath. Let us consider the Ising Hamiltonian described in Eq. 1.1 and the short time propagator for this model as mentioned in the earlier section. Performing a symmetric Trotter splitting one gets

$$
\left[e^{-i\hat{H}_{ising}\Delta t/\hbar} = e^{iJ\Delta t \sum_{\alpha=1}^{n-1} \hat{\sigma}_z^\alpha \hat{\sigma}_z^{\alpha+1}/2\hbar} \; e^{ih\Omega\Delta t \sum_{\alpha=1}^{n} \hat{\sigma}_x^\alpha/\hbar} \; e^{iJ\Delta t \sum_{\alpha=1}^{n-1} \hat{\sigma}_z^\alpha \hat{\sigma}_z^{\alpha+1}/2\hbar} \right] \tag{2.6}
$$

Combining this with Eq. 2.5 we get the expression

$$
\begin{aligned}
\left\langle \hat{o}(t) \right\rangle = \prod_{\alpha=1}^{n} \sum_{i_N^\pm} \sum_{i_{N-1}^\pm} ... \sum_{i_0^\pm} & e^{iJ\Delta t \; s_{\alpha,N}^+ s_{\alpha+1,N}^+/2\hbar} \left\langle i_{\alpha,N}^+ \left| e^{i\Omega\Delta t \sigma_x^\alpha} \right| i_{\alpha,N-1}^+ \right\rangle e^{iJ\Delta t \; s_{\alpha,N-1}^+ s_{\alpha+1,N-1}^+/\hbar} ... \times \\
& e^{iJ\Delta t \; s_{\alpha,0}^+ s_{\alpha+1,0}^+/2\hbar} \left\langle i_{\alpha,0}^+ \left| \hat{\rho}(0) \right| i_{\alpha,0}^- \right\rangle e^{-iJ\Delta t \; s_{\alpha,0}^- s_{\alpha+1,0}^-/2\hbar} ... e^{-iJ\Delta t \; s_{\alpha,N-1}^- s_{\alpha+1,N-1}^-/\hbar} \times \\
& \left\langle i_{\alpha,N-1}^- \left| e^{-i\Omega\Delta t \sigma_x^\alpha} \right| i_{\alpha,N}^- \right\rangle e^{iJ\Delta t \; s_{\alpha,N}^- s_{\alpha+1,N}^-/2\hbar} \left\langle i_{\alpha,N}^- \left| \hat{o}(t) \right| i_{\alpha,N}^+ \right\rangle
\end{aligned} \tag{2.7}
$$

If we look at Eq. 2.7 closely, we find that there are two types of terms, one body terms which only depend on the αth monomer and linking two body terms which link the αth monomer to the $\alpha+1$ th monomer. This can be written as the following matrix vector multiplication

$$
\boldsymbol{R}^{\alpha+1} = \boldsymbol{A}^{\alpha+1} \boldsymbol{T}^{\alpha,\alpha+1} \boldsymbol{R}^\alpha \tag{2.8}
$$

13

Here, $\boldsymbol{R}^{\alpha}$ is the vector containing the amplitudes of all paths of monomer α summed over all the monomers occurring previously in the chain. $\boldsymbol{T}^{\alpha,\alpha+1}$ is the linking matrix which links each path of monomer α to every path of monomer $\alpha+1$. When every unit in the system is connected to a dissipative bath, the path amplitudes of every monomer are augmented by the influence functional[16-17] of that given path for the particular monomer.

$$A^{\alpha}\left(i_0^{\pm},i_1^{\pm}....i_N^{\pm}\right) = \left\langle i_{\alpha,N}^{+}\left|e^{i\Omega\Delta t\sigma_x^{\alpha}}\right|i_{\alpha,N-1}^{+}\right\rangle\left\langle i_{\alpha,N-1}^{+}\left|e^{i\Omega\Delta t\sigma_x^{\alpha}}\right|i_{\alpha,N-2}^{+}\right\rangle...\left\langle i_{\alpha,0}^{+}\left|\hat{\rho}(0)\right|i_{\alpha,0}^{-}\right\rangle\times$$
$$\left\langle i_{\alpha,0}^{-}\left|e^{-i\Omega\Delta t\sigma_x^{\alpha}}\right|i_{\alpha,1}^{-}\right\rangle...\left\langle i_{\alpha,N-1}^{-}\left|e^{-i\Omega\Delta t\sigma_x^{\alpha}}\right|i_{\alpha,N}^{-}\right\rangle \qquad (2.9)$$

$$T^{\alpha,\alpha+1}(i_{\alpha,0}^{\pm},i_{\alpha,1}^{\pm}....i_{\alpha,N}^{\pm},i_{\alpha+1,0}^{\pm},i_{\alpha+1,1}^{\pm}....i_{\alpha+1,N}^{\pm}) = e^{iJ\Delta t\, s_{\alpha,N}^{+}s_{\alpha+1,N}^{+}/2\hbar}e^{iJ\Delta t\, s_{\alpha,N-1}^{+}s_{\alpha+1,N-1}^{+}/\hbar}...e^{iJ\Delta t\, s_{\alpha,0}^{+}s_{\alpha+1,0}^{+}/2\hbar}\times$$
$$e^{-iJ\Delta t\, s_{\alpha,0}^{-}s_{\alpha+1,0}^{-}/2\hbar}...e^{-iJ\Delta t\, s_{\alpha,N-1}^{-}s_{\alpha+1,N-1}^{-}/\hbar}e^{-iJ\Delta t\, s_{\alpha,N}^{-}s_{\alpha+1,N}^{-}/2\hbar} \qquad (2.10)$$

The MPI decomposition leads to linear scaling with respect to the number of units in the system of interest by connecting the discretized paths of each unit to those of the adjacent unit prior to discarding them. Any number of quadratic degrees of freedom may be treated exactly in the MPI algorithm through the influence functional[8] approach, which leads to analytical expressions for the relevant coefficients. The computational effort to execute this algorithm is further reduced by additional factorization[9] leading to highly efficient evaluation. In the MPI algorithm, once the αth unit is reached, the path amplitudes contain all the dynamical effects from units $1,2,\ldots,\alpha$. Thus, the sequential treatment of units in the MPI algorithm can also be viewed as an efficient, fully quantum mechanical construction of the influence functional from all preceding units. Thus, the influence functional (with all spin-spin and spin-bath interactions summed exactly) from these units up to α augments the path amplitudes of unit $\alpha+1$ upon linking.

Also, motivated by the small decomposition of the path integral for system-bath Hamiltonians[10], a small matrix decomposition of the modular path integral (SMatMPI) has also been introduced[11] based on the small matrix decomposition of path amplitudes. This algorithm allows for sequential linking of units

when path storage is not practical (due to larger system size) and also leads to an iterative algorithm in time, thus allowing us to simulate situations requiring long memory and extending calculations to longer time.

2.2 Small Matrix Path Integral (SMatPI) Decomposition

The small matrix decomposition[13-15] (SMatPI) of the quasi-adiabatic propagator path integral[3-4] (QuAPI) is an exact decomposition of the fully quantum mechanical real-time path integral expression. It fully accounts for exciton-vibration interactions at any temperature that employs minimal sized, $n^2 \times n^2$ matrices, thus enabling the simulation of multistate systems. The QuAPI algorithm uses the decrease of the nonlocal influence functional coupling i.e. finite memory length to evaluate the RDM through iterative propagation of a tensor which spans the memory length. The SMatPI decomposition does away with the need for tensors, obtaining the RDM through a sum of small matrix products

$$\tilde{\boldsymbol{\rho}}^{(N0)} = \sum_{r=1}^{L} \mathbf{M}^{(N,N-r)} \cdot \tilde{\boldsymbol{\rho}}^{(N-r,0)}, \quad N = L+1,\dots \tag{2.11}$$

where L is the memory length in units of the path integral time step and $\mathbf{M}^{(N,N-r)}$ are $n^2 \times n^2$ matrices recursively obtained by the full path integral expression with a discretized influence functional. Eq. 2.11 is an analytically derived, numerically exact decomposition of the RDM, which requires minimal storage, comparable to that of the RDM of interest. The effect of the bath at a particular temperature is captured by the discretized influence functional[16]

$$F_{i_N^\pm, i_{N-1}^\pm, \dots, i_0^\pm} = \prod_{k'=0}^{N} \prod_{k''=0}^{k'} F_{i_{k'}^\pm i_{k''}^\pm}^{(k'k'')} \tag{2.12}$$

which contains nonlocal interactions that couple the path integral variables at different times. This requires minimal storage and the cost of the total SMatPI algorithm is that of one QuAPI propagation step, thus allowing to go to really long times.

2.3 References

1) Feynman, R. P., Space-time approach to non-relativistic quantum mechanics *Rev. Mod. Phys.* **1948**, 20, 367-387

2) R. P. Feynman and A. R. Hibbs, *Quantum Mechanics and Path Integrals*. (McGraw-Hill, New York, 1965

3) Makri, N., Numerical path integral techniques for long time dynamics of quantum dissipative systems. *J. Math. Phys.* **1995**, 36, 2430-2456

4) Makri, N., Quantum dissipative dynamics: A numerically exact methodology. *J. Phys. Chem.* **1998**, 102, 24, 4414-4427

5) Makri, N., Quantum-classical path integral: A rigorous approach to condensed phase dynamics. *Intl. J. of Quan. Chem.* **2015**, 115, 1209-1214

6) Makri, N., Modular path integral methodology for real-time quantum dynamics. J. Chem. Phys. 2018 149, 214108

7) Makri, N., Communication: Modular path integral: Quantum dynamics via sequential necklace linking. J. Chem. Phys. 2018, 148, 101101

8) Feynman, R. P.; Vernon, F. L., The theory of a general quantum system interacting with a linear dissipative system. *Ann. of Phys.* **1963**, *24*, 118-173

9) Kundu, S.; Makri, N., Efficient matrix factorisation of the modular path integral for extended systems. *Mol. Phys.* **2021**, *119* (13), e1797200

10) Makri, N., Small matrix disentanglement of the path integral: Overcoming the exponential tensor scaling with memory length. *J. Chem. Phys.* **2020**, *152*, 041104

11) Makri, N., Small matrix modular path integral: iterative quantum dynamics in space and time. *Phys. Chem. Chem. Phys.* **2021**, *23*, 12537-12540

12) Makri, N., Small matrix decomposition of Feynman path amplitudes. *J. Chem. Theory Comput.* **2021** *17* (7), 3825-3829

13) Makri, N., Small matrix disentanglement of the path integral: overcoming the exponential tensor scaling with memory length. *J. Chem. Phys*. **2020**, *152*, 041104

14) Makri, N., Small matrix path integral for system-bath dynamics. *J. Chem. Theory Comput*. **2020**, *16*, 4038–4049

15) Makri, N., Small matrix path integral with extended memory. *J. Chem. Theory and Comput*. **2021**, *17*, 1-6

16) Feynman R.P., Vernon F.L., The theory of a general quantum system interacting with a linear dissipative system. *Ann. Phys.***1963**, *24*, 118−173

17) Leggett, A. J.; Chakravarty, S.; Dorsey, A. T.; Fisher, M. P. A.; Garg, A.; Zwerger, W., Dynamics of the dissipative two-state system. *Rev. Mod. Phys*. **1987**, *59*, 1−85

Chapter 3

Dynamics of Quantum Ising Chains with Dissipative Baths

3.1 Introduction

The spin-boson model[1] i.e the two-level system (TLS) interacting with a dissipative bath is the simplest example of quantum dissipative dynamics, where the dissipative bath leads to damping of the coherent oscillations in an isolated TLS. This quenching of oscillations depends on a lot of factors namely the temperature, the system-bath coupling strength and the characteristics of the bath. The dissipative TLS is relevant to a lot of chemical processes like charge transfer or spin dynamics and are ubiquitous in molecular systems.

The picture gets even more complex when we consider more than one TLS coupled to dissipative baths. The order-disorder transition, coherence, relaxation and entanglement properties of such systems are intriguing from the point of quantum information transfer. The quantum Ising (or transverse field Ising) chain consists of one-dimensional spins coupled only along the z-direction. A variety of crystals and metal-organic frameworks with interesting spin topologies have been identified, synthesized, and studied and look promising.[2-6]

The quantum Ising model was introduced by de Gennes[10] to describe hydrogen-bonding in ferroelectrics. Experimental realizations in ferromagnetic quasi-one-dimensional cobalt niobate in transverse magnetic fields[11] and in systems of cold rubidium atoms confined in an optical lattice[12] have been reported. The infinite quantum Ising chain of identical spins has been solved analytically[13-14] by transforming the interacting spin operators to non-interacting spinless fermions using the Jordan-Wigner

---

transformation and then diagonalizing the transformed Hamiltonian with the aid of the Bogoliubov technique.[15] These and many other analytical tools have led to valuable insights and a good understanding

of important aspects surrounding the intriguing physics that characterizes this system in the isolated state[16], but are not suitable for studying the dynamics of individual spins in quantum Ising chains of finite length and cannot account for dissipative interactions.[17-18] Numerical studies of isolated finite-length spin chains have been carried out[19] with methods based on the density matrix renormalization group (DMRG) formulation.[20-21] Imaginary-time path integral calculations have been employed to investigate instanton tunneling paths that connect the two states of aligned spins.[22-23]

The quantum Ising model is characterized by two parameters, the spin-spin coupling strength J and the tunneling frequency Ω of the individual spins, which act against each other (explained in section 3.2) and lead to an ordered ferromagnetic phase with two degenerate ground states and a disordered paramagnetic phase with a single ground state, which in the infinite chain limit leads to a phase transition at zero temperature.[24] This behavior is of much interest from the perspective of quantum statistical physics and also quantum quench dynamics.[25-28] The quantum Ising chain is also of interest in the design of quantum computers, which rely on the entanglement properties of qubits. For example, adiabatic passage through the quantum phase transition can generate a maximally entangled spin state.[29] Dissipative effects are critical in that regard, as they can easily destroy the coherence and entanglement of coupled spins.

We investigate the dynamics of the spin magnetization in relatively short quantum Ising chains in the presence of dissipative harmonic baths attached to the spins. In contrast to previous studies, we simulate the real-time evolution of individual spins in various parameter regimes. We use our simulation results to characterize the behavior of the quantum Ising chain in comparison to that of the simpler, single TLS coupled to a bath. We emphasize on the coherent properties of the spin dynamics and the edge effects during a quantum quench, where the system is allowed to evolve under a paramagnetic (disordered) phase following preparation in the ferromagnetic (ordered) phase. To maintain the relevance of this model to model aggregates, each spin was coupled to its own vibrational bath. The average value of the z projection

of a particular spin, which is proportional to the magnetization is calculated using numerically exact, fully quantum mechanical path integral methods. We chose a bath model characterized by the commonly used Ohmic spectral density.[30]

We find that even in the absence of a dissipative bath, coupling to the spin chain leads to damping of population of the tagged TLS[26]. This is due to the spectral properties of the quantum Ising environment which are rather different than that of a harmonic bath. Coupling to harmonic bath leads to decoherence through thermal fluctuations as well as zero-point fluctuations leading to smoother dynamics. Generally, we observe that the observed spin transitions from a "coherent" (underdamped oscillatory) dynamics at weak system-bath coupling strength to "incoherent" (monotonic) decay at higher coupling. This transition depends on the spin-spin coupling, temperature, the location of the spin being observed in the chain and edge spins show considerable difference in the dynamics than the spins located in the interior of the chain. In contrast to the behavior of a single TLS coupled to a harmonic bath, the characteristics of the coherent-incoherent transition in the Ising chain are considerably more complex. With sufficiently large spin-spin coupling, once the damping effects are strong enough to prevent the magnetization of the interior spins to oscillate around the equilibrium value $\langle \sigma_z(\infty) \rangle = 0$, the evolution slows down considerably before eventually decaying, while edge spins may exhibit unusual oscillatory dynamics where the population oscillates above or below the equilibrium line.

The Hilbert space of an Ising chain containing n spins consists of 2^n states, thus there are over 10^3 states even for a rather short chain of $n \simeq 10$. While direct diagonalization of the Hamiltonian with such numbers of states is routinely feasible, the inclusion of harmonic baths to such a large system would result in an extremely challenging problem. Our calculations are based on the modular decomposition of the real-time path integral (MPI),[31-32] which links the TLS units sequentially, while allowing the full inclusion of bath degrees of freedom that couple to each spin. Throughout this work, we restrict attention to the paramagnetic phase.

3.2 Quantum Ising chain with spin-bath coupling

The isolated quantum Ising spin chain (with a transverse field) is described by the Hamiltonian:

$$\hat{H}_{\text{Ising}} = -\hbar\Omega\sum_{\alpha=1}^{n}\hat{\sigma}_x^{\alpha} - J\sum_{\alpha=1}^{n-1}\hat{\sigma}_z^{\alpha}\hat{\sigma}_z^{\alpha+1} \tag{3.1}$$

where $\hat{\sigma}_x$ and $\hat{\sigma}_z$ are the Pauli spin operators. This Hamiltonian describes a chain of n identical, symmetric TLSs connected through nearest-neighbor interactions. Each TLS has two localized states $|\uparrow\rangle$ and $|\downarrow\rangle$, which are eigenstates of $\hat{\sigma}_z$ with eigenvalues ±1. The Hamiltonian is characterized by two parameters, the tunneling parameter (or the transverse field) $\hbar\Omega$ (which is equal to half of the tunneling splitting of an individual TLS) and the nearest-neighbor spin-spin coupling strength J. In the context of magnetic materials, $\hbar\Omega$ is proportional to the magnitude of the transverse magnetic field, which flips the sign of the spin on which it operates, while J is the spin-spin magnetic interaction, which favors parallel (ferromagnetic, $J>0$) or anti-parallel (anti-ferromagnetic, $J<0$) alignment. The competition between the two terms governs the equilibrium structure and the dynamics. The Ω terms favor eigenstates where each spin is in a superposition of the "up" and "down" states, while the spin-spin coupling term J tries to align the spins. As a result, depending on the relation of these two parameters in the Hamiltonian, the infinite Ising chain undergoes a quantum phase transition at $J=\hbar\Omega$. Variations are expected in chains of finite length, where edge spins which couple to only one neighboring spin are less strongly aligned with those in the interior and the phase transition is broadened.

In this work we explore the role of model dissipative environments on the spin dynamics of the quantum Ising model by adding a harmonic bath to each spin. The total Ising + harmonic bath Hamiltonian is

$$\hat{H} = \hat{H}_{\text{Ising}} + \sum_{j}\frac{\left(\hat{p}_j^{\alpha}\right)^2}{2m_j} + \frac{1}{2}m_j^{\alpha}\omega_j^2\left(\hat{x}_j^{\alpha} - \frac{c_j\hat{\sigma}_z^{\alpha}}{m_j\omega_j}\right)^2 \tag{3.2}$$

In the present work, we use identical parameters for all the monomers in order to explore the dynamics of the quantum Ising chain, however the MPI methodology offers considerable flexibility and different parameter values for different monomers can be used. The parameters of the bath are collectively defined by the spectral density function[30]

$$J(\omega) = \tfrac{1}{2}\pi \sum_j \frac{c_j^2}{m_j \omega_j} \delta(\omega - \omega_j) \tag{3.3}$$

We choose the common Ohmic spectral density model, $J(\omega) = \tfrac{1}{2}\pi\hbar\xi\omega e^{-\omega/\omega_c}$, which has an exponential cutoff frequency ω_c and where the overall strength of TLS-bath coupling is characterized by the dimensionless Kondo parameter ξ. However, it should be emphasized that the MPI methodology may be used with any type of spectral density, and discrete normal mode vibrations may also be treated exactly. Initially all spins of the chain are placed in the $|\uparrow\rangle$ state, such that the initial density operator is

$$\hat{\rho}(0) = \prod_{\alpha=1}^{n} |\uparrow^\alpha\rangle\langle\uparrow^\alpha| \prod_j \frac{e^{-\beta\hat{h}_j^\alpha}}{\mathrm{Tr}\, e^{-\beta\hat{h}_j^\alpha}} \tag{3.4}$$

where

$$\hat{h}_j^\alpha = \frac{\left(\hat{p}_j^\alpha\right)^2}{2m_j} + \frac{1}{2}m_j\omega_j^2\left(\hat{x}_j^\alpha\right)^2 \tag{3.5}$$

is the Hamiltonian for the harmonic bath degrees of freedom that couple to spin α. The population of the "up" state of a particular spin is given by

$$P^\alpha(t) = \mathrm{Tr}\left\langle\uparrow^\alpha\left| e^{-i\hat{H}N\Delta t/\hbar}\hat{\rho}(0)e^{i\hat{H}N\Delta t/\hbar}\right|\uparrow^\alpha\right\rangle \tag{3.6}$$

where the trace is with respect to all degrees of freedom of the bath and the two spin states for all the spins except α and the magnetization of the observed spin is proportional to $\langle\sigma_z^\alpha(t)\rangle = 2P_\uparrow^\alpha(t) - 1$. Within the paramagnetic phase ($J < \hbar\Omega$), we refer to spin-spin coupling values as weak, intermediate or strong.

3.3 Methods

The results presented in the following sections use MPI[31-32] and SMatMPI[44] depending on the parameter regime. Both the methods are mentioned in Chapter 2. For coupling in the small to intermediate spin-spin coupling and spin-bath coupling, the original MPI algorithm was able to converge well. The convergence for large spin-spin coupling and strong dissipation, specially at low temperature turned out to be more challenging. Calculations in that regime were performed with the SMatMPI algorithm. Calculations for the isolated system (without bath) were performed using basis set methods.

3.4 Dynamics of the quantum Ising chain

The $\langle \sigma_z(t) \rangle$ for a single, symmetric TLS exhibits fully coherent tunneling oscillations between ± 1 which gets damped in the presence of dissipation from a harmonic bath. In the case for more than one TLS, by contrast, we observe that the same observable for a tagged spin shows damping even in the absence of a dissipative bath as the neighboring spins act as a dissipative environment to the particular spin being observed. In the case of a chain with n units, one generally expects to observe recurrences which should be pushed to longer time as n increases. Coupling to a harmonic bath leads to quenched oscillations even in the case of a single TLS, thus all spins in the quantum Ising chain exhibit dissipative dynamics and reach thermal equilibrium regardless of the number of units.

We are interested in the dynamical behavior of finite length Ising chains which can describe real molecular systems and where edge effects play a crucial role in determining the dynamics of the tagged spin. Here we explore the effect of the two Ising parameters, $\hbar\Omega$ and J (whose ratio determines the location of the quantum phase transition) on the resulting evolution, and the transition from underdamped to overdamped dynamics for edge and interior spins. We also investigate how coupling to a dissipative harmonic bath affects this transition as a function of the system-bath coupling strength and the temperature.

In this work we use a chain of $n = 10$ spins, each of which is coupled to an Ohmic bath characterized by the Kondo parameter ξ and cutoff frequency $\omega_c = 5\Omega$. The isolated Ising chain has 1024 eigenstates. The lowest eigenvalues of the isolated Ising chain are shown in Fig. 3.1. for weak, intermediate and strong spin-spin coupling (within the paramagnetic parameter space). For small values of J, the system has a ground state which is well separated from the cluster of singly excited states and a cluster of doubly excited states can also be identified. These clusters merge and the picture gets complicated as we go on increasing J until we reach phase transition at $J = \hbar\Omega$. (Things get clear again as we approach the ferromagnetic phase, but we deal with only the paramagnetic phase in this work.)
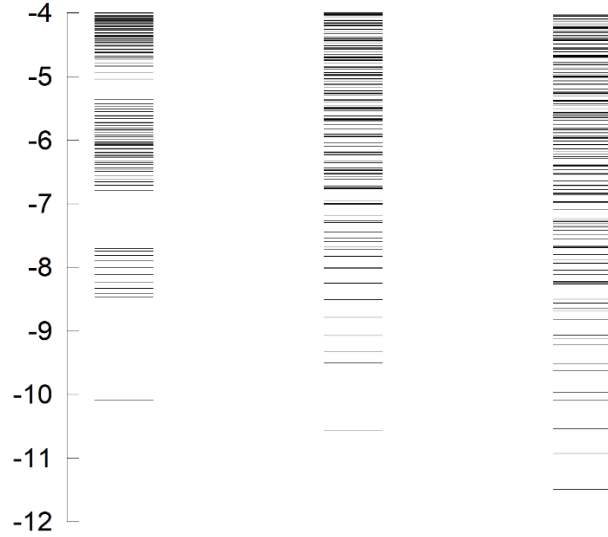

Fig. 3.1. Lowest 120-160 eigenvalues of the quantum Ising chain for $n = 10$ within the paramagnetic phase, in units of $\hbar\Omega$. Left: $J = 0.2\,\hbar\Omega$. Middle: $J = 0.5\,\hbar\Omega$ $J = 0.8\,\hbar\Omega$.

We simulate a quantum quench of a 10TLS Ising chain prepared initially in the ferromagnetic phase ($J > \hbar\Omega$) to a paramagnetic phase ($J < \hbar\Omega$) and thus characterize $J = 0.2\,\hbar\Omega$, $J = 0.5\,\hbar\Omega$, $J = 0.8\,\hbar\Omega$ as weak, intermediate and strong spin-spin coupling, respectively.

A. Weak spin-spin coupling

With $J << \hbar\Omega$ the spins interact only weakly. The behavior of the magentisation of a tagged spin in this case resembles that of a single spin attached to a dissipative bath at zero temperature, however, in the case of the Ising chain, we observe significant edge effects. Fig. 3.2. shows the time evolution of magnetization for the first five spins of an isolated 10 spin quantum Ising chain with $J = 0.2\,\hbar\Omega$ along with the magnetization of a single TLS coupled to a dissipative bath at zero temperature. All the spins display underdamped oscillatory dynamics over the time interval shown. The oscillation of the edge spin has a slightly larger amplitude than the interior spins as the edge spin only interacts with one neighboring monomer while the interior spins does with two. It is interesting to note that the amplitude doesn't vary monotonically with the location of a spin in the chain; the oscillation of the second spin is more damped than the third and the more interior spins.

Further, the dynamics of the edge spin is considerably more complex. While the first two oscillations are synchronized with those of the other spins, a jitter develops around the third peak, after which the edge spin oscillates out of phase. The second spin exhibits a somewhat similar but weaker effect and its oscillations remain almost synchronized with the edge spin. The interior spins display smoother dynamics which remain synchronized with each other and resemble a single underdamped oscillator with nearly identical populations. In this regime the effective damping on a spin induced by the other spins is reminiscent of that from a harmonic bath, which has been found to synchronize the oscillations of different *bath* degrees of freedom.[46]

Also shown in Fig. 3.2**.** is the magnetization dynamics of a TLS coupled to the a harmonic bath with $\xi = 0.1$ at zero temperature. This value of spin-bath coupling strength was chosen to produce dynamics similar to that of interior spins in the isolated Ising chain. It is seen that the damping effect of the spin environment on interior spins is overall similar to that of a harmonic dissipative bath with these parameters. However, the harmonic bath is more effective at decreasing the oscillation amplitude at short times.
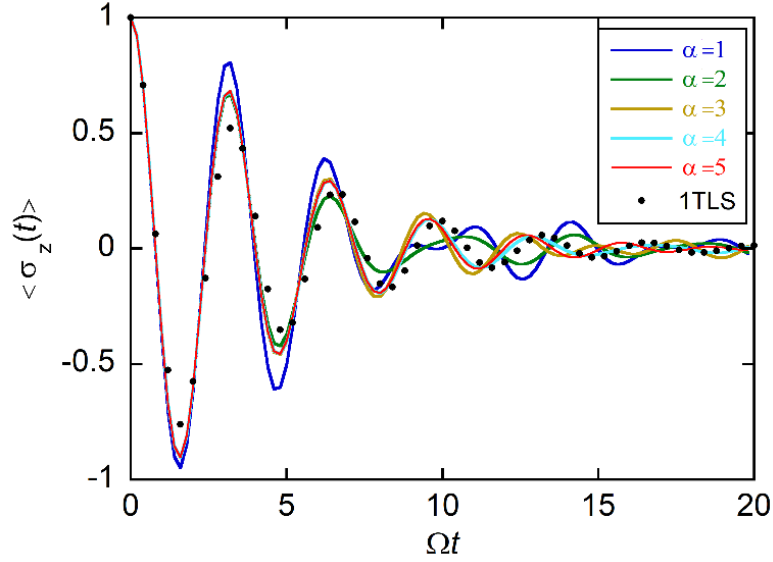
25

Fig. 3.2. Time evolution of magnetization of the first five spins of a 10 spin Ising chain with $J = 0.2\,\hbar\Omega$ (solid lines). Black dots show the same for one spin coupled to a harmonic bath with $\xi = 0.1$, $\omega_c = 5\Omega$, at zero temperature.

In Fig. 3.3. we show the magnetization for the Ising chain in the presence of dissipative harmonic baths attached to each spin with moderate strength, $\xi = 0.3$, at low ($\hbar\Omega\beta = 5$), intermediate ($\hbar\Omega\beta = 1$) and high ($\hbar\Omega\beta = 0.1$) temperatures. For comparison, the magnetization of the isolated chain is shown in this figure as well, on the same scale. The dissipative bath has a very pronounced effect on the coherence and at low and intermediate temperatures, all $\left\langle \sigma_z^\alpha \right\rangle$ oscillate below zero only once, and evolve to the equilibrium value after a very minor recurrence. The dissipative bath synchronizes the dynamics of all the spins (except the edge spin which shows a somewhat higher magnitude). The bath also slows down the oscillation of all spins; this effect is more prominent in the interior spins. At high temperature, all the spins exhibit indistinguishable dynamics.
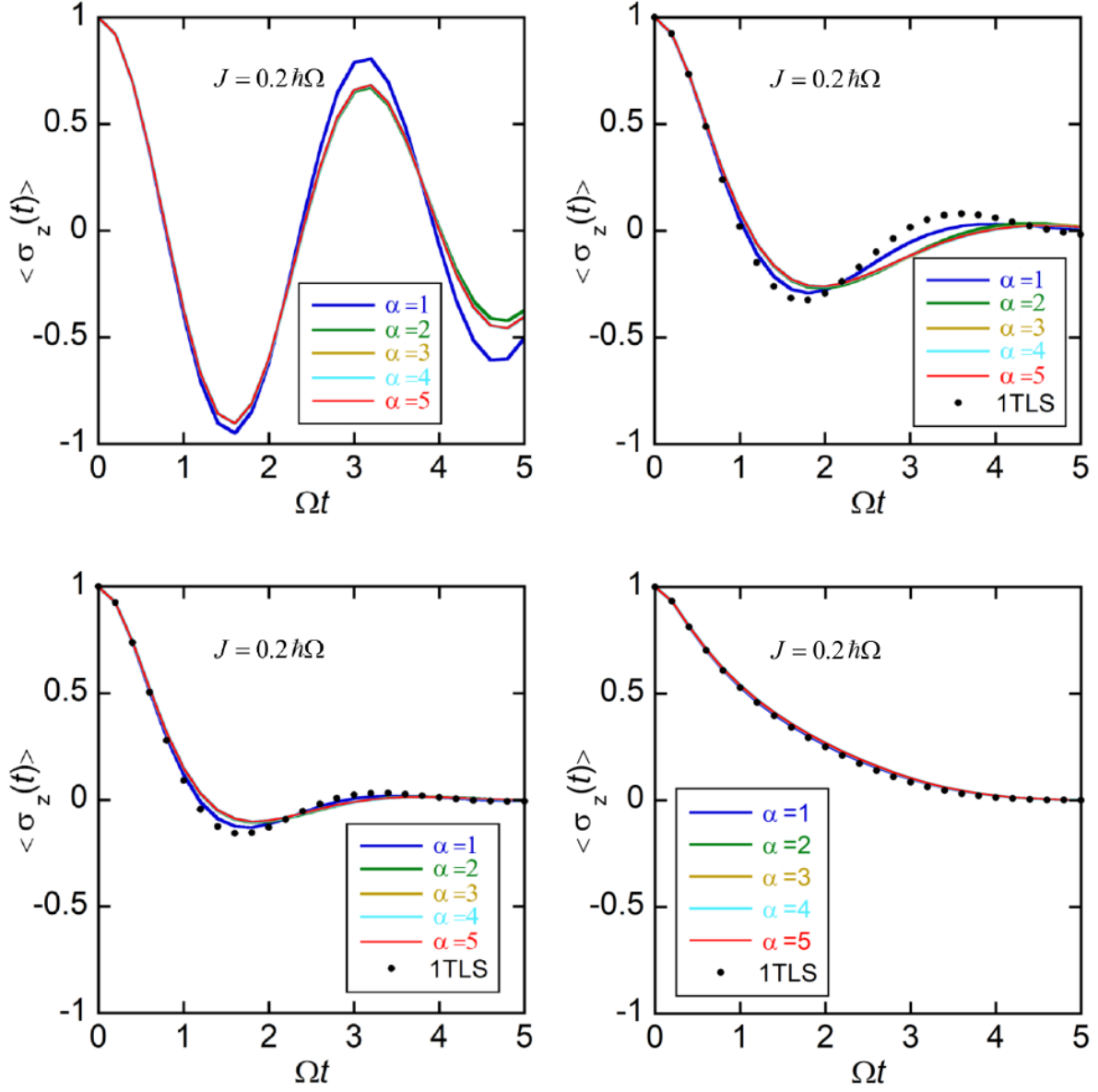
26

Fig. 3. 3. Magnetization in quantum Ising chains with $J = 0.2\,\hbar\Omega$ where each spin is coupled to a harmonic bath. The top left panel shows results in the absence of spin-bath coupling. The other three panels show results for a moderate spin-bath coupling value, $\xi = 0.3$. Top right: low temperature, $\hbar\Omega\beta = 5$. Bottom left: intermediate temperature, $\hbar\Omega\beta = 1$. Bottom right: high temperature, $\hbar\Omega\beta = 0.1$. Also shown are results for a single spin coupled to the same dissipative harmonic bath

For this case of very small spin-spin coupling, the moderate spin-bath interaction dominates the behavior of this system. It can be seen in Fig. 3.3. that the dynamics of a single spin coupled to a harmonic bath at the same temperature is not drastically different than the dynamics of a spin within the Ising chain, which has the spin-spin interactions along with the dissipative bath. However, the oscillations in presence of the harmonic bath, the oscillations are strongly damped compared to that of the isolated spin chain.

B. Moderate and strong spin-spin coupling

As the strength of the spin-spin coupling increases, the dynamics undergoes several notable changes. In the absence of dissipative baths, the major recurrence time of the $n=10$ chain shifts to earlier times, and with sufficiently large J moves within the time window displayed in the figures. Fig. 3.4. Shows the magnetization of an isolated n=10 Ising chain with $J = 0.5\hbar\Omega$ and $J = 0.8\hbar\Omega$. The coherence-quenching effects of the Ising chain on the short-time dynamics are now much more pronounced. The first oscillation minimum of the edge spin is deeper than that of interior spins, reflecting again the weaker damping effects on the spin coupled to the Ising chain only on one side. For the larger spin-spin coupling value $J = 0.8\hbar\Omega$, the dynamics for the second spin is different than the interior spins even during the first half oscillation. The short time amplitude is now seen to be monotonically dependent on the spin-position in the chain unlike that of the weak spin-spin coupling case. The magnetization minima of the second and third spins are also shifted to later times, indicating lowered characteristic frequencies. Interestingly, more complex evolution is observed at longer times, which is characterized by multiple frequencies that generate unique beating patterns.

Again, coupling to dissipative harmonic baths simplifies the dynamics and causes a gradual damping of the oscillatory behavior though the effect of a weakly or moderately dissipative bath does not dominate the dynamics observed with larger J values, and strong dissipation is needed to wipe out the patterns created by the strongly interacting spins.
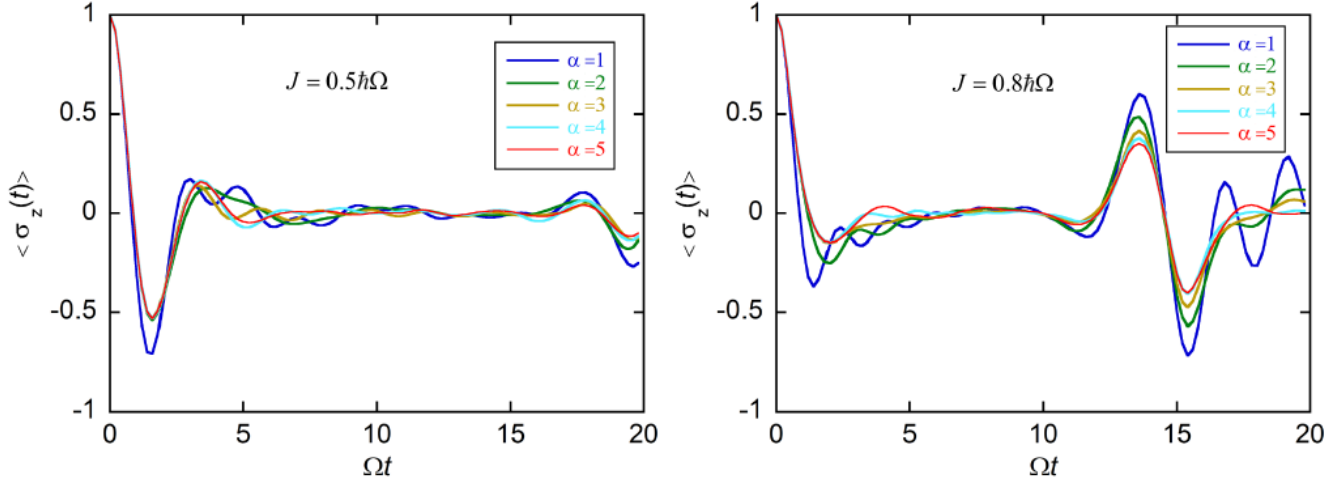
Fig. 3. 4. Magnetization of various spins in an isolated quantum Ising chain with moderately strong spin interactions.

Fig. 3.5. shows the magnetization for all spins in a chain with the moderate coupling value $J = 0.5\hbar\Omega$, which is coupled to a bath with $\xi = 0.3$ at three temperatures. Overall, the oscillatory behavior is more effectively suppressed here compared to the $J = 0.2\hbar\Omega$ case, and interior spins exhibit monotonic dynamics at all temperatures. The harmonic bath does not succeed at synchronizing the dynamics, and the first four spins are seen to oscillate with different frequencies and amplitudes. At the lowest temperature, the dissipative bath leads to moderately damped oscillatory dynamics for the edge spin, and a very shallow oscillation is observed in the magnetization of the second spin as well, while all interior spins display monotonic dynamics. Only the edge spin exhibits a slightly oscillatory behavior at the intermediate temperature, while incoherent decay is observed for all spins at the highest temperature.

Moving on to stronger spin-spin coupling, we see more complex patterns emerging in the dynamics. Fig. 3.6. shows the magnetization for an Ising chain with $J = 0.8\hbar\Omega$ coupled to baths characterized by $\xi = 0.1$, 0.3 and 0.5, at an intermediate temperature $\hbar\Omega\beta = 1$.
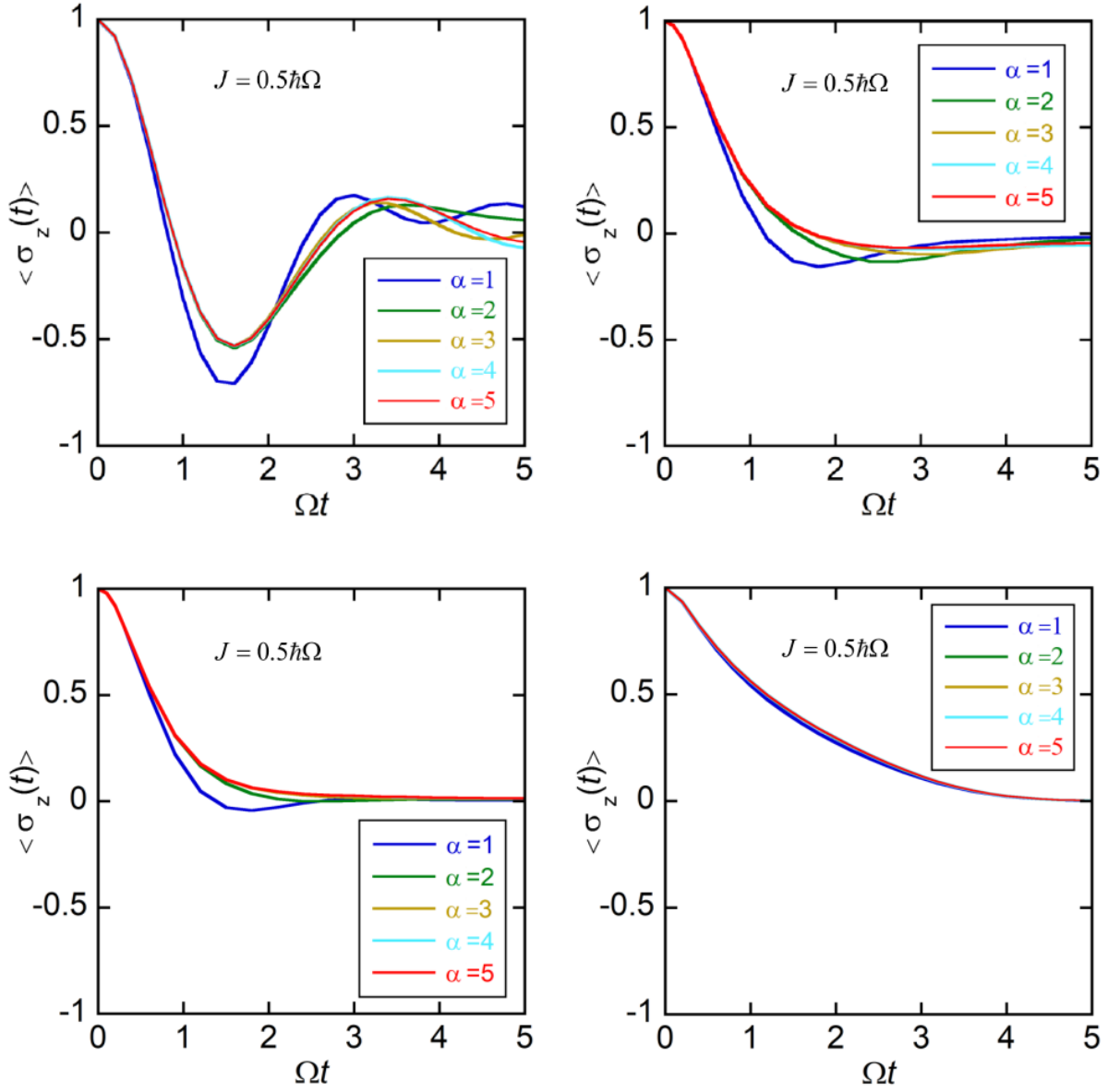
Fig. 3. 5. Magnetization of various spins in quantum Ising chains with $J = 0.5\hbar\Omega$ where each spin is coupled to a harmonic bath. The top left panel shows results for in the absence of spin-bath coupling. The other three panels show results for a moderate spin-bath coupling value, $\xi = 0.3$. Top right: low temperature, $\hbar\Omega\beta = 5$. Bottom left: intermediate temperature, $\hbar\Omega\beta = 1$. Bottom right: high temperature, $\hbar\Omega\beta = 0.1$.

The weakly dissipative bath leads to underdamped or overdamped dynamics depending on the position of the tagged spin in the chain, however the strongly dissipative bath alters the spin dynamics early on, almost stopping the population evolution for some time although the decay resumes later.

This behavior is more pronounced in interior spins and is amplified with increasing dissipative strength. In this regime, the population curves can often resemble a rotated sigmoidal function and can also exhibit oscillations where the magnetization oscillates about a value greater than zero.
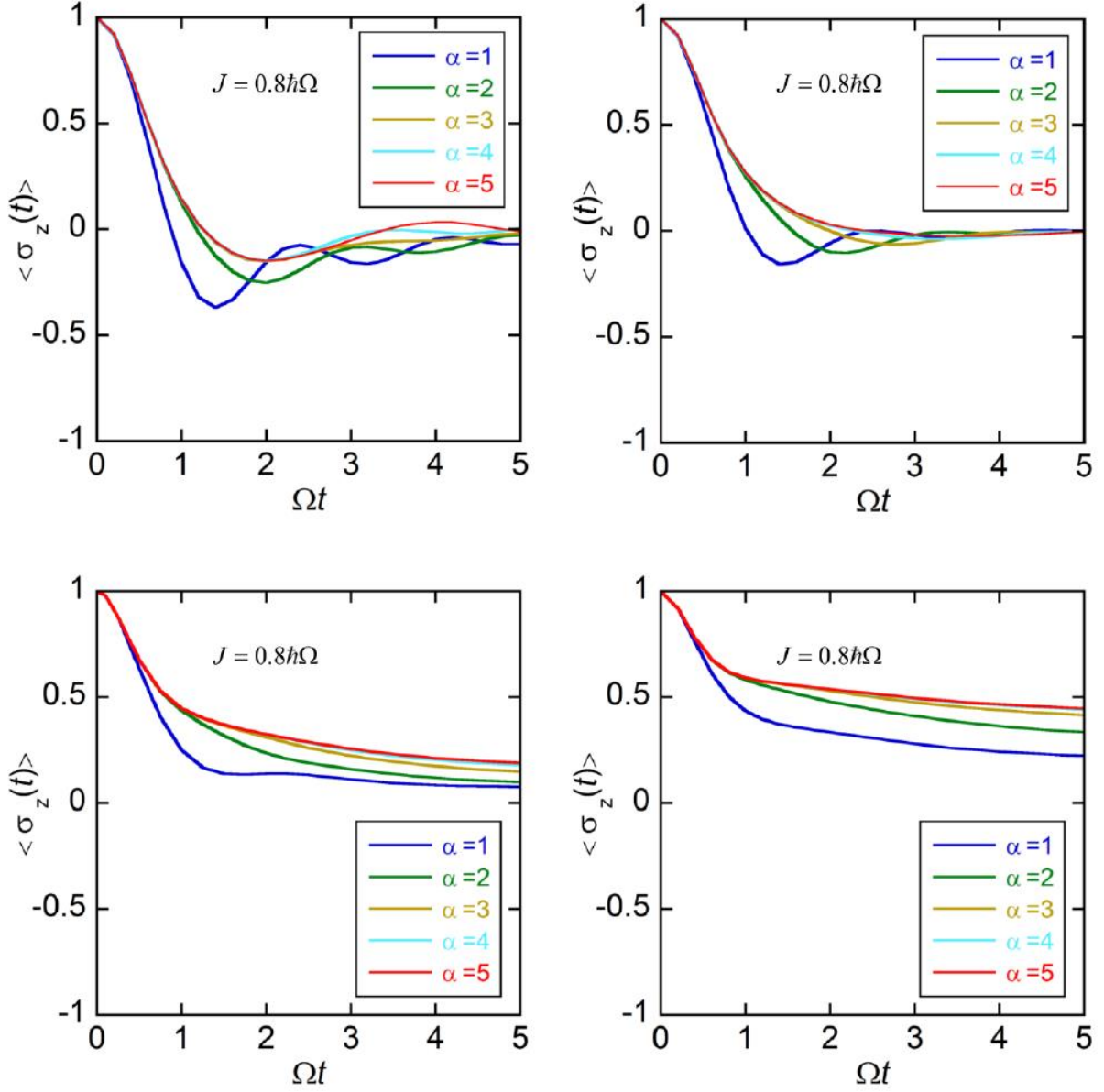

Fig 3. 6. Magnetization of various spins in quantum Ising chains with $J = 0.8\hbar\Omega$ where each spin is connected to a harmonic bath. The top left panel shows results for in the absence of spin-bath coupling. The other three panels show results at intermediate temperature $\hbar\Omega\beta = 1$. Top right: system-bath coupling parameter $\xi = 0.1$. Bottom left: $\xi = 0.3$. Bottom right: $\xi = 0.5$.

3.5 Transition from coherent to incoherent dynamics

We now turn our attention to the nature of dynamics depending on the spin-spin strength, spin-bath interaction, the temperature and the position of the spin in the chain. For small values of J, the magnetization dynamics of the edge spin is oscillatory with small ξ at low temperatures and eventually transitions to a monotonic decay as ξ and/or the temperature increases. However as J increases, the range of ξ values over which ordinary underdamped or monotonic oscillatory behavior is observed shrinks. With strong spin-spin and intermediate spin-bath coupling, the magnetization of the edge spin oscillates above or below the $\langle \sigma_z \rangle = 0$ value while decaying, giving rise to biased oscillatory dynamics at short times that resemble sigmoidal curves. This pattern is observed over a wider range of ξ values at low temperatures with stronger spin-spin coupling. At high spin-spin coupling and spin-bath coupling, the eventual decay of the magnetization slows down for all the spins. Here, we present magnetization dynamics in the parameter space where we can observe these interesting effects and we can eventually observe the dynamics go from "coherent" (common underdamped oscillatory) to "incoherent" (monotonically decreasing) which in some cases involves an intermediate "biased oscillatory" regime. Fig. 3.7. shows the magnetization of the edge spins near the boundaries of this coherent-incoherent transition with moderate and large spin-spin coupling at low, intermediate and high temperature. The biased oscillatory behavior which is mostly above but also below the equilibrium magnetization values (zero) is seen distinctly at low and intermediate temperatures. The regime of the overdamped oscillatory behavior decreases as temperature increases and at high temperatures, we see a direct transition from coherent to incoherent behavior. The sigmoidal curves and the very slow decay also disappear at high temperatures giving rise to simpler dynamics.

All of these behaviors are summarized in Fig. 3.8., which shows the three regimes on the J, ξ plane for edge and interior spins at low, intermediate and high temperatures. It should be noted that these hand drawn plots are primarily suggestive, and the boundaries are not sharp as the crossover from coherent to incoherent is a continuous one and the classification is subjective to some extent. The biased oscillatory

behavior is seen to occupy a large area of the plots for edge monomer at low temperatures, but this region becomes narrower as T is increased and eventually disappears. The interior spins, which are located far enough from the edges directly transition from coherent to incoherent behavior.

For $J = 0$ the Ising chain reduces to uncoupled spins, whose coherent-incoherent boundary at zero temperature is known[1] to be $\xi = \frac{1}{2}$. The coherent-incoherent boundary seen in Fig. 3.8. is $\xi \simeq 0.42$ at $J = 0.2\,\hbar\Omega$, which extrapolates to about 0.5 in the $J = 0$ limit, in agreement with the expected value.
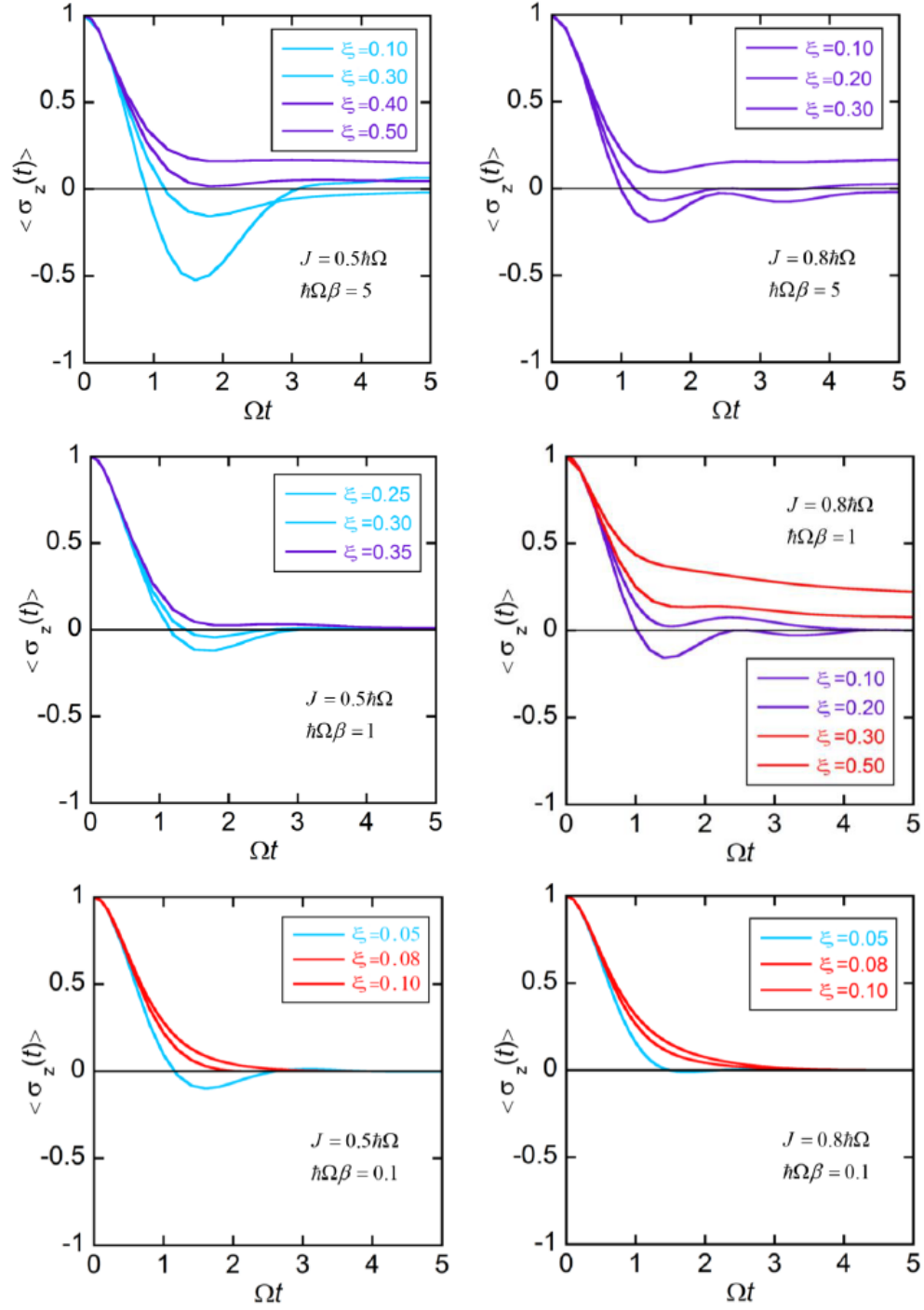
Fig. 3. 7. Edge spin population for moderate and strong spin-spin coupling at low, intermediate and high temperatures. Cyan: coherent regime. Purple: overdamped oscillatory regime. Red: incoherent regime.
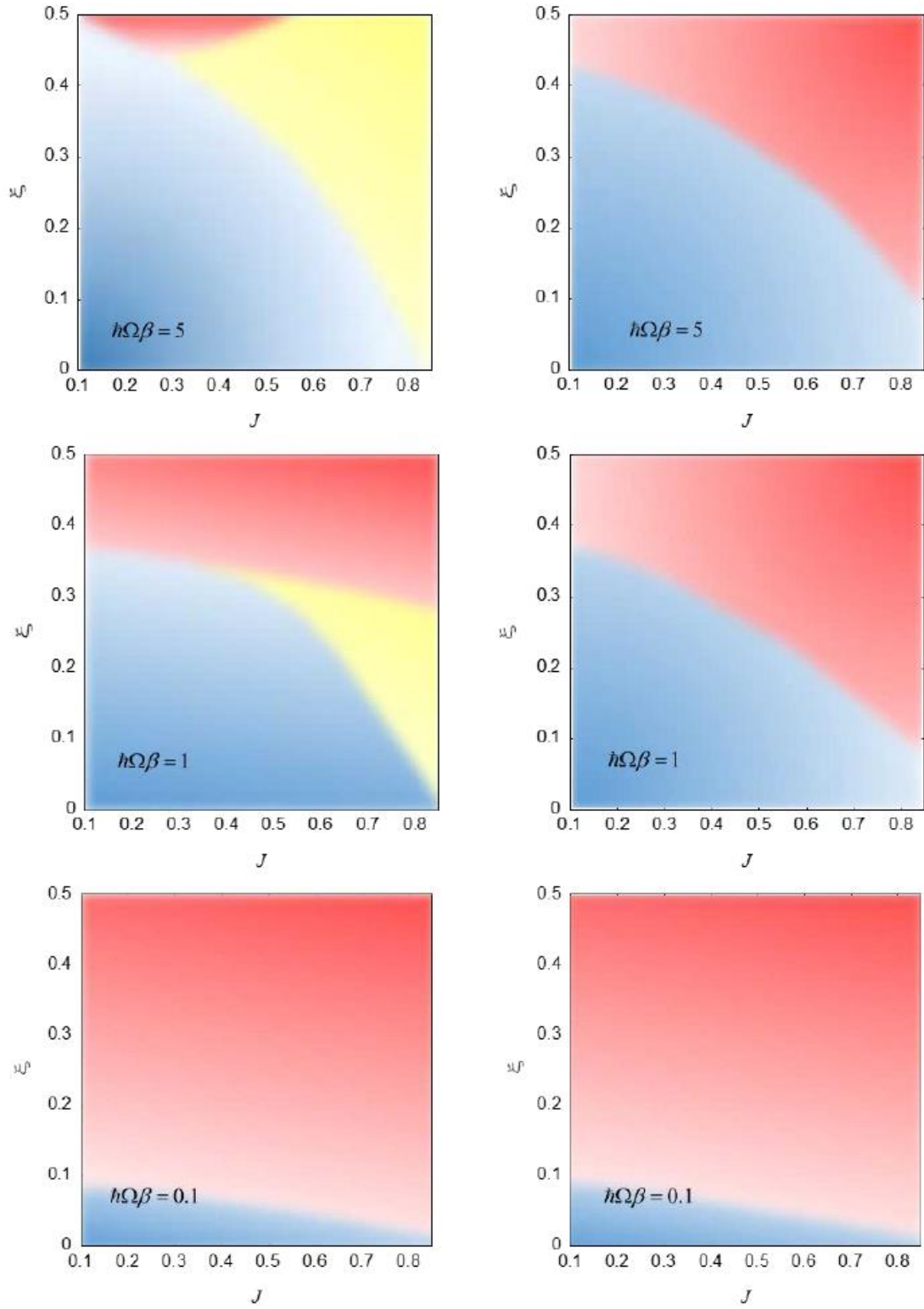
34

Fig. 3. 8. Coherent-incoherent diagrams for edge and interior spins at three temperatures. Left: Edge spins. Right: Interior spins. Cyan: coherent regime. Yellow: overdamped oscillatory regime. Red: incoherent regime.

3.6 Conclusions

In this work we have used fully quantum mechanical path integral methods to investigate the magnetization dynamics of individual spins in quantum Ising chains where each spin is coupled to a harmonic bath. This extends the well-known spin-boson tunneling dissipative dynamics to multiple spins in a one-dimensional chain. The spins were initially prepared in the aligned ferromagnetic phase and were evolved under a Hamiltonian characterizing a paramagnetic phase. The magnetization calculated thus describes the dynamics of a quantum quench experiment. We focused on the real time dynamics and the transition of dynamics from coherent to incoherent at different temperatures, spin-spin coupling, spin-bath coupling strength with particular emphasis on the variation of these properties with spin chains.

In the absence of a dissipative bath, the spin environment show damping effects on the observed spins and these effects are characteristically different from that of a dissipative bath. The spin state populations also don't die out and major recurrences occur at longer times. These times increase with the increase in the system size.

We also want to emphasize on the fact that the Ising chain bath differs from a bath of non-interacting TLS, each coupled to the observed spin. If the coupling parameters are scaled appropriately such that observables remain well-behaved in the thermodynamic limit,[47] such a spin bath displays a Gaussian response[48]. This can be mapped on to a harmonic bath with a definite spectral density.[49-51] However, the Ising spin bath doesn't affect the dynamics of the tagged spin in a way that might seem compatible to that of a harmonic bath.

Another interesting feature of the Ising chain is the dependence of the dynamics on the location of the tagged spin in the chain. Interior spins have two interacting spins on both sides, thus damping effects are more prominent for the interior spins. The dynamics of the edge spin which has only one

neighboring spin remains oscillatory over a wider range of temperatures and spin-bath coupling compared to the interior spins. Spins near the edge exhibit behavior which seem intermediate. However, in the case of an isolated spin chain, a nonmonotonic variation of amplitude with spin location is observed.

Coupling of the spins to dissipative harmonic baths leads to irreversible dynamics where the magnetization eventually approaches zero. In contrast, in the isolated spin chains, the magnetization of all spins saturates at $n \simeq 10$ over the range of parameters examined, such that the behaviors of the central spins presented in the previous two sections are representative of interior spin dynamics in long Ising chains.

Just as in the case of the spin-boson problem, the spin magnetization in Ising chains exhibits coherent (underdamped oscillatory) and incoherent (monotonically decaying) regimes, which depend on the system-bath coupling strength and the temperature. Because of the additional damping effects from the spin environment, the coherent regime spans a smaller portion of parameter space in comparison to the spin-boson case. Edge spins exhibit more complex behaviors than spins located in the interior of the chain.

With weak spin-spin coupling, and also for any value of J at high temperatures, edge-spin magnetization curves have underdamped oscillatory shapes or exhibit monotonic decay. However, with intermediate-to-strong spin-spin coupling, a third behavior is identified at intermediate and low temperatures, where the magnetization undergoes biased oscillatory evolution above or below the equilibrium value of zero. We have presented diagrams that illustrate these behaviors in the J vs. ξ plane at low, intermediate and high temperatures. We emphasize that the coherent-incoherent crossover is quite distinct from the ordered-disordered phase transition, which has been the subject of many earlier studies. The numerical results presented in this work offer a glimpse of the rich behaviors that characterize the dynamics of quantum Ising chains.

3.7 References

1) Leggett, A. J.; Chakravarty, S.; Dorsey, A. T.; Fisher, M. P. A.; Garg, A.; Zwerger, W., Dynamics of the dissipative two-state system. *Rev. Mod. Phys*. **1987**, *59*, 1−85

2) Escalera-Moreno, L.; Baldoví, J. J.; Gaita-Ariño, A.; Coronado, E., Spin states, vibrations and spin relaxation in molecular nanomagnets and spin qubits: a critical perspective. *Chem. Sci.* **2018**, *9* (13), 3265-3275

3) Dixey, R. J. C.; Orlandi, F.; Manuel, P.; Mukherjee, P.; Dutton, S. E.; Saines, P. J., Emergent magnetic order and correlated disorder in formate metal-organic frameworks. *Phil. Trans. R. Soc. A.* **2019**, *377* (2149), 20190007

4) Collins, K. A.; Saballos, R. J.; Fataftah, M. S.; Puggioni, D.; Rondinelli, J. M.; Freedman, D. E., Synthetic investigation of competing magnetic interactions in 2D metal–chloranilate radical frameworks. *Chem. Sci.* **2020**, *11* (23), 5922-5928

5) Thorarinsdottir, A. E.; Harris, T. D., Metal–organic framework magnets. *Chem. Rev.* **2020**, *120* (16), 8716-8789

6) Anthony, J. C.; Benjamin, P. J., Quasi-one dimensional magnetic interactions in the three-dimensional hyper-honeycomb framework [(C2H5)3NH]2Cu2(C2O4)3. *Phys. Chem. Chem. Phys.* **2021**,*23*, 5012-5019

7) Heisenberg, W., Zur theorie des ferromagnetismus *Z. Phys.* **1928**, *49*, 619-636

8) P. J. Low and S. Marqués-González, in *Single-Molecule Electronics: An Introduction to Synthesis, Measurement and Theory*, edited by M. Kiguchi (Springer Singapore, Singapore, 2016), pp. 87-116.

9) Frenkel, J., On the transformation of light into heat in solids. I *Phys. Rev.* **1931**, *37*, 17

10) de Gennes, P. G., Collective motions of hydrogen bonds. *Solid State Commun.* **1963**, *1* (6), 132-137

11) Coldea, R.; Tennant, D. A.; Wheeler, E. M.; Wawrzynska, E.; Prabhakaran, D.; Telling, M.; Habicht, K.; Smeibidl, P.; Kiefer, K., Quantum criticality in an Ising chain: Experimental evidence for emergent E_8 symmetry. *Sci.* **2010**, *327* (5962), 177-180

12) Simon, J.; Bakr, W. S.; Ma, R.; Tai, M. E.; Preiss, P. M., Greiner M., Quantum simulation of antiferromagnetic spin chains in an optical lattice. *Nat.* **2011**, *472* (7343), 307-312

13) Pfeuty, P., The one-dimensional Ising model with a transverse field. *Ann. Phys.* **1970**, *57* (1), 79-90

14) Dziarmaga, J., Dynamics of a quantum phase transition: Exact solution of the quantum Ising model. *Phys. Rev. Lett.* **2005**, *95*, 245701

15) Suzuki, S.; Inoue, J., Chakrabarty B. K., *Quantum Ising phases and transitions in transverse Ising models*, 2nd ed. (Springer-Verlag, Berlin-Heidelberg, 2013).

16) Fisher, D. S., Random transverse field Ising spin chains. *Phys. Rev. Lett.* **1992**, *69* (3), 534-537

17) Hoyos, J. A.; Vojta, T., Dissipation effects in random transverse-field Ising chains. *Phys. Rev. B* **2012**, *85* (17), 174403

18) Takada, K.; Nishimori, H., Critical properties of dissipative quantum spin systems in finite dimensions. *J. Phys. A* **2016**, *49*, 435001

19) Pang, S. Y.; Muniandy, S. V.; Kamali, M. Z. M., Critical dynamics of transverse-field quantum Ising model using finite-size scaling and matrix product states. *Intl. J. Theoret. Phys.* **2019**, *58* (12), 4139-4151

20) White, S. R., Density matrix formulation for quantum renormalization groups. *Phys. Rev. Lett.* **1992**, *69*, 2863

21) Schollwöck, U., The density-matrix renormalization group in the age of matrix product states. *Ann. Phys.* **2011**, *326*, 96-192

22) Isakov, S. V.; Mazzola, G.; Smelyanskiy, V. N.; Jiang, Z.; Boixo, S.; Neven, H.; Troyer, M., Understanding quantum tunneling through quantum Monte Carlo simulations. *Phys. Rev. Lett.* **2016**, *117* (18), 180402

23) Werner, P.; Völker, K.; Troyer, M.; Chakravarty, S., Phase diagram and critical exponents of a dissipative Ising spin chain in a transverse magnetic field. *Phys. Rev. Lett.* **2005**, *94* (4), 047201

24) Sachdev, S., *Quantum phase transitions*, Second ed. (Cambridge University Press, Cambridge, England, 2011).

25) Sengupta, K.; Powell, S.; Sachdev, S., Quench dynamics across quantum critical points. *Phys. Rev. A* **2004**, *69* (5), 053616

26) Calabrese, P.; Essler, F. H. L.; Fagotti, M., Quantum quench in the transverse field Ising chain: I. Time evolution of order parameter correlators. *J. Stat. Mech.: Theory and Experiment* **2012**, *7*, P07016

27) Calabrese, P.; Essler, F. H. L.; Fagotti, M., Quantum quenches in the transverse field Ising chain: II. Stationary state properties. *J. Stat. Mech.: Theory and Experiment* **2012**, *7*, P07022

28) Abeling, N. O.; Kehrein, S., Quantum quench dynamics in the transverse field Ising model at nonzero temperatures. *Phys. Rev. B* **2016**, *93*, 104302

29) Dorner, U.; Fedichev, P.; Jaksch, D.; Lewenstein, M.; Zoller, P., Entangling strings of neutral atoms in 1D atomic pipeline structures. *Phys. Rev. Lett.* **2003**, *91* (7), 073601

30) Caldeira, A. O.; Leggett, A. J., Path integral approach to quantum Brownian motion. *Physica A* **1983**, *121*, 587-616

31) Makri, N., Modular path integral methodology for real-time quantum dynamics. *J. Chem. Phys.* **2018** *149*, 214108

32) Makri, N., Communication: Modular path integral: Quantum dynamics via sequential necklace linking. *J. Chem. Phys.* **2018**, *148*, 101101

33) Feynman, R. P., Space-time approach to non-relativistic quantum mechanics. *Rev. Mod. Phys.* **1948**, *20*, 367-387

34) Feynman, R. P.; Hibbs, A. R., *Quantum Mechanics and Path Integrals*. (McGraw-Hill, New York, 1965).

35) Makri, N., Numerical path integral techniques for long time dynamics of quantum dissipative systems. *J. Math. Phys.* **1995**, *36*, 2430-2456

36) Makri, N., Quantum dissipative dynamics: A numerically exact methodology. *J. Phys. Chem.* **1998**, *102*, 4414-4427

37) Makri, N., Quantum-classical path integral: A rigorous approach to condensed phase dynamics. *Intl. J. Quant. Chem.* **2015**, *115*, 1209-1214

38) Feynman, R.P., Vernon, F.L., The theory of a general quantum system interacting with a linear dissipative system *Ann. Phys.***1963**, *24*, 118−173

39) Kundu, S.; Makri, N., Modular path integral for finite-temperature dynamics of extended systems with intramolecular vibrations. *J. Chem. Phys.* **2020**, *153*, 044124

40) Kundu, S.; Makri, N., Modular path integral for discrete systems with non-diagonal couplings. *J. Chem. Phys.* **2019**, *151*, 074110

41) Kundu, S.; Makri, N., Efficient matrix factorisation of the modular path integral for extended systems. *Mol. Phys.* **2021**, *119*, e1797200

42) Makri, N., Small matrix disentanglement of the path integral: Overcoming the exponential tensor scaling with memory length. *J. Chem. Phys.* **2020**, *152*, 041104

43) Makri, N., Small matrix path integral for system-bath dynamics. *J. Chem. Theory Comput.* **2020**, *16*, 4038–4049

44) Makri, N., Small matrix modular path integral: iterative quantum dynamics in space and time. *Phys. Chem. Chem. Phys.* **2021**, *23*, 12537-12540

45) Makri, N., Small matrix decomposition of feynman path amplitudes. *J. Chem. Theory Comput.* **2021**, *17* (7), 3825-3829

46) Kundu, S.; Makri, N., Time evolution of bath properties in spin-boson dynamics. *J. Phys. Chem. B* **2021**, *125* (29), 8137-8151

47) Suarez, A.; Silbey, R., Properties of a macroscopic system as a thermal bath. *J. Chem. Phys.* **1991**, *95*, 9115-9121

48) Makri, N., The linear response approximation and its lowest order corrections: An influence functional approach *J. Phys. Chem.* **1999**, *103*, 2823-2829

49) Shao, J.; Hänggi, P., Decoherent dynamics of a two-level system coupled to a sea of spins. *Phys. Rev. Lett.* **1998**, *81*, 5710

50) Forsythe, K.; Makri, N., Dissipative tunneling in a bath of two-level systems. *Phys. Rev. B* **1999**, *60*, 972-978

51) Wang, H.; Shao, J., Dynamics of a two-level system coupled to a bath of spins. *J. Chem. Phys.* **2012**, *137* (22), 22A504

Chapter 4

Excitation Energy Transfer in Bias-Free Dendrimers

4.1 Introduction

The search for renewable energy sources has resulted in a plethora of experimental and theoretical activity, aiming at designing molecular structures which can efficiently harvest and store solar energy. A major part of this effort focuses towards light harvesting apparatus found in photosynthetic plant and bacteria, which are known to transfer the absorbed light with high efficiency.[1-2] Ever since their discovery and characterization, light harvesting complexes have served as a paradigm for understanding the complex interplay between electronic states and vibrational motion which is the reason behind this observed energy transfer efficiency.[3-7] Understanding these systems with their intricate EET mechanisms can help in designing molecular structures for artificial light harvesting with diverse shapes and topologies. Dendrimers are one such class of molecules which offer a lot of promise as light harvesting systems.

Dendrimers are highly defined branched structures consisting of a core, repeat units and peripheral groups.[8-11] Their large volume compared to their molecular weight allows for encapsulation of guest molecules with specific functionality in their void, making them ideal candidates for drug delivery. Control of various important properties like density, shape, solubility, chirality and spectral characteristics can be obtained by a judicious choice of the building blocks and the peripheral functional groups that comprise the dendrimer. Apart from this, dendrimers are of interest as they can serve as an artificial energy antenna, their funnel-like structure aiding in funneling energy from the periphery to the core.

Theoretical investigations and simulations of these systems offer invaluable insights by providing useful structure-function relations and can aid experiments on light harvesting. The study of synthetic and natural light harvesting systems and excitation energy transfer has been the topic of study of several

theoretical studies.[12-15] Most of these studies focus on the model where each chromophore occupies a lattice site with nearest neighbor couplings between the sites.[16-19] But when the building blocks comprise of conjugated molecules, whose wavefunctions are delocalized over linear segments, a better model results by considering the nearest neighboring interactions between segments.[20] Electronic structure calculations have shown[20] that the interactions between segments can be mapped on the Frenkel exciton Hamiltonian and obtained parameters for the couplings between poly-phenylacetylene units[21-22] that comprise the nanostar.[8] There have been studies on the dynamical properties of dendrimer structures which include classical kinetic models,[23-24] quantum mechanical evolution using electronic Hamiltonian diagonalization or density matrix renormalization group[25] or tree tensor networks[26] and surface hopping approximation.[27-30] The multilayer multiconfiguration time-dependent Hartree method[31-32] and the time-dependent density matrix renormalization group approach[33] have enabled fully quantum mechanical studies of molecular aggregates comprising several chromophores with a few vibrational modes in each monomer at zero (and in some cases also at a low) temperature.[12,14,34-36] However, the complex interplay of the many energy and time scales found in these large molecular structures gives rise to a wide variety of behaviors, which cannot be predicted without accurate, fully quantum mechanical calculations. The vast size of thermally accessible electronic-vibrational Hilbert space prohibits the use of conventional wavefunction-based approaches when many low-frequency modes are present. Feynman's path integral formulation[37-39] offers unique capabilities for treating large numbers of vibrational degrees of freedom at any temperature. Real time path integral methods developed in the Makri group have been recently used to study EET through all-mode exciton-vibration calculations in the LH2 complex of purple bacteria,[46-47] in J aggregates of perylene bisimide[48-50] (PBI), in cofacial porphyrin dimers.[51] the striking finding of such all-state, all-mode path integral studies (where the exciton-vibration parameters were treated with their specific molecular values without simplification) is the complexity of the ensuing dynamics and the diversity of observed behaviors.[15]

In this work, we use quantum mechanical methods to investigate the eigenstate structure, thermodynamics and EET dynamics in model dendrimers composed of segments which interact via nearest neighbor Frenkel exciton interactions. The Frenkel model[57] has offered an excellent description of

dendrimers consisting of conjugated segments.[20] Most dendrimer work has focused on building up the structure in such a way that the segments decrease in energy as one approaches the center in order to create an effective energy funnel and accumulating the absorbed energy at the core. This energy funnel overcomes the entropic factor that favors accumulation of the energy on the periphery where there are more segments. In this work, we investigate structures which can show significant energy transfer towards the core even in the absence of an energetic bias. The entropic factor might totally rule this out, but the underlying argument is based on classical thermodynamics which doesn't consider the quantum mechanical nature of the dendrimer exciton states. We show that even in the absence of an energetic bias, the population distribution in the different generations of a dendrimer can be manipulated by controlling the electronic coupling parameters between the segments. This can be achieved by judicious incorporation of ligands at appropriate locations. One of the benefits of such a bias-free funnel architecture is the possibility of quantum coherence and interference which can alter EET dynamics and possibly even lead to faster dynamics.

We vary the strength and also consider different signs of the two types of couplings we see in these dendrimeric structures: intrageneration and intergeneration. We find that particular combinations of these parameters in the 3-fold topology of the typical dendrimer gives rise to unusual eigenstate structures dictated by frustrated effects like we encounter in spin systems. These characteristics are accompanied by a considerable slowing down of the EET dynamics.

4.2 Dendrimer Hamiltonian

Our work focuses on dendrimers with co-ordination number of 3 which gives rise to a three-branched structure. If a dendrimer has G generations, each generation possesses $3 \times 2^{G-1}$ segments with the total number of segments being $n = 3(2^G - 1)$. Fig. 4. 1. shows two such types of dendrimers: one with two generations ($G = 2$, $n = 9$) and one with three generations ($G = 3$, $n = 21$).
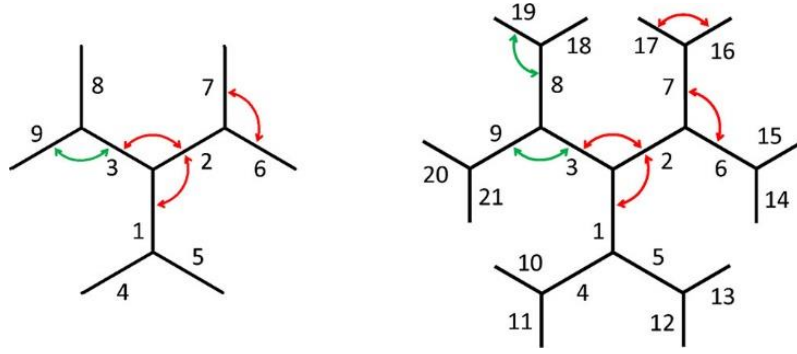
Fig 4.1. Two- and three-generation dendrimers ($G = 2$, $n = 9$ and $G = 3$, $n = 21$). Our numbering of the segments is shown. Intra-generation couplings are shown in red, while inter-generation couplings are shown in green.

Optical excitations in these dendrimers comprising of conjugated segments are localized and involve no charge transfer between segments[21] and the electronic Hamiltonian has the following Frenkel form:[57]

$$\hat{H}_{\mathrm{e}} = \sum_{\alpha=1}^{n} \varepsilon_{\alpha} |\alpha\rangle\langle\alpha| + \sum_{\alpha=1}^{n} \sum_{\beta>\alpha}^{n} J_{\alpha\beta} \left(|\alpha\rangle\langle\beta| + |\beta\rangle\langle\alpha| \right) \qquad (4.1)$$

where $|\alpha\rangle$ is the state with segment α excited, while all other segments are in the ground state, and $J_{\alpha\beta}$ are the exciton coupling parameters. Following earlier work, we assume that only connected (nearest neighbor) segments are coupled in Eq. 4.1. As mentioned earlier, in this work we explore the energy transfer in dendrimers in the absence of an energy bias and set $\varepsilon_{\alpha} = 0$. There are two types of segment-segment interactions as mentioned before: the intrageneration coupling J_{intra} between segments belonging to the same generation and the intergeneration coupling J_{inter} between segments belonging to different generations. Earlier work[22] has found that intra- and inter-generation couplings can change significantly with small variations of segment length and composition, and that these parameters may have opposite signs within the same dendrimer.

Intramolecular vibrations play a very important role in the dynamics of EET. Within the normal mode approximation, the ground and excited electronic states of each segment couple to intramolecular vibrations through the standard Hamiltonian[58]

45

$$\hat{h}_\alpha^g = \sum_i \left(\frac{\hat{p}_{i\alpha}^2}{2m} + \frac{1}{2} m\omega_{i\alpha}^2 \hat{q}_{i\alpha}^2 \right), \quad \hat{h}_\alpha^e = \sum_i \left[\frac{\hat{p}_{i\alpha}^2}{2m} + \frac{1}{2} m\omega_{i\alpha}^2 \left(\hat{q}_{i\alpha} - \frac{c_{i\alpha} s_e}{m\omega_{i\alpha}^2} \right)^2 \right] \quad (4.2)$$

where s_e is a parameter with units of length, $\hat{q}_{i\alpha}$ and $\hat{p}_{i\alpha}$ are the positions and momenta of the normal modes of segment α, and $\omega_{i\alpha}$, $c_{i\alpha}$ are the respective vibrational frequencies and exciton-vibration coupling strengths. The total Hamiltonian is given by

$$\hat{H} = \hat{H}_e + \sum_{\alpha=1}^n \left(\hat{h}_\alpha^e + \sum_{\beta \neq \alpha}^n \hat{h}_\beta^g \right) |\alpha\rangle\langle\alpha| . \quad (4.3)$$

The effects of molecular vibrations on exciton dynamics are collectively captured through the spectral density function $J(\omega)$. While the path integral methodology can fully account for vibrational modes characterized by their individual frequencies and coupling coefficients,[15] in the present model study we employ an Ohmic bath (discussed in Sec. 3.2.).

4.3 Methods

The system eigenstates and eigenvalue calculations were performed analytically using matrix diagonalization. The real time dynamics of these systems were performed using the small matrix decomposition[43-45] (SMatPI) of the quasi-adiabatic propagator path integral (QuAPI),[59-60] which is discussed in Chapter 2.

4.4 The building block

We begin by examining a three-segment structure (the central structure consisting of 1, 2, and 3 in Fig. 4.1). The electronic Hamiltonian for such a structure is given by:

$$\hat{H}_e = J_{12}\left(|1\rangle\langle 2| + |2\rangle\langle 1|\right) + J_{13}\left(|1\rangle\langle 3| + |3\rangle\langle 1|\right) + J_{23}\left(|2\rangle\langle 3| + |3\rangle\langle 2|\right) \tag{4.4}$$

In case of the bigger dendrimers in Fig. 4.1, all these three couplings are equal in value (J_{intra}). We can also consider an inter-generational block where $J_{12} = J_{13}$ and the third coupling J_{23} may have a different value. We thus set $J_{12} = J_{13} \equiv J$ and examine the eigenstates and the eigenvalues in several characteristic cases, illustrated in Fig. 4.2.
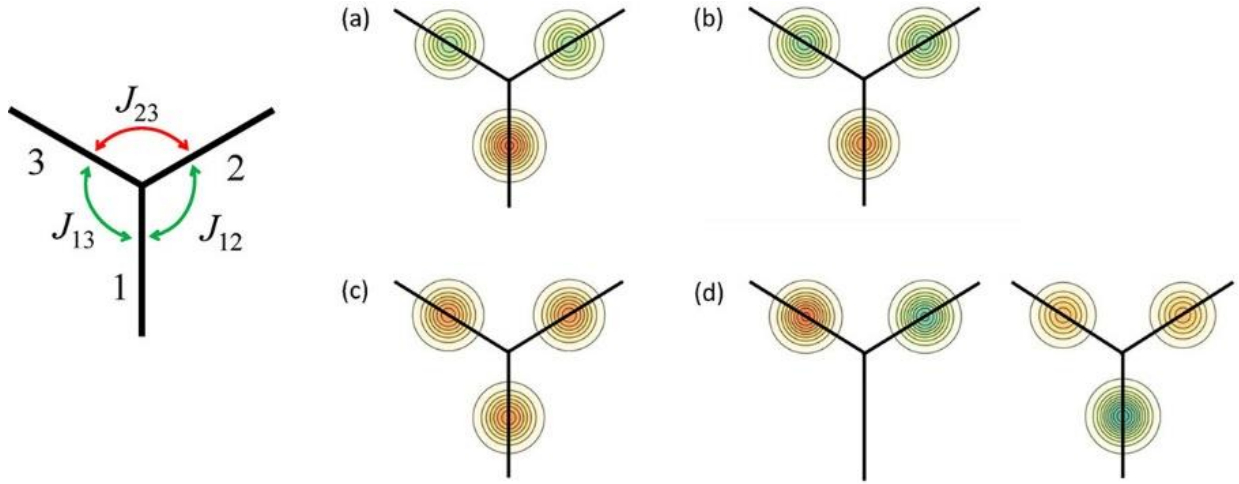

Fig. 4.2. Left: schematic illustration of three-segment block. Right: visualization of segment amplitudes in the ground state for four combinations of the coupling values. The component of the wavefunction on each is visualized by placing a Gaussian of proportional height on the center of the segment. Green and orange indicate positive and negative amplitudes. (a) $J_{12} = J_{13} > 0$, $J_{23} = 0$, (b) $J_{12} = J_{13} > 0$, $J_{23} = -J_{12}$, (c) $J_{12} = J_{13} = J_{23} < 0$, (d) $J_{12} = J_{13} = J_{23} > 0$

(i) $J_{12} = J_{13} = J$, $J_{23} = 0$. The eigenvalues and corresponding eigenstates are

$$\begin{aligned}
E_1 &= -\sqrt{2}|J|, \quad |\Phi_1\rangle = -\tfrac{\sqrt{2}}{2}\mathrm{sgn}(J)|1\rangle + \tfrac{1}{2}|2\rangle + \tfrac{1}{2}|3\rangle \\
E_2 &= 0, \quad |\Phi_2\rangle = \tfrac{1}{\sqrt{2}}|2\rangle - \tfrac{1}{\sqrt{2}}|3\rangle \\
E_3 &= +\sqrt{2}|J|, \quad |\Phi_3\rangle = +\tfrac{\sqrt{2}}{2}\mathrm{sgn}(J)|1\rangle + \tfrac{1}{2}|2\rangle + \tfrac{1}{2}|3\rangle
\end{aligned} \tag{4.5}$$

The eigenstate density does not depend on the sign of J, but the wavefunctions do and the highest and the lowest eigenstates swap signs upon changing this sign. For $J < 0$, the ground state is nodeless while for $J > 0$, the amplitudes on the different generations are of different signs (Fig. 4.2.a).

ii) $J_{12} = J_{13} = J$, $J_{23} = -|J|$. The eigenvalues and eigenstates are

$$
\begin{aligned}
E_1 &= -2|J|, \quad |\Phi_1\rangle = -\tfrac{1}{\sqrt{3}}\mathrm{sgn}(J)|1\rangle + \tfrac{1}{\sqrt{3}}|2\rangle + \tfrac{1}{\sqrt{3}}|3\rangle \\
E_2 &= |J|, \quad |\Phi_2\rangle = \tfrac{1}{\sqrt{2}}|2\rangle - \tfrac{1}{\sqrt{2}}|3\rangle \\
E_3 &= |J|, \quad |\Phi_3\rangle = \tfrac{2}{\sqrt{6}}\mathrm{sgn}(J)|1\rangle + \tfrac{1}{\sqrt{6}}|2\rangle + \tfrac{1}{\sqrt{6}}|3\rangle
\end{aligned}
\tag{4.6}
$$

The $J > 0$ case applies to the smallest building block with one segment in one generation and two in the next generation. The ground state in this case has opposite amplitudes on the two generations, is doubly degenerate and the negative intra-generation coupling stabilizes the system. (Fig. 4.2.b). And for $J < 0$, we get a nodeless ground state (Fig. 4.2.c).

(iii) $J_{12} = J_{13} = J_{23} = J > 0$. In this case (Fig. 2d) we find

$$
\begin{aligned}
E_1 &= -J, \quad |\Phi_1\rangle = -\tfrac{2}{\sqrt{6}}|1\rangle + \tfrac{1}{\sqrt{6}}|2\rangle + \tfrac{1}{\sqrt{6}}|3\rangle \\
E_2 &= -J, \quad |\Phi_2\rangle = \tfrac{1}{\sqrt{2}}|2\rangle - \tfrac{1}{\sqrt{2}}|3\rangle \\
E_3 &= 2J, \quad |\Phi_3\rangle = \tfrac{1}{\sqrt{3}}|1\rangle + \tfrac{1}{\sqrt{3}}|2\rangle + \tfrac{1}{\sqrt{3}}|3\rangle
\end{aligned}
\tag{4.7}
$$

The ground state is now doubly degenerate and is destabilized. The positive intergeneration coupling causes the segments 2 and 3 to have opposite signs which is not favorable for the positive intrageneration coupling. This causes this trimer to exhibit frustration – an effect analogous from interacting spin systems.

When all three couplings have the same magnitude equal to J, the evolution of electronic populations following excitation of one segment is given by

$$
P_\alpha(t) = \frac{1}{9}\left[5 + 4\cos\left(3J\,t/\hbar\right)\right]
\tag{4.8}
$$

regardless of the relative signs.

To summarize this section, eigenstate densities are insensitive to the sign of the intergeneration couplings in a trimer, but the spectrum and the ground state structure change drastically when the third coupling, the intrageneration coupling reverses sign. A negative intrageneration stabilizes the structure, while a positive value destabilizes the system and gives rise to a pair of degenerate ground states. We now turn to larger dendrimers and use numerical diagonalization to study the eigenstates of the electronic Hamiltonian.

4.5 Eigenvectors and equilibrium distributions

In this section we investigate the eigenstate structure and equilibrium populations of dendrimer of varying size. We set $J_{inter} = J > 0$, but consider different magnitudes and signs of J_{intra}. We examine the ground state(s) and some select excited states for a 21 segment three generation dendrimer. In addition, we also show the population distribution of the electronic Hamiltonian in each generation of dendrimers comprising of two to four generations at zero temperature and also at $k_B T = 0.2J, \; J, \;$ and $10J$. The first of the finite temperatures is very low for typical values of the inter-generation coupling ($50\text{-}500\,\mathrm{cm}^{-1}$). Yet, we find that with particular choices of J_{intra}, the populations are drastically different from those obtained at zero temperature. The electronic Hamiltonian of the dendrimer is in the high temperature regime at $k_B T = 10J$ for all the coupling values considered in this work. We find that at this temperature, the population distribution is statistical, and all segments have equal populations, thus each generation has twice the population as the previous one (as every segment branches to two in the next generation). Classical hopping approximation[23-24] have produced such high-temperature results. As will be seen in the figures presented in this section, the quantized electronic Hamiltonian gives rise to entirely different population distributions at low and intermediate temperature. It is thus natural to expect quantum effects will be very prominent in the population distribution and also in the EET dynamics.
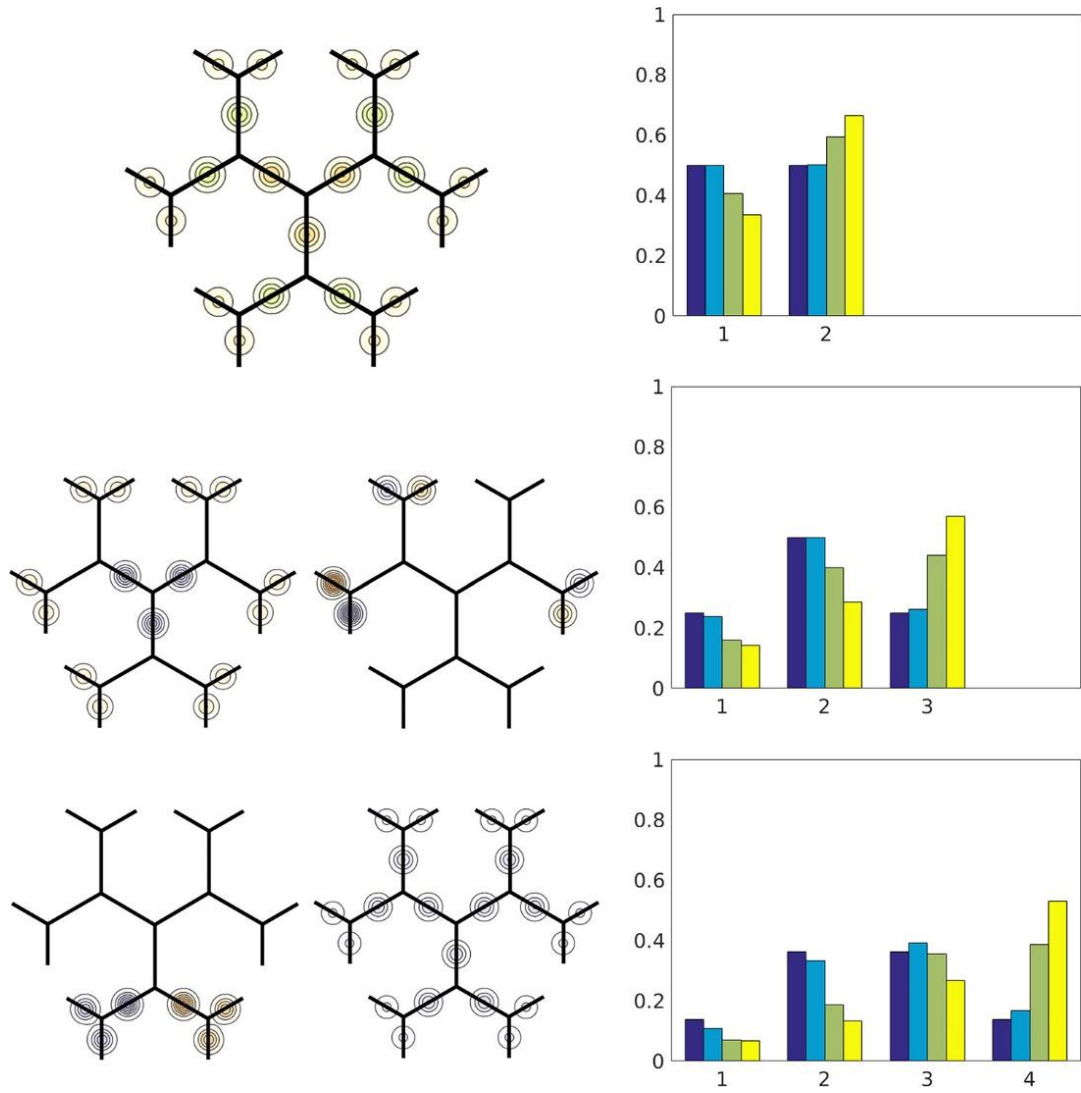
Fig. 4.3. Visualization of segment amplitudes and population distribution for $J_{\text{intra}} = 0$. Left: eigenstates amplitudes on the various segments of a three-generation dendrimer. All eigenstates are three-fold degenerate. The larger image shows the ground state Φ_1, while the smaller four images show eigenstates $\Phi_7, \Phi_{12}, \Phi_{16}$, and Φ_{19}. Orange/green and blue/orange correspond to positive and negative amplitudes. Right: total population in each generation for a two (top), three (middle) and four generation (bottom) dendrimer at various temperatures. Dark blue: T=0. Cyan: $k_{\text{B}}T = 0.2J$. Green: $k_{\text{B}}T = J$. Yellow: $k_{\text{B}}T = 10J$.

(i) All $J_{\text{intra}} = 0$. Since none of the core segments have any coupling between them, this is the case of three unconnected dendrimer branches. The eigenstates in this case are all three-fold degenerate. With proper linear combinations, the wavefunctions are delocalized over the entire dendrimer. The ground state

wavefunctions have circular nodes between generations, while the highest lying excited states are nodeless (Fig. 4.3.).
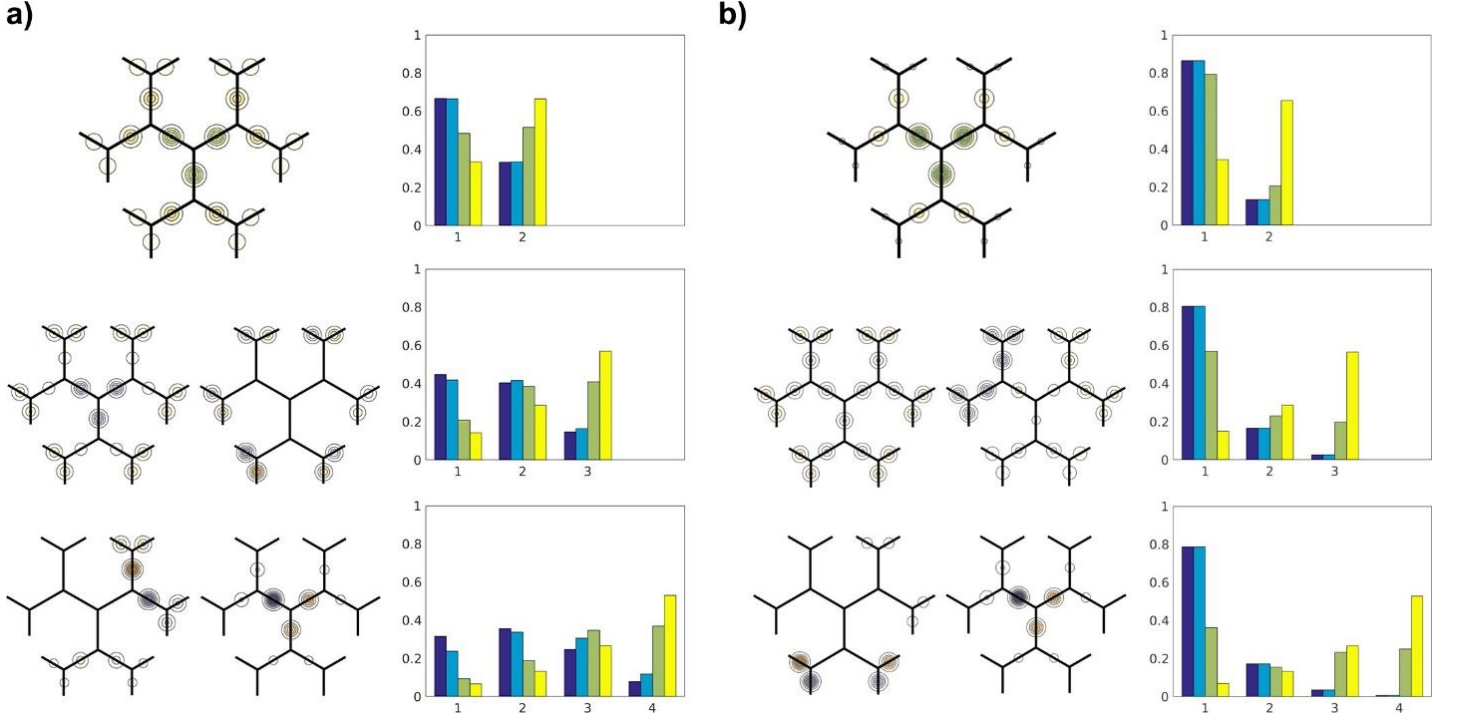

Fig. 4.4. Visualization of segment amplitudes and population distribution for (a) $J_{\text{intra}} = -J$ and (b) $J_{\text{intra}} = -3J$. Left: eigenstate amplitudes on the various segments for a three-generation dendrimer. The larger images show the ground state Φ_1, while the smaller images show the eigenstates (a) $\Phi_7, \Phi_{11}, \Phi_{18}, \Phi_{20}$ and (b) $\Phi_4, \Phi_9, \Phi_{16}, \Phi_{20}$. Orange/green and blue/green indicate positive and negative amplitudes. Right: total population in each generation for a two (top), three (middle) and four generation (bottom) dendrimer at various temperatures. Dark blue: T=0. Cyan: $k_{\text{B}}T = 0.2J$. Green: $k_{\text{B}}T = J$. Yellow: $k_{\text{B}}T = 10J$.

(ii) $J_{\text{intra}} < 0$. In this case the eigenstates maintain the spreading and alternating sign features observed with $J_{\text{intra}} = 0$, but the threefold degeneracy is lifted. Fig.4.4. shows the eigenfunctions and equilibrium population distributions for $J_{\text{intra}} = -J$ and $-3J$. As expected from the discussion in the previous section, increasing the intra-generation coupling stabilizes the dendrimer, lowering the ground state energy and increasing the population in the core segments. With these values of J_{intra}, the two-generation dendrimer

has most of its population in the inner core generation at zero temperature. The populations change non-monotonically with generation number as the temperature is increased, eventually approaching the statistical limit. In large dendrimers, we see population moving away from the inner generation (entropic effect), though this effect is countered by increasing the value of J_{intra}, which pushes more population towards the inner generations. With $J_{intra} = -3J$ the core population is maintained above or slightly below 0.8 for the $G = 2, 3, 4$ dendrimers examined. With $J_{intra} < 0$, we see that at $k_B T = 0.2J$, the core population in every dendrimer is close to that at T=0.

(iii) $J_{intra} > 0$. There is a drastic change in the behavior when the intrageneration coupling is positive, which can be seen in Fig. 4.5. Similar to the three-segment dendrimer with a positive intrageneration coupling, here we see a doubly degenerate ground state that don't show the three-fold symmetry of the dendrimer structure. This results from frustration within the generations. As seen in Fig. 4.5., one of the two ground states is now distributed on only two of the three branches. These dendrimers show a competition between delocalization and frustration leading to the outcome of pushing the ground state population towards the core generation, attempting to minimize the population on the periphery which has the highest number of interacting segments. As a result, at zero temperature, there is an accumulation of population in the dendrimer core. The core population here at T = 0 is higher than that of equivalent cases of $J_{intra} < 0$, and increases with increasing J_{intra}. Further, the shift of population away from the core with increasing dendrimer size is weaker in this case, especially when $J_{intra} = 3J$.

However, there are now eigenstates with large densities in the second generation which are very close in energy to the ground states. These eigenstates are rapidly populated upon increasing the temperature, decreasing the core population. We can see that even at the very low temperature $k_B T = 0.2J$ the core population with $J_{intra} = 3J$ drops to about 0.15, compared to 0.95 at $T = 0$, and the maximum population is found in the third generation. Thus, the population of the core segments is overall larger with

$J_{\text{intra}} > 0$ in comparison to identical dendrimers with negative intra-generation couplings, the trend reverses rapidly when finite temperature is introduced, and the excitation energy approaches the statistical limit faster in this case.
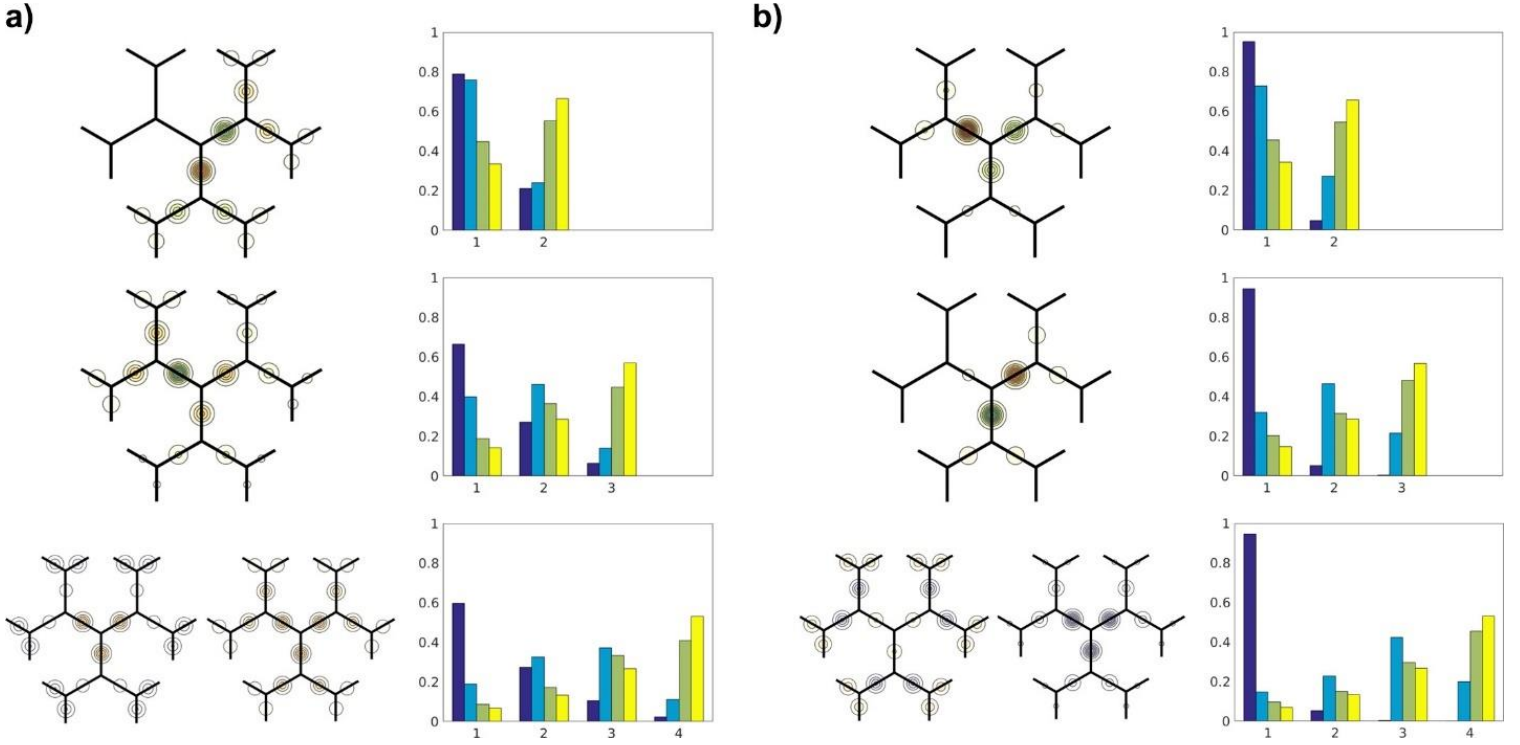

Fig. 4.5. Visualization of segment amplitudes and population distribution for (a) $J_{\text{intra}} = +J$ and (b) $J_{\text{intra}} = +3J$. Left: eigenstate amplitudes on the various segments for a three-generation dendrimer. The larger images show the degenerate ground states Φ_1 and Φ_2, while the two smaller images show the excited eigenstates (a) Φ_{15}, Φ_{21} and (b) Φ_{12}, Φ_{21}. Green/orange and blue/green show the positive and negative amplitudes. Right: Total population in each generation for a two (top), three (middle) and four generation (bottom) dendrimer at various temperatures. Dark blue: T=0. Cyan: $k_B T = 0.2J$. Green: $k_B T = J$. Yellow: $k_B T = 10J$.

4.6. Dynamics of exciton energy transfer

We now shift our attention to the real time dynamics of excitation energy following the excitation of a peripheral segment. The population evolution as we found doesn't depend on the sign of the intergeneration coupling and we set it to $J_{\text{inter}} = J = 300\,\text{cm}^{-1}$ (a value in the range expected for such

systems). We consider both positive and negative intrageneration coupling, $J_{\text{intra}} = \pm 300 \, \text{cm}^{-1}$. We also assume that that vibrational energy peaks at $\omega_c = 1500 \, \text{cm}^{-1}$ and consider two values of reorganization energy: a moderate value $\lambda = J = 300 \, \text{cm}^{-1}$ and $900 \, \text{cm}^{-1}$. We examine the three-segment dendrimer at 100K and then move on to examining the dynamics of a 9 monomer G=2 dendrimer at 100K (corresponding to $J / k_B T = 4.31$), 300K ($J / k_B T = 1.44$) and 1000K ($J / k_B T = 0.431$).
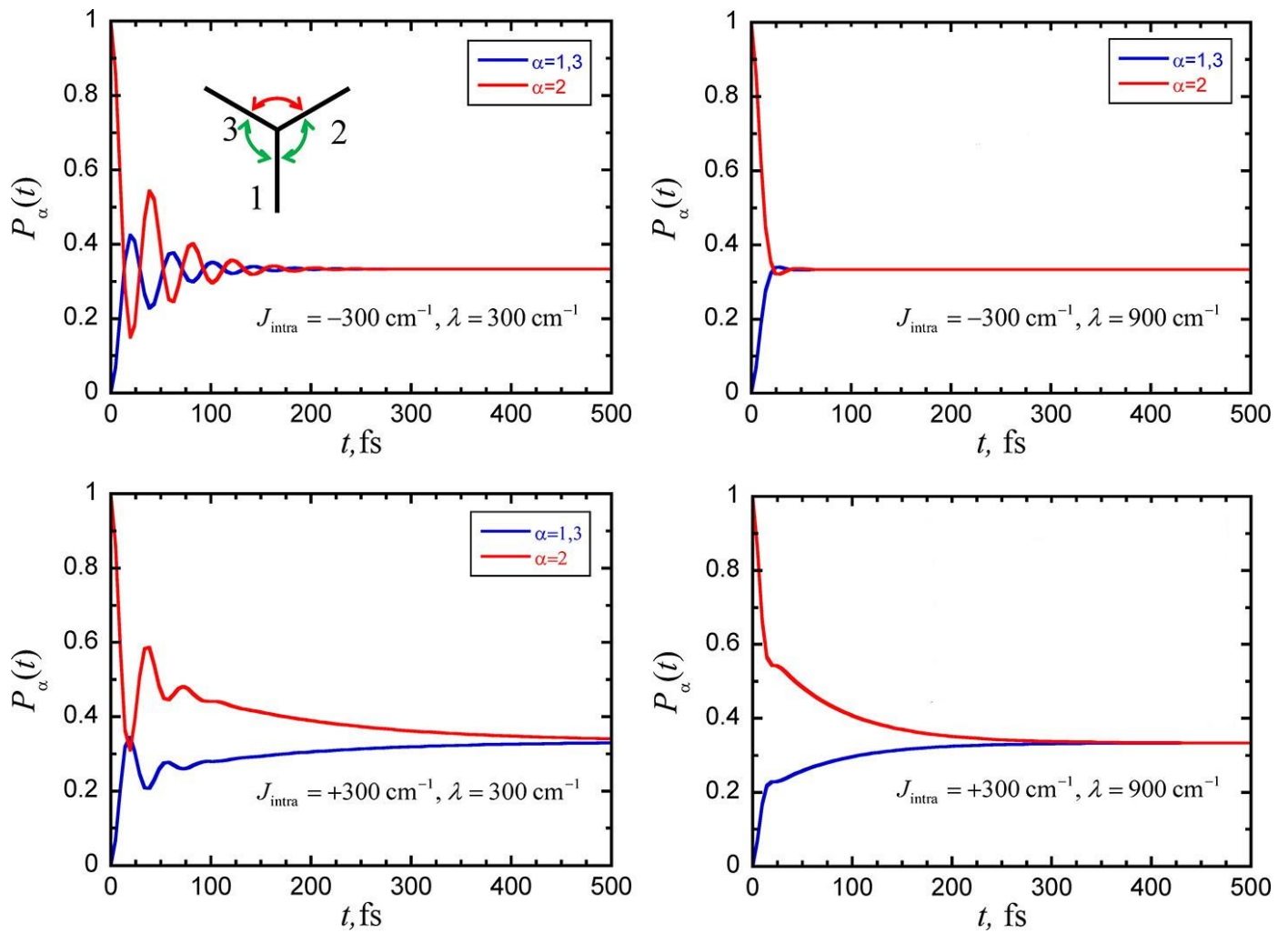

Fig. 4.6. Excited segment populations as a function of time following excitation of segment 2 for a trimer with the parameters given in the text at 100K.

Fig. 4.6. shows the dynamics for the two kinds of three-segment dendrimer (Fig. 4.2.b and 4.2.d) where two pair of segments interact through J_{inter} while the third pair couples through $J_{intra} = \pm 300 \, cm^{-1}$ at 100K. In all the cases, the excitation energy is initially localized on the 2nd segment and we can see that they equilibrate fairly rapidly (within 0.5ps) to 1/3 on all the segments. However, the dynamics they follow to reach this equilibrium is very different for all the four cases. With the weaker exciton-vibration coupling at 300 cm^{-1}, the dynamics is underdamped and oscillatory more so for $J_{intra} < 0$, but this oscillatory feature is lost upon increasing this coupling to 900 cm^{-1}. It is interesting to note that even though we just present results for 100K, there is only a mild reduction in the oscillations at 300K. This is so because while this temperature is moderate with respect to the exciton coupling parameters, it is still low with respect to the vibrational coupling, thus providing inadequate damping.

The most striking difference seen in Fig. 4.6. is the lengthening of the EET relaxation time when $J_{intra} > 0$, compared to the dynamics with $J_{intra} < 0$ (of the same magnitude) and all other parameters fixed. Two distinct time scales are very clearly evident for $J_{intra} > 0$, especially with $\lambda = 900 \, cm^{-1}$. Regardless of the sign of J_{intra}, we observe a fast population transfer out of the initially excited state in the initial 15fs. For $J_{intra} < 0$, the subsequent transfer is rapid and uneventful, and the population equilibrates within 50fs. However, when $J_{intra} > 0$, the population transfers to a slow decay, reaching equilibrium at approximately 300fs, a six-fold slowdown. The relaxation is even slower when the reorganization energy is lower, the energy transfer lasting 500fs.
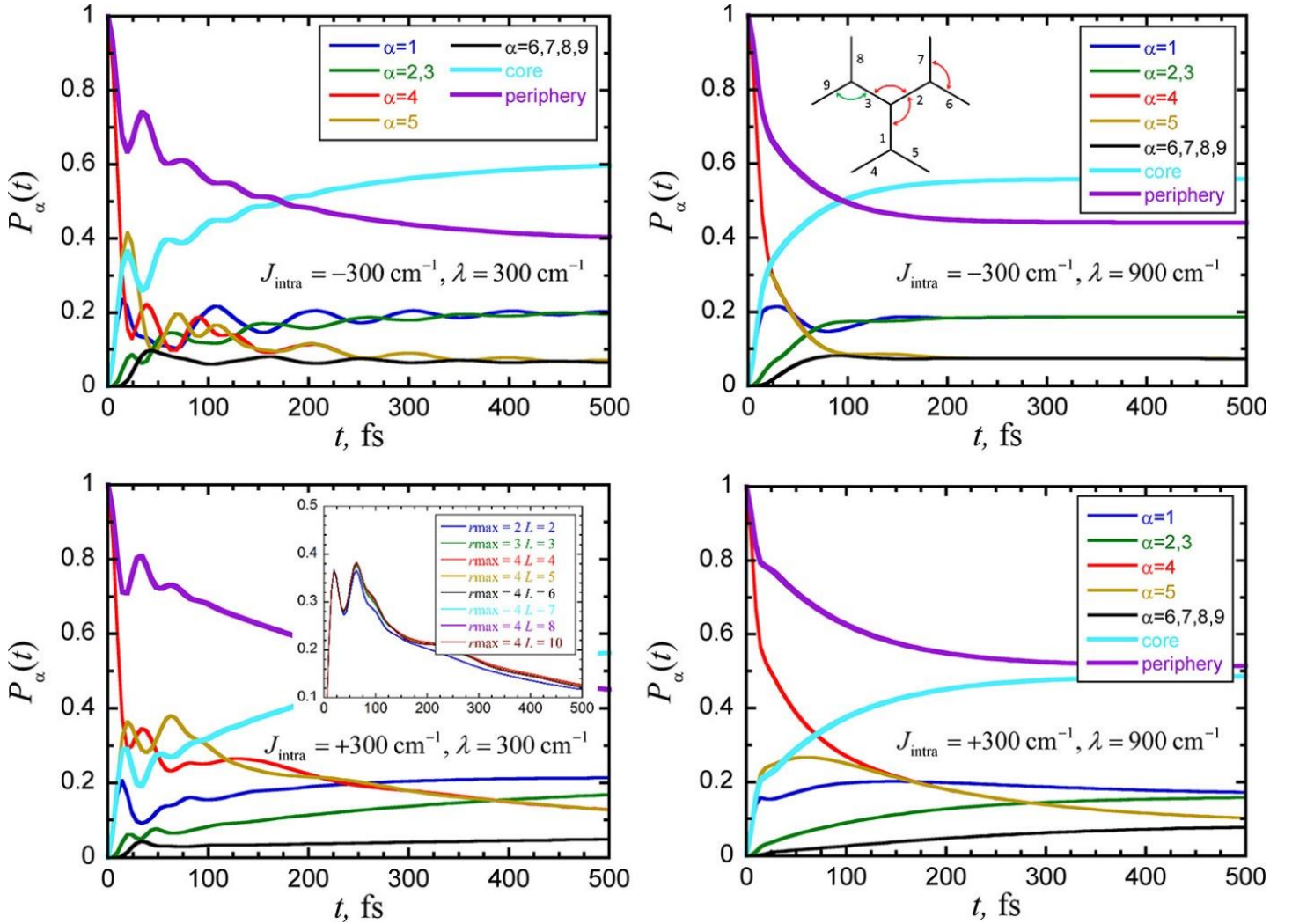
Fig. 4.7. Energy transfer dynamics in $G = 2$ dendrimers with the parameters given in the text at $T = 100\ \mathrm{K}$. For convenience we show the dendrimer structure with segment numbers in one of the panels. The inset shows the convergence of P_5 for various values of the SMatPI entanglement length r_{max} and memory length L.

It is interesting to note that, as discussed in Sec. 4.4, the EET dynamics resulting with opposite signs of J_{intra} are identical in the absence of exciton-bath coupling. The peculiar behavior observed with $J_{intra} > 0$ is an aftermath of frustration which reveals itself when interaction with the vibration modes allows the

excitation energy to equilibrate, a process involving redistribution of energy between degenerate ground states. Such a process enabled by vibrational modes tends to be very slow.

We now focus our attention to G=2 dendrimers with 9 segments and the same set of parameters used for the three-segment dendrimer at three different temperatures. Fig. 4.7. through Fig. 4.9 show the dynamics for these structures and several trends observed before hold here too. However, the coherence pattern here is more complex since there are a lot of segments and multiple energy scales associated with the n=9 electronic eigenstates. The dynamics here also lasts longer. The initial excitation is totally localized on segment 4 in the outer generation and rapidly spreads to segments 1 and 5. At early times, a preferential accumulation of population takes place on segment 5 as the population on segment 1 is rapidly transferred to the other two inner core segments 2 and 3. The populations of distant peripheral segments 6-9 increase gradually after a short decay.

The dynamics with $J_{\text{intra}} = -300\,\text{cm}^{-1}$ is fast here too, but the amplitude of the oscillations in the population evolution at 100 K is now smaller than in the three-segment dendrimer, in line with similar observations in large molecular aggregates.[15,47-49] With lower reorganization energy $\lambda = 300\,\text{cm}^{-1}$, these low amplitude oscillations survive till much longer (up to 500fs) in this larger dendrimer. For the higher reorganization energy, these oscillations die out faster (~200fs). In these larger dendrimers, the positive intrageneration coupling lead to even slower dynamics, though we don't see the very striking difference between the dynamical patterns for the opposite signs of the intrageneration coupling. here. With $J_{\text{intra}} = 300\,\text{cm}^{-1}$ the populations reach their equilibrium values around 1.5 ps (although, for consistency, we only show the initial 500 fs in the figure).
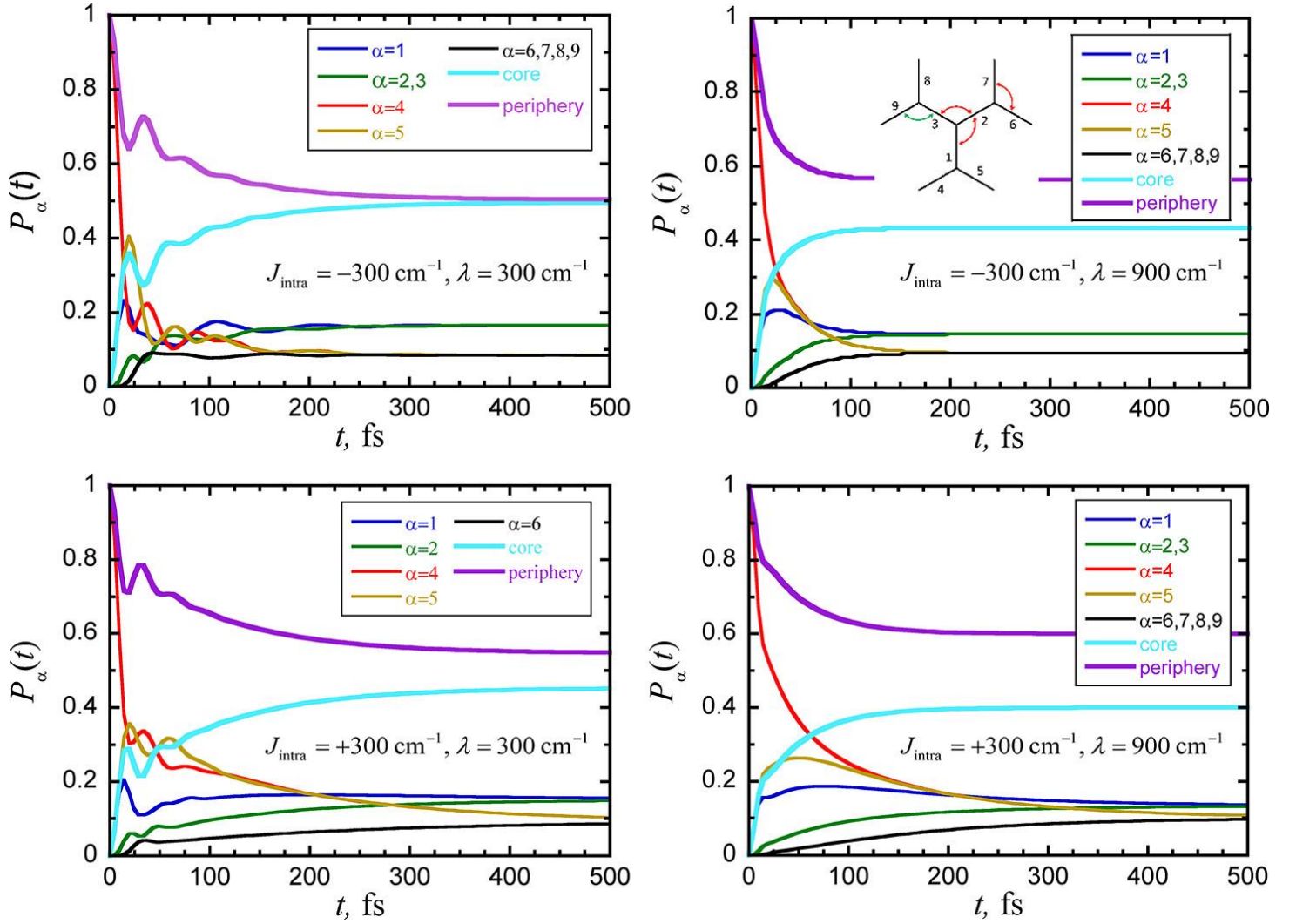
Fig. 4.8. Energy transfer dynamics in $G = 2$ dendrimers with the parameters given in the text at $T = 300$ K .

At higher temperatures, the evolution of the excitation energy is faster, and we get diminished transfer of population from the outer to the inner core. Fig. 4.9. shows the EET evolution at T=1000K. At such a high temperature, the long-time population of the inner core remains almost equal to the classical value. However, it is remarkable to note that even at this high temperature, the quantum mechanical nature of the electronic Hamiltonian is clearly visible. The eigenstate structure and specially the frustration effects with

positive intrageneration coupling is clearly evident in the considerably slower dynamics and the core population taking twice the time to reach its equilibrium as compared to negative intrageneration coupling.

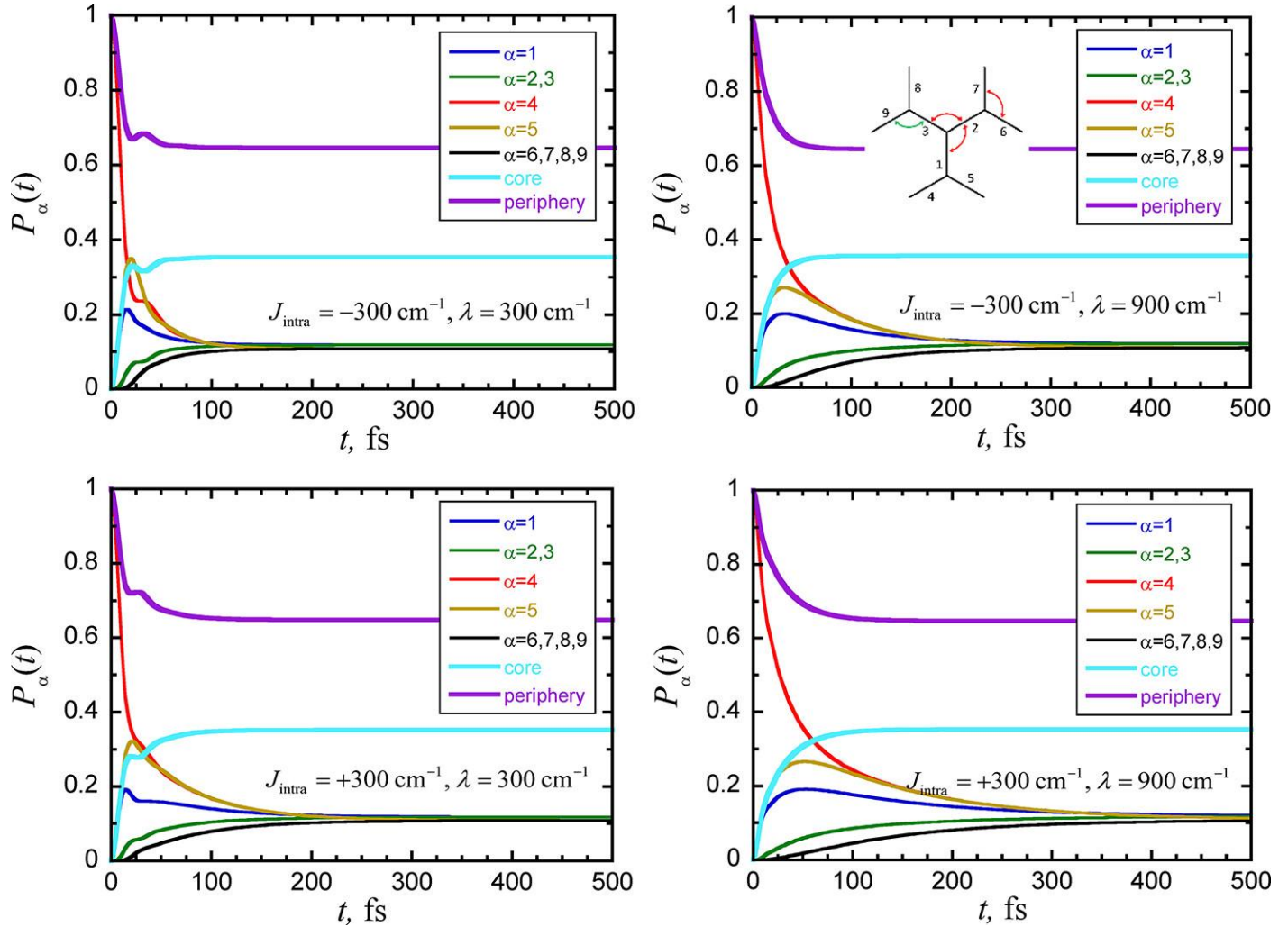**Fig. 4.9**. Energy transfer dynamics in $G = 2$ dendrimers with the parameters given in the text at $T = 1000$ K.

The role of nuclear motion on EET is also very intriguing. Intramolecular vibrations seem to not only damp the coherence, but also perturb the equilibrium segment populations. At 100K and 300K, the equilibrium populations of the core and periphery are closer to the statistical limit for the larger

reorganization energy $\lambda = 900 \, \text{cm}^{-1}$ than for the smaller value $\lambda = 300 \, \text{cm}^{-1}$. A stronger coupling between the electronic levels and the vibrational modes thus not only affect the dynamics but also but also the population distribution at thermal equilibrium.

4.7. Conclusions

In this work we have investigated the quantum mechanical structure, equilibrium properties and real-time dynamics of dendrimers described by a simple Frenkel exciton model with interaction between bias-free nearest-neighbor segments coupled to model vibrational baths. Removing the energy bias allows us to focus on the rich interplay among quantum coherence, topology, entropic factors, exciton-vibration interactions and temperature, identifying intriguing behaviors.

Even for the present single-parameter electronic Hamiltonian, several of these findings point to the remarkable physics of dendrimeric structures and the endless possibilities for targeted function through nanoscale design. Perhaps the first notable result is that even in the absence of an energetic funnel built into the electronic Hamiltonian, these structures are able to transfer excitation energy from the periphery to the core. This is a consequence of quantum effects, which give rise to eigenstate structures and equilibrium distributions that can favor the core at low temperatures. When the electronic coupling parameters are fixed, we find that small dendrimers have largest populations in the core, and that the peak of the distribution gradually shifts outward with increasing size. However, for a given dendrimer size, the core population can be increased by increasing the intra-generation coupling (or, equivalently, decreasing the inter-generation coupling strength). It is thus evident that electronic coupling can counter the periphery-favoring entropic factor, achieving outcomes that are vastly different from those based on classical statistical models.

We also find that the eigenstate structure of these dendrimers is dominated by the sign of the intra-generation coupling parameter. Analyzing a basic trimeric building block revealed that a positive value of this parameter gives rise to a destabilized structure with a doubly degenerate ground state whose wavefunction does not exhibit the threefold symmetry of the dendrimer. We attributed this behavior to electronic frustration, in analogy to the analogous effect known from spin systems. The unfavorable interaction generated by an odd number of positive couplings within a three-state unit effectively shifts electronic density toward the core, further countering the entropic effect at zero temperature. At the same time, the close proximity of multiple low-lying states leads to a sharp drop of core population upon increasing the temperature even slightly. The dynamical manifestations of electronic frustration are surprising and remarkable. We found that EET slows down very significantly when the intra-generation coupling is positive, in comparison with situations where this parameter has the same magnitude but a negative sign.

We also report real time dynamics for excitation energy transport in these dendrimers. Exciton-vibration interactions play a major role in EET and are required for equilibration and the trapping of energy. With small-to-moderate values of the vibrational reorganization energy ($\lambda \simeq J$), the population evolution is underdamped. More efficient quenching of oscillatory features is observed in dendrimers with positive intra-generation coupling. Increasing exciton-vibration coupling causes a shift of equilibrium populations away from the core, approaching a more classical behavior. The phase relations and effects related to quantized level structure are washed away by thermal effects. The population distribution becomes more classical-like with increasing temperature, with each segment having a population equal to $1/n$ in the infinite temperature limit. Interestingly, dynamical features such as those related to the sign of intra-generation couplings persist to sufficiently high temperatures, even though the equilibrium populations are close to their classical values. With typical Frenkel couplings of the order of $200-300\,\mathrm{cm}^{-1}$, the temperatures required for classical-like behavior are extremely high, thus quantum effects are expected to be prominent in dendrimers at or below physiological temperatures.

To summarize, using a simple model with a single electronic parameter of fixed magnitude ($|J| = 300\,\text{cm}^{-1}$) and two possible values of vibrational reorganization energy ($\lambda = |J|$ or $\lambda = 3|J|$), our calculations identified a vast range of time scales in the EET dynamics of $G = 2$ dendrimers at a fixed temperature, ranging from a 15fs ultrafast transfer out of the initially excited peripheral segment to a slow 1.5ps equilibration, which span two orders of magnitude. These very rich behaviors will undoubtedly become even more complex when additional parameters are allowed to vary, inviting additional work on these fascinating systems.

4.8 References

1) Pullerits, T.; Sundstrom, V., Photosynthetic light-harvesting pigment-protein complexes: Toward understanding how and why. *Acc. Chem. Res.* **1996,** *29*, 381-389.

2) Blankenship, R. E., *Molecular mechanisms of photosynthesis*. World Scientific: London, 2002.

3) van Grondelle, R.; Dekker, J. P.; Gillbro, T.; Sundstrom, V., Energy transfer and trapping in photosynthesis. *Biochim. Biophys. Acta* **1994,** *1187*, 1-65.

4) McDermott, G.; Prince, S.; Freer, A.; Hawthornthwaite-Lawless, A.; Papiz, M.; Cogdell, R.; Isaacs, N., Crystal structure of an integral membrane light-harvesting complex from photosynthetic bacteria. *Nat.* **1995,** *374*, 517.

5) Hu, X.; Xu, D.; Hamer, K.; Schulten, K.; Koepke, J.; Michel, H., Predicting the structure of the light harvesting complex II of rhodospirillum molischianum. *Prot. Sci.* **1995,** *4*, 1670-1682.

6) Koepke, J.; Hu, X.; Muenke, C.; Schulten, K.; Michel, H., The crystal structure of the light harvesting complex II (B800-B850) from Rhodospirillum molischianum. *Struc.* **1996,** *4*, 581-597.

7) Cogdell, R. J.; Isaacs, N. W.; Freer, A. A.; Arrelano, J.; Howard, T. D.; Papiz, M. Z.; Hawthornthwaite-Lawless, A. M.; Prince, S., The structure and function of the LH2 (B800–850) complex from the purple photosynthetic bacterium Rhodopseudomonas acidophila strain 10050. *Prog. Biophys. and Mol. Bio.* **1997,** *68* (1), 1-27.

8) Moore, J. S., Shape-Persistent Molecular Architectures of Nanoscale Dimension. *Acc. Chem. Res.* **1997,** *30* (10), 402-413.

9) Ballauff, M.; Likos, C. N., Dendrimers in Solution: Insight from Theory and Simulation. *Angew. Chem. Intl. Ed.* **2004,** *43* (23), 2998-3020.

10) Astruc, D.; Boisselier, E.; Ornelas, C., Dendrimers Designed for Functions: From Physical, Photophysical, and Supramolecular Properties to Applications in Sensing, Catalysis, Molecular Electronics, Photonics, and Nanomedicine. *Chem. Rev.* **2010,** *110* (4), 1857-1959.

11) Abbasi, E.; Aval, S. F.; Akbarzadeh, A.; Milani, M.; Nasrabadi, H. T.; Joo, S. W.; Hanifehpour, Y.; Nejati-Koshki, K.; Pashaei-Asl, R., Dendrimers: synthesis, applications, and properties. *Nanoscale Res. Lett.* **2014,** *9* (1), 247.

12) Schröter, M.; Ivanov, S. D.; Schulze, J.; Polyutov, S. P.; Yan, Y.; Pullerits, T.; Kühn, O., Exciton–vibrational coupling in the dynamics and spectroscopy of Frenkel excitons in molecular aggregates. *Phys. Rep.* **2015,** *567*, 1-78.

13) Hestand, N. J.; Spano, F. C., Expanded Theory of H- and J-Molecular Aggregates: The Effects of Vibronic Coupling and Intermolecular Charge Transfer. *Chem. Rev.* **2018,** *118* (15), 7069-7163.

14) Popp, W.; Brey, D.; Binder, R.; Burghardt, I., Quantum Dynamics of Exciton Transport and Dissociation in Multichromophoric Systems. *Ann. Rev. Phys. Chem.* **2021,** *72* (1), 591-616.

15) Kundu, S.; Makri, N., Intramolecular Vibrations in Excitation Energy Transfer: Insights from Real-Time Path Integral Calculations. *Ann. Rev. Phys. Chem.* **2022,** *73* (1), 349-375.

16) Harigaya, K., Coupled exciton model with off-diagonal disorder for optical excitations in extended dendrimers. *Phys. Chem. Chem. Phys.* **1999,** *1* (7), 1687-1689.

17) Mülken, O.; Blumen, A., Slow transport by continuous time quantum walks. *Phys. Rev. E* **2005,** *71* (1), 016101.

18) Mülken, O.; Bierbaum, V.; Blumen, A., Coherent exciton transport in dendrimers and continuous-time quantum walks. *J. Chem. Phys.* **2006,** *124* (12), 124905.

19) Pouthier, V., Exciton localization-delocalization transition in an extended dendrimer. *J. Chem. Phys.* **2013,** *139* (23), 234111.

20) Poliakov, E. Y.; Chernyak, V.; Tretiak, S.; Mukamel, S., Exciton-scaling and optical excitations of self-similar phenylacetylene dendrimers. *J. Chem. Phys.* **1999,** *110* (16), 8161-8175.

21) Tretiak, S.; Chernyak, V.; Mukamel, S., Localized Electronic Excitations in Phenylacetylene Dendrimers. *J. Phys. Chem. B* **1998,** *102* (18), 3310-3315.

22) Minami, T.; Tretiak, S.; Chernyak, V.; Mukamel, S., Frenkel-exciton Hamiltonian for dendrimeric nanostar. *J. Lumin.* **2000,** *87-89*, 115-118.

23) Bar-Haim, A.; Klafter, J.; Kopelman, R., Dendrimers as Controlled Artificial Energy Antennae. *J. Am. Chem. Soc.* **1997,** *119* (26), 6197-6198.

24) Bar-Haim, A.; Klafter, J., Geometric versus Energetic Competition in Light Harvesting by Dendrimers. *J. Phys. Chem. B* **1998,** *102* (10), 1662-1664.

25) Martín-Delgado, M. A.; Rodriguez-Laguna, J.; Sierra, G., Density-matrix renormalization-group study of excitons in dendrimers. *Phys. Rev. B* **2002,** *65* (15), 155116.

26) Nagy, Á., Simulating quantum systems on the Bethe lattice by translationally invariant infinite-tree tensor network. *Ann. Phys.* **2012,** *327* (2), 542-552.

27) Fernandez-Alberti, S.; Kleiman, V. D.; Tretiak, S.; Roitberg, A. E., Nonadiabatic Molecular Dynamics Simulations of the Energy Transfer between Building Blocks in a Phenylene Ethynylene Dendrimer. *J. Phys. Chem. A* **2009,** *113* (26), 7535-7542.

28) Soler, M. A.; Roitberg, A. E.; Nelson, T.; Tretiak, S.; Fernandez-Alberti, S., Analysis of State-Specific Vibrations Coupled to the Unidirectional Energy Transfer in Conjugated Dendrimers. *J. Phys. Chem. A* **2012,** *116* (40), 9802-9810.

29) Galindo, J. F.; Atas, E.; Altan, A.; Kuroda, D. G.; Fernandez-Alberti, S.; Tretiak, S.; Roitberg, A. E.; Kleiman, V. D., Dynamics of Energy Transfer in a Conjugated Dendrimer Driven by Ultrafast Localization of Excitations. *J. Am. Chem. Soc.* **2015,** *137* (36), 11637-11644.

30) Ondarse-Alvarez, D.; Oldani, N.; Roitberg, A. E.; Kleiman, V.; Tretiak, S.; Fernandez-Alberti, S., Energy transfer and spatial scrambling of an exciton in a conjugated dendrimer. *Phys. Chem. Chem. Phys.* **2018,** *20* (47), 29648-29660.

31) Beck, M. H.; Jäckle, A.; Worth, G. A.; Meyer, H.-D., The multiconfiguration time-dependent Hartree (MCTDH) method: a highly efficient algorithm for propagating wavepackets. *Phys. Rep.* **2000,** *324*, 1-105.

32) Wang, H.; Thoss, M., Multilayer formulation of the multiconfiguration time-dependent Hartree theory. *J. Chem. Phys.* **2003,** *119* (3), 1289-1299.

33) Schollwöck, U., The density-matrix renormalization group in the age of matrix product states. *Ann. Phys.* **2011,** *326*, 96-192.

34) Ambrosek, D.; Marciniak, H.; Lochbrunner, S.; Tatchen, J.; Li, X.-Q.; Würthner, F.; Kühn, O., Photophysical and quantum chemical study on a J-aggregate forming perylene bisimide monomer. *Phys. Chem. Chem. Phys.* **2011,** *13* (39), 17649-17657.

35) Popp, W.; Polkehn, M.; Hughes, K. H.; Martinazzo, R.; Burghardt, I., Vibronic coupling models for donor-acceptor aggregates using an effective-mode scheme: Application to mixed Frenkel and charge-transfer excitons in oligothiophene aggregates. *J. Chem. Phys.* **2019,** *150* (24), 244114.

36) Ren, J.; Shuai, Z.; Kin-Lic Chan, G., Time-Dependent Density Matrix Renormalization Group Algorithms for Nearly Exact Absorption and Fluorescence Spectra of Molecular Aggregates at Both Zero and Finite Temperature. *J. Chem. Theory Comput.* **2018,** *14* (10), 5027-5039.

37) Feynman, R. P., Space-time approach to non-relativistic quantum mechanics. *Rev. Mod. Phys.* **1948,** *20*, 367-387.

38) Feynman, R. P.; Hibbs, A. R., *Quantum Mechanics and Path Integrals*. McGraw-Hill: New York, 1965.

39) Feynman, R. P.; Vernon, F. L., The theory of a general quantum system interacting with a linear dissipative system. *Ann. Phys.* **1963,** *24*, 118-173.

40) Makri, N., Modular path integral: Quantum dynamics via sequential necklace linking. *J. Chem. Phys.* **2018,** *148*, 101101.

41) Makri, N., Modular path integral methodology for real-time quantum dynamics. *J. Chem. Phys.* **2018,** *149*, 214108.

42) Kundu, S.; Makri, N., Modular path integral for finite-temperature dynamics of extended systems with intramolecular vibrations. *J. Chem. Phys.* **2020,** *153*, 044124.

43) Makri, N., Small matrix disentanglement of the path integral: overcoming the exponential tensor scaling with memory length. *J. Chem. Phys.* **2020,** *152*, 041104.

44) Makri, N., Small matrix path integral for system-bath dynamics. *J. Chem. Theory Comput.* **2020,** *16*, 4038–4049.

45) Makri, N., Small matrix path integral with extended memory. *J. Chem. Theory Comput.* **2021,** *17*, 1-6.

46) Bose, A.; Makri, N., All-mode quantum-classical path integral simulation of bacteriochlorophyll dimer exciton-vibration dynamics *J. Phys. Chem.* **2020,** *124*, 5028-5038.

47) Kundu, S.; Makri, N., Real-time path integral simulation of exciton-vibration dynamics in light-harvesting bacteriochlorophyll aggregates. *J. Phys. Chem. Lett.* **2020,** *11*, 8783-8789.

48) Kundu, S.; Makri, N., Exciton-vibration dynamics in J-aggregates of a perylene bisimide from real-time path integral calculations. *J. Phys. Chem. C* **2021,** *125*, 201-210.

49) Kundu, S.; Makri, N., Origin of vibrational features in the excitation energy transfer dynamics of perylene bisimide J-aggregates. *J. Chem. Phys.* **2021,** (154), 114301.

50) Kundu, S.; Makri, N., Electronic-vibrational density evolution in a perylene bisimide dimer: mechanistic insights into excitation energy transfer. *Phys. Chem. Chem. Phys.* **2021,** *23*, 15503-15514.

51) Roy, P. P.; Kundu, S.; Valdiviezo, J.; Bullard, G.; Fletcher, J. T.; Liu, R.; Yang, S., Jr.; Zhang, P.; Beratan, D. N.; Therien, et. al., Synthetic Control of Exciton Dynamics in Bioinspired Cofacial Porphyrin Dimers. *J. Am. Chem. Soc.* **2022,** *144*, 6298–6310.

52) Dani, R.; Makri, N., Quantum quench and coherent-incoherent dynamics of Ising chains interacting with dissipative baths. *J. Chem. Phys.* **2021,** *155*, 234705.

53) May, V.; Kühn, O., *Charge and energy transfer dynamics in molecular systems*. 3rd ed.; Wiley: 2011.

54) Kundu, S.; Makri, N., Time evolution of bath properties in spin-boson dynamics. *J. Phys. Chem. B* **2021,** *125*, 8137–8151

55) Caldeira, A. O.; Leggett, A. J., Path integral approach to quantum Brownian motion. *Physica A* **1983,** *121*, 587-616.

56) Leggett, A. J.; Chakravarty, S.; Dorsey, A. T.; Fisher, M. P. A.; Garg, A.; Zwerger, M., Dynamics of the dissipative two-state system. *Rev. Mod. Phys.* **1987,** *59*, 1-85.

57) Frenkel, J., On the transfomation of light into heat in solids. *Phys. Rev.* **1931,** *37*, 17.

58) May, V.; Kuhn, O., *Theory of charge and energy transfer in molecular systems*. Wiley: 1999.

59) Makri, N., Improved Feynman propagators on a grid and non-adiabatic corrections within the path integral framework. *Chem. Phys. Lett.* **1992,** *193*, 435-444.

60) Makri, N., Numerical path integral techniques for long-time quantum dynamics of dissipative systems. *J. Math. Phys.* **1995,** *36*, 2430-2456.

61) Kundu, S.; Dani, R.; Makri, N., B800-to-B850 relaxation of excitation energy in bacterial light harvesting: All-state, all-mode path integral simulations. *J. Chem. Phys.* **2022,** *157*, 015101

Chapter 5

Quantum Rates for Multistate Processes from Coherences

5.1 Introduction

The determination of reaction rates from first principles has gathered much interest since the early days of quantum and statistical mechanics. Obtaining potential energy surfaces requires electronic structure calculations which involves difficulties needed to be circumvent. The theoretical description of finite-temperature rate also poses a challenging problem. Most efforts have focused either on barrier crossing[1] in the multidimensional potential energy surface that separates reactants from products, or on the rate of nonadiabatic transitions such as those relevant to electron transfer. Semiclassical theory has given rise to an insightful picture of tunneling, which involves classical periodic orbits on the inverted barrier potential.[2] There have been a lot of numerical and analytic methods used to characterize dependence of the reaction rate for condensed phase processes on parameters. These include the Kramers turnover[3] along with the Grote-Hynes generalization[4-5] and its quantum mechanical extension,[6-7] the Marcus inverted regime,[8-9] as well as tunneling, curve crossing and quantum interference phenomena.[10-15]

In condensed phase system, when reactive processes are sufficiently slow in comparison to time scales associated with the reactants, reaction rates are associated with exponential kinetics. If a particular state of a reactant is produced, the density first relaxes very rapidly to a local equilibrium, before there is any significant transformation to the product. Here, the flux through a surface that divides reactants from products settles rapidly to a "plateau" value, from which a slow exponential decay is observed with the same time constant that characterizes the reactive process.[16]

In this work we generalize these ideas to processes involving transformations among multiple species. The rate kinetics in this case can be described by simple kinetic equations that involve a matrix of

state-to-state transition rates. The resulting population evolution is then given by the exponential of this matrix, i.e. combinations of exponential functions characterized by rate constants. We show, most generally, that the time derivatives of populations are (at any time) simply related to the imaginary parts of off-diagonal reduced density matrix (RDM) elements (the "coherences"). The rates can then be obtained from these imaginary components, which exhibit a plateau regime. Thus, even though the populations may obey classical-like kinetic equations, the underlying dynamics is always and entirely driven by the time evolution of coherences.

5.2 System Hamiltonian

In this work, we consider the dynamics of discrete multistate Hamiltonians, which may represent a variety of processes, such as charge or energy transport, or reactive processes described by discretized continuous potentials. For systems described in terms of a continuous coordinate, we use the n lowest eigenstates of the system Hamiltonian to perform a unitary transformation to a discrete variable representation[23-24] (DVR), in which the coordinate operator is diagonal. The system operator in the DVR basis can be expressed as

$$\hat{s} = \sum_{i=1}^{n} s_i |i\rangle\langle i|$$ (5.1)

where $|i\rangle$ represent the n localized DVR states (or sites) and the DVR eigenvalues s_i serve as grid points. The Hamiltonian in the discrete form is thus given by

$$\hat{H}_0 = \sum_{i=1}^{n} \sum_{j=1}^{n} H_{ij} |i\rangle\langle j|$$ (5.2)

where $H_{ij} = H_{ji}$. Eq.5.2 can be used to describe electron transfer reactions or charge transport systems ($|i\rangle$ being electronic states in a diabatic representation), excitation energy transfer in molecular aggregates

($|i\rangle$ being excited states of monomers), coupled spin systems in addition to reactant-product processes. In general, the system interacts with a large environment (the "bath") at a particular temperature through terms that are diagonal in the site basis. We do not impose any restrictions on the form of the bath Hamiltonian or the initial density matrix.

In the numerical results presented in this work, we couple the system to separate harmonic baths (which might correspond to intramolecular normal mode coordinates of molecular aggregates[28]) characterized by the spectral density function[29]

$$J(\omega) = \tfrac{1}{2}\pi\xi\omega e^{-\omega/\omega_c} \tag{5.3}$$

which peaks at the frequency ω_c and where ξ is the dimensionless Kondo parameter that quantifies the system-bath coupling strength. In all cases the bath is initially equilibrated with respect to a common ground state, as in the case of energy transfer following a Franck-Condon initial excitation.

5.3 RDM, population rates and coherences

The RDM in the site representation is given by

$$\tilde{\rho}_{km}(t) = \mathrm{Tr}_b \langle k | e^{-i\hat{H}t/\hbar}\hat{\rho}(0)e^{i\hat{H}t/\hbar} | m \rangle \tag{5.4}$$

where $\hat{\rho}(0)$ is the initial density matrix operator and the trace is with respect to the bath modes. The diagonal elements of the RDM give the populations

$$P_k(t) \equiv \tilde{\rho}_{kk}(t) = \mathrm{Tr}\left(e^{-i\hat{H}t/\hbar}\hat{\rho}(0)e^{i\hat{H}t/\hbar}|k\rangle\langle k|\right). \tag{5.5}$$

Taking the time derivative of Eq. 5.5 we get

$$\frac{d}{dt}P_k(t) = \frac{i}{\hbar}\mathrm{Tr}\left(e^{-i\hat{H}t/\hbar}\hat{\rho}(0)e^{i\hat{H}t/\hbar}\left[\hat{H},|k\rangle\langle k|\right]\right) \tag{5.6}$$

The system-bath coupling is diagonal in the site basis, so only the system Hamiltonian contributes to the commutator. Eq. 5.5 thus becomes

$$\frac{d}{dt}P_k(t) = \frac{i}{\hbar}\sum_{j=1}^{n}\left(H_{jk}\tilde{\rho}_{kj}(t) - H_{kj}\tilde{\rho}_{jk}(t)\right) \tag{5.7}$$

Using the Hermitian property of the Hamiltonian and the RDM, we get

$$\frac{d}{dt}P_k(t) = \frac{2}{\hbar}\sum_{j=1}^{n}H_{jk}\,\mathrm{Im}\,\tilde{\rho}_{jk}(t) \,. \tag{5.8}$$

Here, the coherences and the populations are calculated from the same initial conditions.

Eq. 5.8 is completely general and exact, regardless of the form of the bath Hamiltonian, as long as the system-bath coupling is diagonal in the system basis. It generalizes the expression obtained earlier[25] for a symmetric two-level system (TLS) and shows that in the absence of imaginary components in the coherences, populations remain stationary. This is always the situation at long times, when the process has reached equilibrium and the RDM elements are given by purely real valued Boltzmann matrix elements. This is also what we observe in multistate systems which start from a real valued initial RDM. Conversely, if there is still any population evolution going on, there must be some complex valued RDM element(s). Fig. 5.1 illustrates Eq. 5.8.

The imaginary parts of the coherences in the column containing a site population may at particular instants add to zero. These situations correspond to inflection points of the site population, at which its time derivative vanishes. Also, as long as the initial RDM is real valued, at the start of the evolution, Eq. 5.8 assures that the time derivatives of all site populations are equal to zero, implying that populations evolve at least quadratically in time as $t \to 0$.
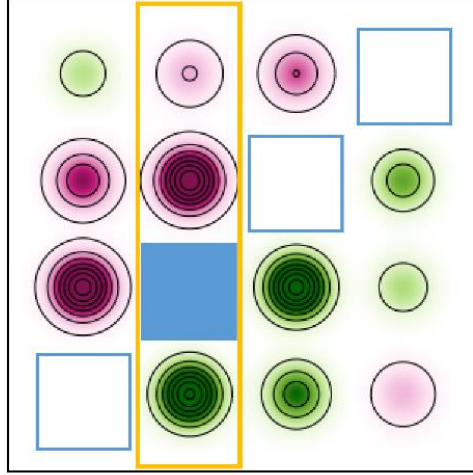
Fig.5.1. Illustration of Eq.5.8. Magenta and green areas show density contours of positive and negative imaginary parts of the RDM in the case of a 4-state system coupled to a harmonic bath. The diagonal elements (blue squares) are purely real-valued. The time derivative of the population of the second site, indicated by a filled blue square, is proportional to the sum of Hamiltonian matrix elements multiplied by imaginary components inside the column indicated with a yellow box.

5.4 Rate constants from coherences

Next, we turn our attention to obtaining rate constants from Eq. 5.8 in situations where there is an adequate separation of timescales in strongly incoherent regimes in condensed phases. Let us consider a two-state process

$$|1\rangle \underset{k_{-1}}{\overset{k_1}{\rightleftharpoons}} |2\rangle. \tag{5.9}$$

The site populations rapidly settle into forms that satisfy kinetic equations at sufficiently high temperatures and strong system-bath coupling. The population evolution rate for the two states can be described in terms of a forward and a backward rate constant through the following differential equations

$$\dot{P}_1(t) = -k_1 P_1(t) + k_{-1} P_2(t)$$
$$\dot{P}_2(t) = k_1 P_1(t) - k_{-1} P_2(t) \tag{5.10}$$

whose solution gives the following population evolution

71

$$P_1(t) - P_1(\infty) = \left[P_1(0) - P_1(\infty)\right]e^{-(k_1+k_{-1})t}$$
$$P_2(t) - P_2(\infty) = \left[P_2(0) - P_2(\infty)\right]e^{-(k_1+k_{-1})t}$$

(5.11)

Here, the knowledge of the forward and the backward rate constants is enough to fully characterize the dynamics and even the equilibrium constant $K = P_2(\infty)/P_1(\infty) = k_1/k_{-1}$ or the ratio of the populations of the two species at equilibrium.

As mentioned earlier, exponential population dynamics requires a separation of time scales, implying that the time required for the system populations to reach equilibrium is much longer than the time of local equilibration with the environment, allowing the populations to enter a regime of exponential decay early on. This is long before any appreciable deviations from the initial values have occurred and Eq. 5.11 is valid except for a very short time of nonexponential transients.[16] This realization has led to the development of classical and quantum mechanical flux correlation function formulations,[20-22] which deduce the rate from the behavior of the flux in the "plateau" regime. The standard formulation is based on the equilibrium flux correlation function, but recent work has shown[27] that the flux obtained with non-equilibrium initial conditions contains precisely the same information and may be used to obtain the rate without the need for numerical evaluation of the full equilibrium density. If we start with $P_1(0) = 1$, Eq. 5.11 gives us

$$\dot{P}_1(t) = -\left(k_1 + k_{-1}\right)\left[1 - P_1(\infty)\right]e^{-(k_1+k_{-1})t} = -k_1 e^{-(k_1+k_{-1})t}, \quad t > t_{\mathrm{p}}. \tag{5.12}$$

Here, $\dot{P}_1$ is the non-equilibrium flux, which (for a real-valued initial RDM) vanishes at the start of the evolution. This function can be obtained from the imaginary part of the off-diagonal RDM elements (ot the coherences) using Eq. 5.8. Since $\exp(-k_1 t_{\mathrm{p}} - k_{-1}t_{\mathrm{p}}) \simeq 1$, the non-equilibrium flux quickly grows from zero to the value given by the right-hand side of Eq. 5.11 at the onset t_{p} of the plateau regime, after which it decays exponentially over a time that is very long compared to t_{p} (plateau time). Assuming, as usual, that the exponential factor is very close to unity at this time, we recover the result[25]

$$k_1 = \frac{2}{\hbar} H_{12} \operatorname{Im} \tilde{\rho}_{12}(t_{\mathrm{p}}) \tag{5.13}$$

The next section expands these ideas to a more generic n state system.

5.5 Kinetic equations and rate constants for a generic n state system

We now turn to processes involving multiple states. Let us consider a system of n states interacting through the Hamiltonian mentioned in Eq. 5.2 whose populations satisfy the following rate equations

$$\frac{d}{dt} \mathbf{P}(t) = \mathbf{M} \cdot \mathbf{P}(t) \tag{5.14}$$

where $\mathbf{P}(t)$ is the vector that contains the populations P_k of the states at time t and $\mathbf{M}$ is a matrix of transition rates. Using Eq. 5.8, we obtain

$$\dot{P}_k(t) = \sum_{j=1}^n M_{kj} P_j(t) = \frac{2}{\hbar} \sum_{j=1}^n H_{jk} \operatorname{Im} \tilde{\rho}_{jk}(t) \tag{5.15}$$

This equation holds for any initial condition of the RDM. We now evaluate Eq. 5.15 with *all* initial conditions, $\hat{\rho}(0) = |i\rangle\langle i|$, at the plateau time. We indicate the initial condition in the RDM elements through a superscript, $\tilde{\rho}_{jk}^{ii}$. Using again $P_i \simeq 1, P_{j \neq i} \simeq 0$ at the early plateau time, we obtain

$$\frac{d}{dt} \tilde{\rho}_{kk}^{ii}(t_{\mathrm{p}}) = M_{ki} \tag{5.16}$$

leading to the result

$$M_{ki} = \frac{2}{\hbar} \sum_{j=1}^n H_{jk} \operatorname{Im} \tilde{\rho}_{jk}^{ii}(t_{\mathrm{p}}) \tag{5.17}$$

Eq. 5.17 gives the state-to-state rates in terms of the (imaginary parts of) coherences at the plateau time.

It should be noted here that while the matrix $\mathbf{M}$ has n^2 elements, there are only $n(n-1)$ forward and reverse rate constants. Thus, this means there is a linear dependence in the matrix i.e. $\det(\mathbf{M}) = 0$.

Differentiating the sum of populations, one can express a diagonal element M_{kk} in terms of all other elements M_{jk}, allowing the kinetic equations to be written in a form that does not involve diagonal elements,

$$\dot{P}_k(t) = \sum_{j \neq k}^{n} M_{kj} P_j(t) - \left(\sum_{j \neq k}^{n} M_{jk} \right) P_k(t) \tag{5.18}$$

implying that only $n^2 - n$ elements of the matrix are required to fully characterize the kinetics. With $j \neq k$ the elements of $\mathbf{M}$ are the forward and reverse rate constants between sites.

Further, we note that in cases of imperfect separation of timescales, the populations may have deviated significantly from their initial values during the short time of transient evolution that precedes the plateau regime. The kinetic equations are valid for $t > t_p$ and should be integrated with adjusted initial conditions given by the actual value of population of the states at the plateau time, $P_k(t_p)$. The population values obtained from the full propagation of the RDM should be used for $t < t_p$.

Lastly, from the detailed balance principle we get

$$M_{ki} P_i(\infty) = M_{ik} P_k(\infty) \tag{5.19}$$

which means that *the imaginary parts of the coherences at the plateau time fully specify the equilibrium populations* through the relation

$$\sum_{j=1}^{n} H_{jk} \operatorname{Im} \tilde{\rho}_{jk}^{ii}(t_p) P_i(\infty) = \sum_{j=1}^{n} H_{ji} \operatorname{Im} \tilde{\rho}_{ji}^{kk}(t_p) P_k(\infty) \tag{5.20}$$

This is a subtle and rather remarkable property.

5.6 Detailed derivation of kinetic equations and rate constants for a three-state system

Let us consider the following three-state system where all states are coupled in the system, describing a physical situation where the transformation from $|1\rangle$ to $|3\rangle$ can occur through two pathways, i.e. through

direct population transfer as well as through an intermediate state $|2\rangle$. The rate constants are labelled symmetrically,

$$
\begin{array}{c}
|2\rangle \\
k_1 \diagup\diagup k_{-1} \quad k_{-2} \diagdown\diagdown k_2 \\
|1\rangle \overset{k_{-3}}{\underset{k_3}{\rightleftharpoons}} \quad |3\rangle
\end{array}
\tag{5.21}
$$

The kinetic equations for such a system are given by

$$
\begin{aligned}
\dot{P_1}(t) &= -k_1 P_1(t) + k_{-1} P_2(t) + k_3 P_3(t) - k_{-3} P_1(t) \\
\dot{P_2}(t) &= k_1 P_1(t) - k_{-1} P_2(t) - k_2 P_2(t) + k_{-2} P_3(t) \\
\dot{P_3}(t) &= k_2 P_2(t) - k_{-2} P_3(t) - k_3 P_3(t) + k_{-3} P_1(t)
\end{aligned}
\tag{5.22}
$$

These rate equations can be casted in the matrix form of Eq. 5.14 with $M_{12} = k_{-1}, M_{13} = k_3$, $M_{21} = k_1, M_{23} = k_{-2}, M_{31} = k_{-3}, M_{32} = k_2$. Evaluating $\dot{P_k}$ from the above equations for all initial conditions $\hat{\rho}(0) = |i\rangle\langle i|, i \neq k$, we get

$$
\begin{aligned}
k_1 &= \frac{2}{\hbar} H_{12} \operatorname{Im} \tilde{\rho}_{12}^{11}(t_\mathrm{p}) + \frac{2}{\hbar} H_{32} \operatorname{Im} \tilde{\rho}_{32}^{11}(t_\mathrm{p}), \quad k_{-1} = \frac{2}{\hbar} H_{21} \operatorname{Im} \tilde{\rho}_{21}^{22}(t_\mathrm{p}) + \frac{2}{\hbar} H_{31} \operatorname{Im} \tilde{\rho}_{31}^{22}(t_\mathrm{p}) \\
k_2 &= \frac{2}{\hbar} H_{23} \operatorname{Im} \tilde{\rho}_{23}^{22}(t_\mathrm{p}) + \frac{2}{\hbar} H_{13} \operatorname{Im} \tilde{\rho}_{13}^{22}(t_\mathrm{p}), \quad k_{-2} = \frac{2}{\hbar} H_{12} \operatorname{Im} \tilde{\rho}_{12}^{33}(t_\mathrm{p}) + \frac{2}{\hbar} H_{32} \operatorname{Im} \tilde{\rho}_{32}^{33}(t_\mathrm{p}) \\
k_3 &= \frac{2}{\hbar} H_{21} \operatorname{Im} \tilde{\rho}_{21}^{33}(t_\mathrm{p}) + \frac{2}{\hbar} H_{31} \operatorname{Im} \tilde{\rho}_{31}^{33}(t_\mathrm{p}), \quad k_{-3} = \frac{2}{\hbar} H_{23} \operatorname{Im} \tilde{\rho}_{23}^{11}(t_\mathrm{p}) + \frac{2}{\hbar} H_{13} \operatorname{Im} \tilde{\rho}_{13}^{11}(t_\mathrm{p})
\end{aligned}
\tag{5.23}
$$

The expressions in Eq. 5.23 agree with the general form given by Eq. 5.17. The diagonal components in Eq. 5.22 are $M_{11} = -k_1 - k_{-3}$, $M_{22} = -k_{-1} - k_2$ and $M_{33} = -k_{-2} - k_3$, i.e. are given in terms of sums of off-diagonal elements of the rate matrix, thus are not independent, in agreement with the remark made earlier. If all coupling elements have the same value, the three-site system is completely symmetric, and all rate constants are identical. In this case the eigenvector corresponding to the vanishing eigenvalue of **M**, which describes the equilibrium populations, has equal components on the three sites. Symmetry breaking (through nondegenerate site energies or unequal coupling matrix elements) leads to unequal site

75

populations. A non-cyclic tight binding Hamiltonian with identical nearest neighbor couplings has different

forward and reverse rates, which become equal only at infinite temperature, thus in general the equilibrium

populations of each site depend on the location of the site. To illustrate these ideas, we present a few

numerical results of a few model system in the next section.

5.7 Numerical results and methods

In this section, we present numerical results on several models of discrete systems coupled to separate

harmonic baths (which might correspond to intramolecular normal mode coordinates of molecular

aggregates[28]). We describe the models in terms of a characteristic coupling value $\hbar\Omega$ between system sites.

For the bath, we go to the spectral density function of a bath given in Eq. 5.3. and to generate a proper

separation of timescales, set $\omega_{\mathrm{c}} = 100\,\Omega$. We use two values of the Kondo parameter, $\xi = 0.1$ and 0.5,

which correspond to reorganization energies equal to $20\,\hbar\Omega$ and $100\,\hbar\Omega$, respectively. Putting these values

in context of chemical reactions, it is useful to consider the value $2\hbar\Omega \simeq 10\ \mathrm{cm}^{-1}$ as a tunneling splitting

value typical of many proton transfer or isomerization processes. With this value of Ω, the characteristic

bath frequency corresponds to $500\ \mathrm{cm}^{-1}$ and the reorganization energy is $100\,\mathrm{cm}^{-1}$ with $\xi = 0.1$ and 500

cm^{-1} if $\xi = 0.5$. In the calculations shown in this section, we obtain an adequate plateau at or above the

intermediate temperature $\hbar\omega_{\mathrm{c}}\beta = 2$, which is slightly higher than room temperature. We note that the

temperature is very high with respect to the characteristic frequency of the system, i.e. $\hbar\Omega\beta = 0.02$. As a

result, all equilibrium site populations attain equal values of $1/n$.

We also consider a slower bath with $\omega_{\mathrm{c}} = 10\,\Omega$. This relatively low-frequency bath does not produce

a good separation of time scales and the flux does not exhibit a flat plateau. For the same system energy

scale $2\hbar\Omega \simeq 10\ \mathrm{cm}^{-1}$, the characteristic frequency of the bath is now only $50\ \mathrm{cm}^{-1}$, typical of solvent

modes. Nevertheless, we show that at the same temperature (for which now $\hbar\omega_{\mathrm{c}}\beta = 0.2$), the population

evolution is still quantitatively described by kinetic equations and the rates obtained from the sloped flux

function are highly accurate. On the other hand, if the system energy scale is characteristic of Frenkel exciton[30] couplings, $\hbar\Omega \simeq 50$ cm^{-1}, a bath frequency $\omega_c = 10\,\Omega$ corresponds to 500 cm^{-1}. Realistic temperatures in this case correspond to $\hbar\omega_c\beta = 2$ or higher. As the temperature is decreased, time scales become truly mixed, eventually causing a breakdown of the kinetic equations.

The real time dynamics of the system was performed using the small matrix decomposition of the path integral[31-33] (SMatPI) which has been discussed in Chapter 2. The coupled kinetic equations were solved using the numerical differential equation solver of Mathematica.[41]

The figures in this section show the time evolution of the site populations that develop from the initial condition $\tilde{\rho}(0) = |1\rangle\langle 1|$, as well as their time derivatives, as obtained from the SMatPI calculations and also from solving the kinetic equations with the rates obtained from the imaginary parts of the coherences, for several multistate model systems. In all cases it is seen that the time derivatives obtained from Eq. 5.8 always agree exactly with those obtained through numerical differentiation of the SMatPI population results. Also, the solution of the kinetic equations with rates obtained from the imaginary parts of the coherences are in excellent agreement with the SMatPI results.

Fig. 5.2 gives the results for a three-state system with identical site energies and nearest-neighbor couplings, described by the Hamiltonian

$$\hat{H}_0 = -\hbar\Omega\left(|1\rangle\langle 2| + |2\rangle\langle 1| + |2\rangle\langle 3| + |3\rangle\langle 2|\right) \tag{5.24}$$

which describes a sequential process. The bath is at the intermediate temperature $\hbar\omega_c\beta = 2$. We consider two values of the bath frequency, $\omega_c = 100\,\Omega$ and $10\,\Omega$, along with two values of the Kondo parameter. In all cases the populations of the first two sites start changing immediately, while the third site follows later, with a zero derivative at the initial time. On the time scale that corresponds to completion of the process, the populations, as well as the imaginary parts of the coherences (as time derivatives of populations), exhibit (multi-)exponential evolution. However, the imaginary components of the coherences are seen to rise very steeply at first and then settle into a slow evolution and eventually decay.
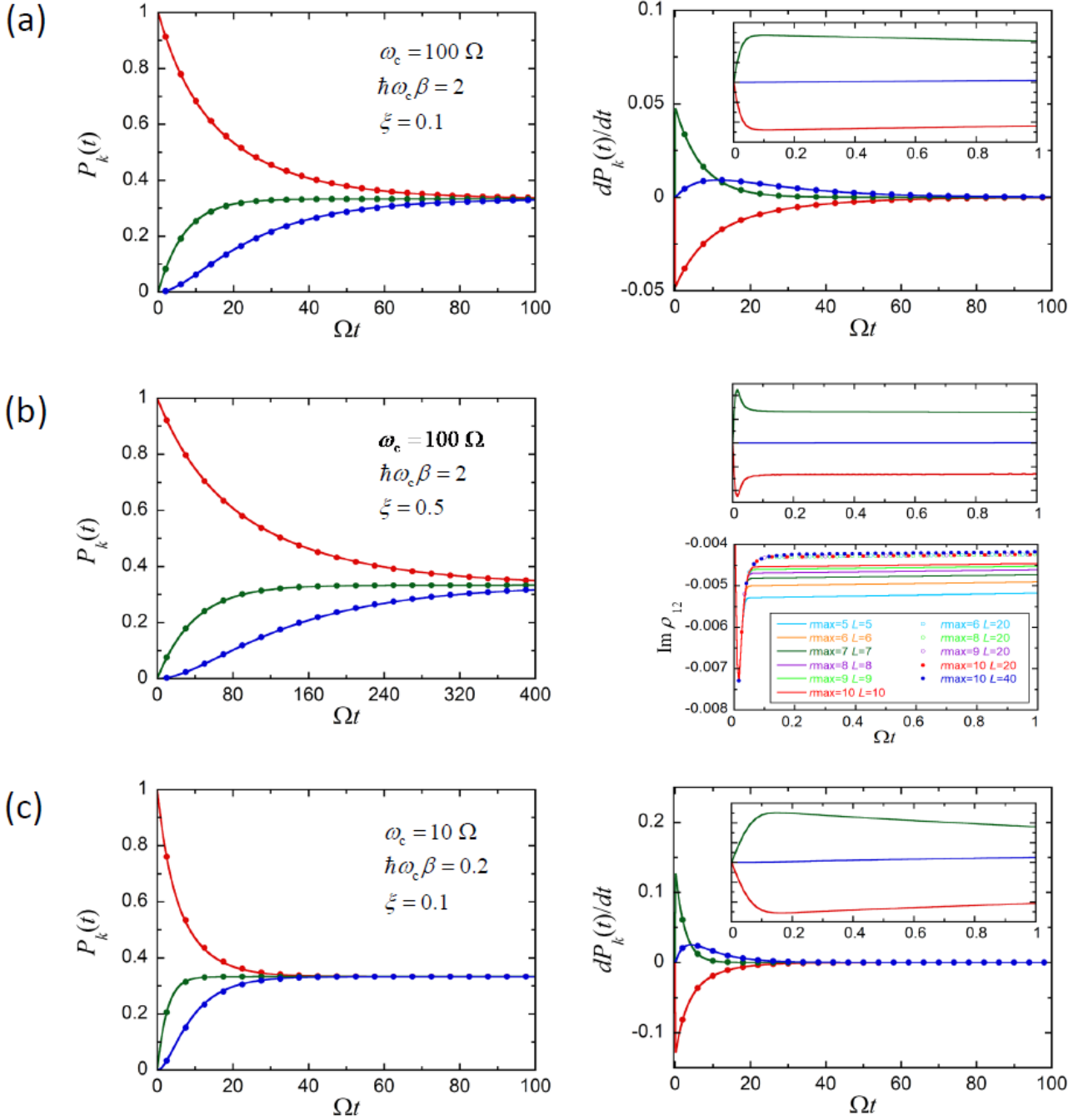
Fig.5 2. Site populations and their derivatives for the three-state model with the Hamiltonian given by Eq.5.24. Solid lines show SMatPI results for the site populations and their numerical derivatives computed by finite difference. In the right panels, markers show the population derivatives obtained from the imaginary parts of the coherences, while in the left panels, markers show populations obtained from the solution of the kinetic equations with rates computed from the coherences at the plateau time. The insets show enlargements of the early dynamics. In (b) the right panel shows the convergence of the imaginary component of a coherence as a function of the SMatPI entanglement parameter r_{max} and the memory length L. Red, green and blue correspond to sites 1, 2 and 3, respectively. (a) $\omega_c = 100\Omega$, $\xi = 0.1$, $\hbar\omega_c\beta = 2$. (b) $\omega_c = 100\Omega$, $\xi = 0.5$, $\hbar\omega_c\beta = 2$. (c) $\omega_c = 10\Omega$, $\xi = 0.1$, $\hbar\omega_c\beta = 0.2$.

At early times $\Omega t_p \simeq 0.1 - 0.2$, upon magnification of the plot, we see a near plateau i.e. a linear region with a very small slope. We note that an even larger value of ω_c would result in a more pronounced separation of timescales and a truly flat (on the time scale of these graphs) plateau region in the population derivatives. The dynamics is faster with smaller values of the reorganization energy ($\xi = 0.1$ and $\omega_c = 10\,\Omega$), causing a more conspicuous slope of the time derivatives. Even when there isn't a perfect plateau, the population dynamics reproduced by the rates obtained from the imaginary parts of the coherences match the path integral results perfectly. With the smaller value of system-bath coupling ($\xi = 0.1$), the evolution of population derivatives is nearly monotonic up to the plateau value. In contrast, the population derivatives undergo strongly nonmonotonic evolution prior to reaching the plateau when the reorganization energy is large ($\xi = 0.5$). The slower population dynamics observed in this case leads to a flatter plateau regime. In all cases shown in Fig. 5.2, the RDM needs to be propagated for a relatively short time. This time should be longer than t_p ($\Omega t \sim 1$ in the present example) to verify the existence of a rate plateau.

Next, in Fig. 5.3 we show results for a different three-state process, where state 1 is transformed to 3 through the direct pathway and also through an intermediate (state 2) according to the Hamiltonian

$$\hat{H}_0 = -\tfrac{1}{2}\hbar\Omega\big(|1\rangle\langle 2| + |2\rangle\langle 1|\big) - \hbar\Omega\big(|2\rangle\langle 3| + |3\rangle\langle 2|\big) - \tfrac{3}{2}\hbar\Omega\big(|1\rangle\langle 3| + |3\rangle\langle 1|\big) \tag{5.25}$$

In this case, population is transferred to states 2 and 3 simultaneously but with different rates, as expected based on the different coupling strengths in the Hamiltonian. The temperature and the bath parameters for Fig. 5.3.a are the same as that in Fig 5.2.a, however the dynamics for the former is much faster due to the larger values of one of the couplings and the existence of two pathways. The separation of timescales in this case is weaker and we get a somewhat large slope of the flux in the plateau region. Nevertheless, the computed rates again give rise to highly accurate populations, which are practically identical to those from the SMatPI results.
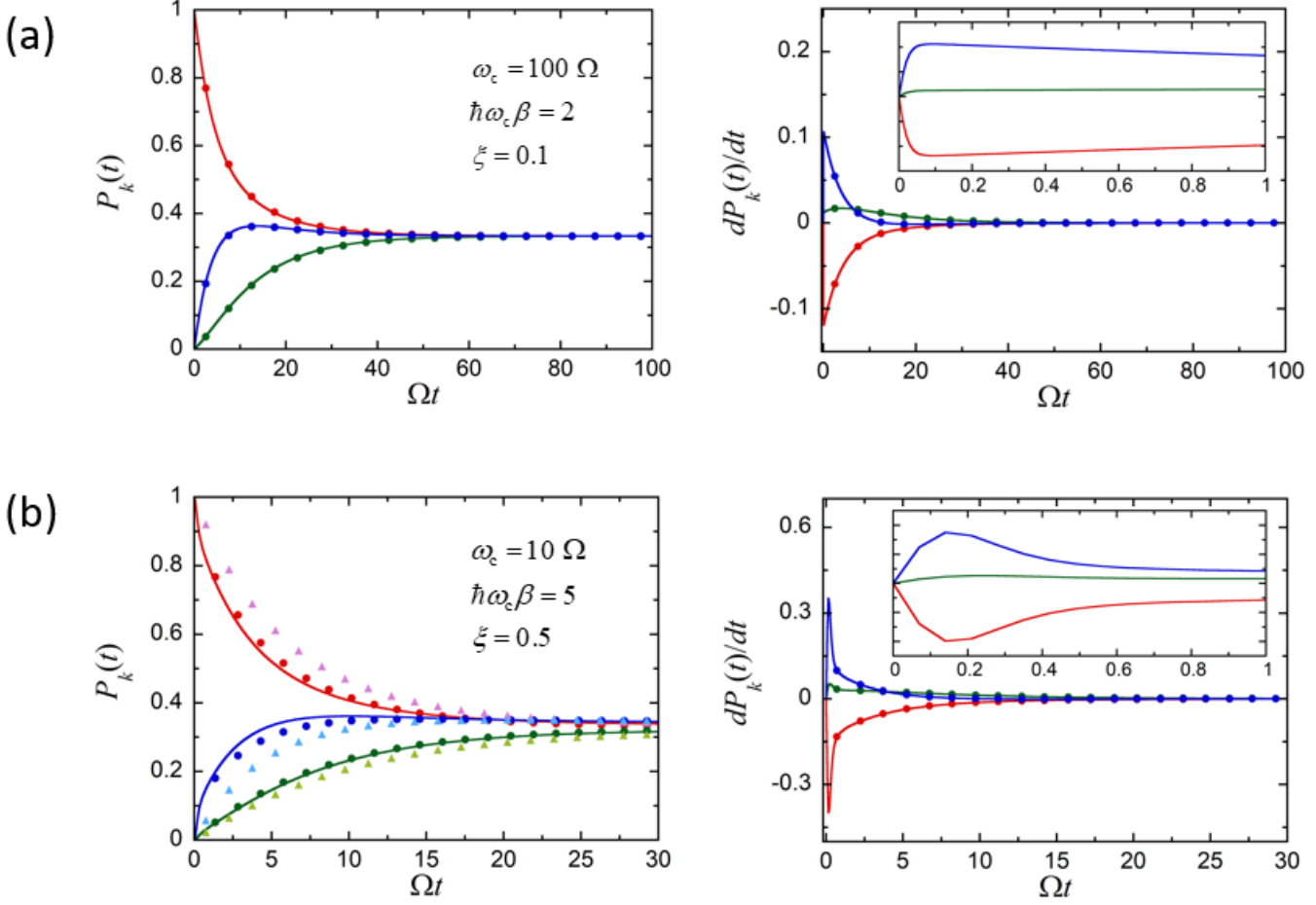
Fig. 5.3. Site populations and their derivatives for the three-state model with the Hamiltonian given by Eq.5.25. Solid lines show SMatPI results for the site populations and their numerical derivatives computed by finite difference. In the right panels, markers show the population derivatives obtained from the imaginary parts of the coherences, while in the left panels, they show populations obtained from the solution of the kinetic equations with rates computed from the coherences at the plateau time. In (b), triangles show results obtained by integrating the kinetic equation from $t = 0$, while circles show solutions obtained after the t_p, while early time populations are obtained from SMatPI results. The insets show enlargements of the early dynamics. Red, green and blue correspond to sites 1, 2 and 3, respectively. (a) $\omega_c = 100\Omega$, $\xi = 0.1$, $\hbar\omega_c\beta = 2$. (b) $\omega_c = 10\Omega$, $\xi = 0.1$, $\hbar\omega_c\beta = 5$.

For a two-state system with weak coupling to a harmonic bath, a decrease of temperature leads to larger rate.[10,14] We see this trend in the three-site dynamics as well. As the temperature is lowered, early-time transients survive much longer and merging time scales lead to deviations from uniform exponential behavior, affecting the accuracy of kinetic equation models. Fig. 5.3.b shows results for a three state system at $\hbar\omega_c\beta = 5$, which is lower than any of the temperatures we have used in this work, although it is still

relatively high with respect to the system energy scale ($\hbar\Omega\beta = 0.5$). Even though the time for the completion of this process is comparable to that in Fig. 5.2.c, the flux rises much more slower and settles into a not very well-defined plateau much later at $\Omega t_{\text{p}} \simeq 0.6$. Here, the populations obtained from the kinetic equations with rates extracted from the coherence don't reproduce the correct dynamics. However, initializing the kinetic equations with the population values from the path integral results at t_{p} leads to improved results which are almost quantitative (Fig. 5.3.b). Further decreasing the temperature leads to oscillatory dynamics through inadequate damping of quantum coherence, where the kinetic equations are invalid.
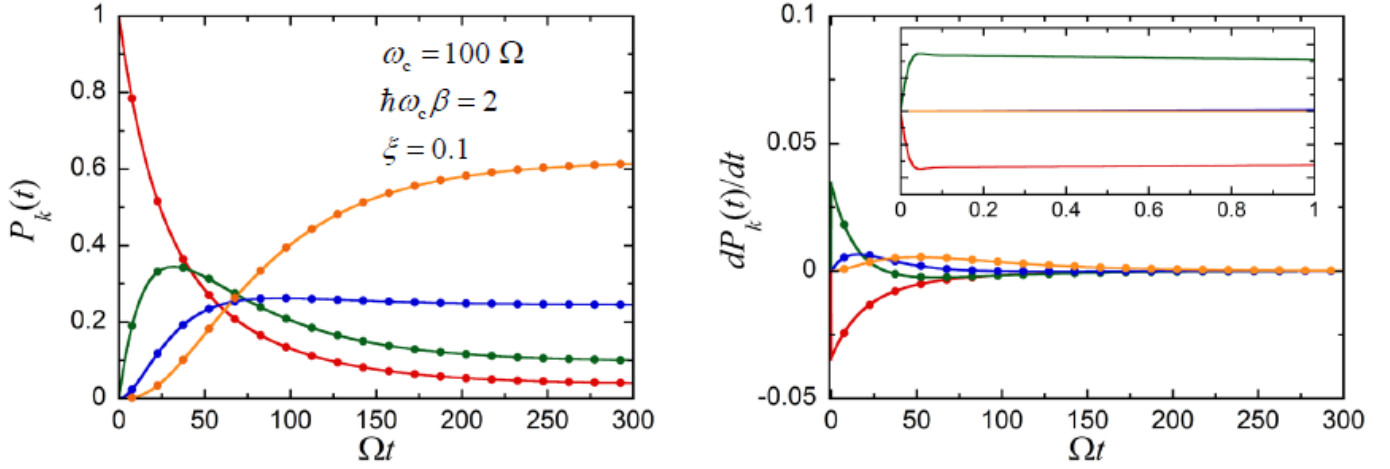

Fig.5.4. Same as Fig. 3, but for the four-state system given in Eq.5.26. The parameters are $\omega_{\text{c}} = 100\Omega$, $\xi = 0.1$, $\hbar\omega_{\text{c}}\beta = 2$. Red, green, blue and orange correspond to sites 1, 2, 3 and 4, respectively.

Next, we present results for a four-state downhill process i.e. where the Hamiltonian has nearest-neighbor couplings, but the site energies decrease gradually according to the Hamiltonian

$$\hat{H}_0 = -\hbar\Omega\sum_{i=1}^{3}\left(|i\rangle\langle i+1| + |i+1\rangle\langle i|\right) - 50\hbar\Omega|2\rangle\langle 2| - 100\hbar\Omega|3\rangle\langle 3| - 150\hbar\Omega|4\rangle\langle 4| \qquad (5.26)$$

Fig. 5.4 shows the results for such a process. The site populations rise sequentially here, and we can see states 3 and 4 have a zero slope at early times as they are not directly connected to state 1. The population of state 2 shows a pronounced peak while that of state 4 rises monotonically. Also, the equilibrium populations decrease monotonically from 1 to 4 because the temperature is moderate to low with respect to differences in site energies, $\hbar(150\Omega)\beta = 3$.
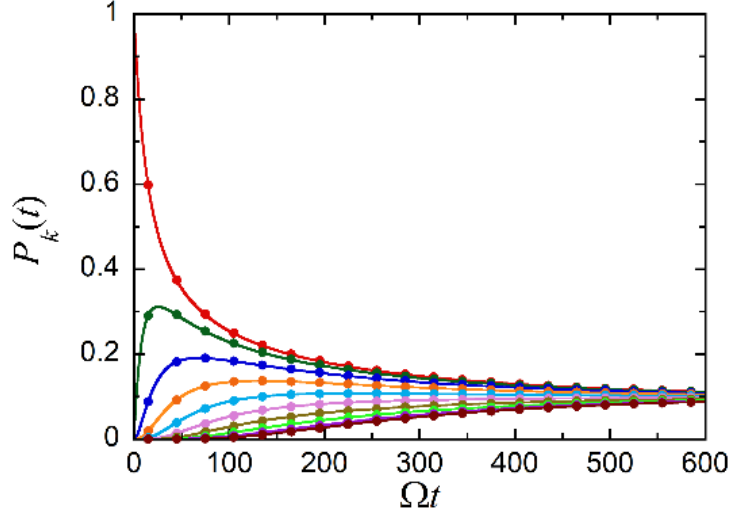

Fig. 5.5.   Site populations for the ten-state model with the Hamiltonian given by Eq.5.27. with $\omega_c = 100\Omega$, $\xi = 0.1$, $\hbar\omega_c\beta = 2$. Solid lines show SMatPI results for the site populations, while markers show populations obtained from the solution of the kinetic equations with rates computed from the coherences at the plateau time. The populations of sites 2-10 rise in sequence.

Last, we present results for a 10-site system with nearest-neighbor couplings described by

$$\hat{H}_0 = -\hbar\Omega\sum_{i=1}^{9}\left(|i\rangle\langle i+1| + |i+1\rangle\langle i|\right) \qquad (5.27)$$

where $\hbar\omega_c\beta = 2$, $\omega_c = 100\,\Omega$ and $\xi = 0.1$. Fig. 5.5. shows the site populations, which rise in sequence. Again, the rates computed from the imaginary parts of the coherences lead to excellent agreement between kinetic equations and path integral results.

5.8 Conclusion

It is interesting to note that the simple master equation describes Markovian dynamics. However, that doesn't mean that we should calculate the rate constants from Markovian algorithms as at early times, prior to the onset of the plateau time, the dynamics is highly non-Markovian. Thus, these rate constants need to be calculated using powerful quantum dynamical results.

The validity of a set of simple kinetic equations with available rate parameters is important conceptually and, in the case of processes in complex, anharmonic environments, quite useful from a practical perspective. For very slow (>ns time scale) processes, knowledge of the rate matrix usually is sufficient. Obtaining the full-time evolution of site populations can be useful in multistate processes, in particular when competing pathways are available. Also, the cost of long-time propagation generally is much higher when the system is coupled to a complex anharmonic environment. The kinetic equations are much more efficient for these multistate ($n > 10$) and/or slow processes. In this case, calculating the relatively short-time dynamics of the RDM that encodes the rate information via a reliable method and obtaining long-time populations by solving the coupled kinetic equations would be the most efficient approach, as long as the kinetic equation description is applicable.

When the interaction between a system and its environment is local in the system basis, imaginary components of coherences are directly related to time derivatives of populations. Each such time derivative can be thought of as a state-to-state flux, which (under conditions associated with rate dynamics) settles early on to a slow exponential decay with the usual plateau appearance familiar from reaction rate theory. The imaginary component of the multistate RDM (with all possible initial conditions) at the relatively short

plateau time determines the state-to-state rate matrix, which may be used to obtain the population dynamics by solving a system of simple kinetic equations. We found the procedure to be robust and accurate even when the plateau is visibly sloped and the onset of the plateau regime occurs later, as long as the kinetic equations are used only for the remainder of the time evolution. Even when systems exhibit rate kinetics associated with classical hopping models, our analysis reveals that quantum coherences are present during the entire course of time evolution. Coherences are associated with quantum superpositions, which survive the massive damping that gives rise to exponential evolution. More severe damping of superpositions leads to slower dynamics. When thermal fluctuations and noisy environments drastically quench coherent superpositions of states, quantum transitions become very slow, leading to small rates. Thus, phenomenological kinetic equations emerge when noise extensively dampens quantum superpositions, creating slow processes and a separation of time scales that lead to exponential evolution, and not because of the absence of quantum effects. Also, since state-to-state rates determine equilibrium populations by virtue of the detailed balance property, we concluded that (for processes that exhibit rate kinetics) the early time evolution of coherences also encodes all information necessary for obtaining the populations at equilibrium. This striking observation applies to general multistate systems in contact with complex environments.

5.9 References

1) Fleming, G. R.; Hänggi, P., *Activated barrier crossing*. World Scientific: Singapore, 1993.
2) Miller, W. H., Semiclassical Limit of Quantum Mechanical Transition State Theory for Non-Separable Systems. *J. Chem. Phys.* **1975,** *62*, 1899-1906.
3) Kramers, H. A., Brownian motion an a field of force and the diffusion model of chemical reactions. *Physica (Utrecht)* **1940,** *7*, 284-304.
4) Grote, R. F.; Hynes, J. T., The stable states picture of chemical reactions. II. Rate constants for condensed and gas phase reaction models. *J. Chem. Phys.* **1980,** *73*, 2715.

5) Pollak, E., Theory of activated rate processes: A new derivation of Kramers' expression. *J. Chem. Phys.* **1986,** *85*, 865.

6) Wolynes, P. G., Quantum theory of activated events in condensed phases. *Phys. Rev. Lett.* **1981,** *47*, 968.

7) Pollak, E.; Grabert, H.; Hänggi, P., Theory of activated rate processes for arbitrary frequency dependent friction: Solution of the turnover problem. *J. Chem. Phys.* **1989,** *91* (7), 4073-4087.

8) Marcus, R. A., Electrostatic free energy and other properties of states having nonequilibrium polarization. I*. *J. Chem. Phys.* **1956,** *24*, 979-989.

9) Marcus, R. A.; Sutin, N.; Electron transfers in chemistry and biology. *Biochim. Biophys. Acta* **1985,** *811*, 265-322.

10) Leggett, A. J.; Chakravarty, S.; Dorsey, A. T.; Fisher, M. P. A.; Garg, A.; Zwerger, M., Dynamics of the dissipative two-state system. *Rev. Mod. Phys.* **1987,** *59*, 1-85.

11) Frauenfelder, H.; Wolynes, P. G., Rate theories and puzzles of heme protein kinetics. *Sci.* **1985,** *228*, 337.

12) Onuchic, J. N.; Wolynes, P. G., Classical and quantum pictures of reaction dynamics in condensed matter: Resonances, dephasing, and all that. *J. Phys. Chem.* **1988,** *92*, 6495-6503.

13) Hänggi, P.; Talkner, P.; Borcovec, M., Reaction rate theory: Fifty years after Kramers. *Rev. Mod. Phys.* **1990,** *62*, 251-341.

14) Topaler, M.; Makri, N., Quantum rates for a double well coupled to a dissipative bath: accurate path integral results and comparisons with approximate theories. *J. Chem. Phys.* **1994,** *101*, 7500-7519.

15) Topaler, M.; Makri, N., Path integral calculation of quantum nonadiabatic rates in model condensed phase reactions. *J. Phys. Chem.* **1996,** *100*, 4430-36.

16) Chandler, D., *Introduction to Modern Statistical Mechanics*. Oxford University Press: New York, 1987.

17) Keck, J. C., Variational theory of shemical reaction rates applied to three-body recombinations. *J. Chem. Phys.* **1960,** *32*, 1035.

18) Kapral, R., Internal relaxation in chemically reacting fluids. *J. Chem. Phys.* **1972,** *56*, 1842.

19) Chandler, D., Statistical mechanics of isomerization dynamics in liquids and the transition state approximation. *J. Chem. Phys.* **1978,** *68*, 2959-2970.

20) Berne, B. J., Methods in rate theory. In *Activated barrier crossing: Application in physics, chemistry and biology*, Fleming, G. R.; Hänggi, P., Eds. World Scientific Publishing Co. Pt. Ltd.: Singapore, 1993; pp 82-119.

21) Yamamoto, T., Quantum statistical mechanical theory of the rate of exchange chemical reactions in the gas phase. *J. Chem. Phys.* **1960,** *33*, 281-289.

22) Miller, W. H.; Schwartz, S. D.; Tromp, J. W., Quantum mechanical rate constants for bimolecular reactions. *J. Chem. Phys.* **1983,** *79*, 4889-4898.

23) Light, J. C.; Hamilton, I. P.; Lill, J. V., Generalized discrete variable approximation in quantum mechanics. *J. Chem. Phys.* **1985,** *82*, 1400-1409.

24) Echave, J.; Clary, D. C., Potential optimized discrete variable representation. *J. Chem. Phys.* **1992,** *190*, 225-230.

25) Chatterjee, S.; Makri, N., Recovery of purity in dissipative tunneling dynamics. *J. Phys. Chem. Lett.* **2020,** *11*, 8592-8596.

26) Chatterjee, S.; Makri, N., Density matrix and purity evolution in dissipative two-level systems: I. Theory and path integral results for tunneling dynamics. *Phys. Chem. Chem. Phys.* **2021,** *23*, 5113-5124.

27) Bose, A.; Makri, N., Non-equilibrium reactive flux: A unified framework for slow and fast reaction kinetics. *J. Chem. Phys.* **2017,** *147*, 152723.

28) Kundu, S.; Makri, N., Intramolecular Vibrations in Excitation Energy Transfer: Insights from Real-Time Path Integral Calculations. *Ann. Rev. Phys. Chem.* **2022,** *73* (1), 349-375.

29) Caldeira, A. O.; Leggett, A. J., Path integral approach to quantum Brownian motion. *Physica A* **1983,** *121*, 587-616.

30) Frenkel, J., On the transfomation of light into heat in solids. *Phys. Rev.* **1931,** *37*, 17.

31) Makri, N., Small matrix disentanglement of the path integral: overcoming the exponential tensor scaling with memory length. *J. Chem. Phys.* **2020,** *152*, 041104.

32) Makri, N., Small matrix path integral for system-bath dynamics. *J. Chem. Theory Comput.* **2020,** *16*, 4038–4049.

33) Makri, N., Small matrix path integral with extended memory. *J. Chem. Theory Comput.* **2021,** *17*, 1-6.

34) Makri, N., Numerical path integral techniques for long-time quantum dynamics of dissipative systems. *J. Math. Phys.* **1995,** *36*, 2430-2456.

35) Makri, N.; Makarov, D. E., Tensor multiplication for iterative quantum time evolution of reduced density matrices. I. Theory. *J. Chem. Phys.* **1995,** *102*, 4600-4610.

36) Makri, N.; Makarov, D. E., Tensor multiplication for iterative quantum time evolution of reduced density matrices. II. Numerical methodology. *J. Chem. Phys.* **1995,** *102*, 4611-4618.

37) Feynman, R. P., Space-time approach to non-relativistic quantum mechanics. *Rev. Mod. Phys.* **1948,** *20*, 367-387.

38) Feynman, R. P.; Hibbs, A. R., *Quantum Mechanics and Path Integrals*. McGraw-Hill: New York, 1965.

39) Feynman, R. P.; Vernon, F. L., The theory of a general quantum system interacting with a linear dissipative system. *Ann. Phys.* **1963,** *24*, 118-173.

40) Kundu, S.; Dani, R.; Makri, N., B800-to-B850 relaxation of excitation energy in bacterial light harvesting: All-state, all-mode path integral simulations. *J. Chem. Phys.* **2022,** *157*, 115101.

41) Wolfram Research, I. *Mathematica*, Wolfram Research, Inc.: Champaign, Illinois, 2016.

Chapter 6

Conclusion

In this work, we used the path integral based methods developed in the Makri group recently for simulating exact quantum dynamics of spin systems (characterized by Ising interactions) and dendrimers (characterized by Frenkel interactions) where every unit of the system is coupled to a dissipative bath. Path integral methods along with the influence functional treatment of the bath provides for the perfect framework to study these extended systems coupled to a bath fully quantum mechanically. For both kinds of systems, we find interesting features from the real time dynamics of the system.

The two methods used in this thesis are MPI and SMatPI. The computational cost of MPI grows linearly (as opposed to exponentially) with the system size, thus letting us perform numerically exact quantum simulations of extended spin systems. SMatPI is the small matrix decomposition of the previously formulated QuAPI which does away with storage of high dimensionality tensors allowing to extend QuAPI to larger systems.

For Ising spin chains with a transverse field, the dynamics of a given spin in the chain was found to be dependent on the spin-spin coupling strength, spin-bath coupling strength and the location of the tagged spin in the chain. The dynamics transitions from a oscillatory coherent to incoherent monotonic decay (with some parameters displaying an intermittent underdamped oscillatory behavior) with increase in the spin-spin, spin-bath coupling strength and temperature. Considerable edge effects are observed inviting further explorations in this direction.

We also investigated dendrimeric systems with number of generations n=1-4, their ground states and eigenstate structure. Real time dynamics of dendrimers with n = 1-2 are also presented. These exact

numerical results provide valuable insights as to how the magnitude and sign of the intrageneration coupling value affects the ground state and finite temperature population in these dendrimers. We see that even in the absence of an energy bias in between the dendrimer generations, we can get enough accumulation of energy in the dendrimer core. Also, for some parameters we get oscillatory behavior while for some these oscillations are quenched. These very rich behaviors will undoubtedly become even more complex when additional parameters are allowed to vary, inviting additional work on these fascinating systems.

Lastly, we turned our attention to rate theory and showed that for a multistate system connected to a generic environment through terms diagonal in the system basis, the derivative of rates of populations are given directly by the imaginary part of the coherences (the off-diagonal elements of the RDM). For regimes where there is a considerable separation of timescales and the population derivative of the states has a well-defined plateau before settling into a slow decay which characterizes the reactive process, we show that after the "plateau time", rate kinetics are able to produce very accurate results. Thus, for these processes, we need powerful quantum dynamics methods only to simulate the dynamics only up to the short "plateau time" and the remaining long-time population can be calculated integrating the rate equations. In this work we show the regimes where the kinetic equations can correctly reproduce the dynamics after the plateau time and regimes where this breaks down but by simply initializing the differential rate equations with population values at the plateau time gives accurate results.